
Masters Theses

Student Theses and Dissertations

Fall 2011

Heat transfer augmentation in rectangular ducts due to passive flow destabilization

James Jackson Tinsley

Follow this and additional works at: https://scholarsmine.mst.edu/masters_theses



Part of the [Aerospace Engineering Commons](#)

Department:

Recommended Citation

Tinsley, James Jackson, "Heat transfer augmentation in rectangular ducts due to passive flow destabilization" (2011). *Masters Theses*. 5028.

https://scholarsmine.mst.edu/masters_theses/5028

This thesis is brought to you by Scholars' Mine, a service of the Missouri S&T Library and Learning Resources. This work is protected by U. S. Copyright Law. Unauthorized use including reproduction for redistribution requires the permission of the copyright holder. For more information, please contact scholarsmine@mst.edu.

HEAT TRANSFER AUGMENTATION IN RECTANGULAR DUCTS DUE TO
PASSIVE FLOW DESTABILIZATION

by

JAMES JACKSON TINSLEY II

A THESIS

Presented to the Faculty of the Graduate School of the
MISSOURI UNIVERSITY OF SCIENCE AND TECHNOLOGY

In Partial Fulfillment of the Requirements for the Degree
MASTER OF SCIENCE IN AEROSPACE ENGINEERING

2011

Approved by

K. O. Homan, Advisor

A. Banerjee

D. J. Alofs

ABSTRACT

The following thesis documents the comparison of surface enhancements in rectangular ducts for heat transfer enhancement of the air-side of off-road heat exchangers. Two sets of experiments were completed, one utilizing air as the working fluid, and the other utilizing water.

Five air geometries and four water geometries were studied, including those with crosswise bumps, longitudinal vortex generators, and a unique rifling geometry. A smooth test section was also tested in the water experiments to verify the experimental setup. Such verification had been performed previously for the air experiments by Rucker [2007].

The experiment involved an applied constant heat flux to each channel as fluid was circulated through. Heat transfer and friction results were obtained using thermocouple and pressure drop data. The data was then compared and results obtained.

It was found that longitudinal vortex generators give lower heat transfer coefficients than crosswise bumps, but at a substantially lower frictional cost, leading to a higher goodness factor overall. The rifling geometry showed similar heat transfer performance to the crosswise bumps, with substantially lower frictional losses, leading to very good performance overall.

ACKNOWLEDGMENT

This thesis was accomplished with the help of a number of people, whom I'd like to thank. I am thankful to Professor Kelly Homan for facilitating the research, as well as to Adams Thermal Systems for providing the funding and direction. Also my committee members, Professors Arindam Banerjee and Darryl Alofs, for their support and instruction in the discipline of fluid flow. A number of others helped facilitate this research, whom I'd like to thank: Randall Lewis for his time and expertise with the CNC mill, Joe Boze and Bob Hribar in the machine shop, George Green and Ted Davis in the tech shop, Mitch Cottrell for providing much needed technical assistance, as well as Ken Schmid for providing building facilities.

My greatest appreciation goes to my wife Melisia, who has always been supportive and helpful, often willing to do without me when work needed to be done in the lab, and to support me in any way she could. Her contributions to this work have been great, and for that I am forever in her debt.

Finally, I'd like to thank my lab mates Rex Rampton and Andrew Sharp for always being willing to help when one set of hands wasn't enough, and to give advice and encouragement when needed.

TABLE OF CONTENTS

	Page
ABSTRACT	iii
ACKNOWLEDGMENT.....	iv
LIST OF ILLUSTRATIONS	viii
LIST OF TABLES	xii
LIST OF SYMBOLS.....	xiii
 SECTION	
1 INTRODUCTION.....	1
2 LITERATURE REVIEW.....	4
2.1 SURFACE ROUGHNESS	4
2.2 FLOW DESTABILIZATION	5
2.3 REPEATED RIBS	7
2.4 LONGITUDINAL VORTEX GENERATORS (LVGS)	19
3 EXPERIMENTAL APPARATUS	29
3.1 LIQUID LOOP	29
3.1.1 Flow Loop	29
3.1.2 Test Section Design, Fabrication, and Installation	33
3.1.3 Instrumentation	42
3.1.4 Liquid Test Section Surface Geometries	46
3.2 AIR LOOP	49
3.2.1 Flow Loop	49
3.2.2 Test Section Design, Fabrication, and Installation	53
3.2.3 Instrumentation	58

3.2.4	Air Test Section Surface Geometries	61
4	EXPERIMENTAL PROCEDURE	65
4.1	LIQUID LOOP EXPERIMENTS	65
4.1.1	Pressure Drop Measurements	67
4.1.2	Temperature Measurements	67
4.2	EXPERIMENTS INVOLVING AIR	68
5	DATA REDUCTION	70
5.1	DIRECTLY MEASURED QUANTITIES	70
5.1.1	Temperature	70
5.1.2	Mass Flow Rate	71
5.1.3	Differential Pressure	72
5.1.4	Heater Power	73
5.2	CALCULATED QUANTITIES	75
5.2.1	Frictional Losses	75
5.2.2	Heat Transfer	76
5.2.3	Goodness Factor	77
5.3	UNCERTAINTY ESTIMATION	77
5.3.1	Reynolds Number	77
5.3.2	Friction Factor	78
5.3.3	Heat Transfer Results	79
6	RESULTS AND DISCUSSION	80
6.1	LIQUID-LOOP TEST SECTIONS	80
6.1.1	Overall Results	80
6.1.2	Local Observations	83
6.2	AIR LOOP TEST SECTIONS	87
7	CONCLUSIONS AND RECOMMENDATIONS	92

APPENDIX..... 93

REFERENCES..... 114

VITA..... 117

LIST OF ILLUSTRATIONS

Figure	Page
1.1	Example of radiator simulated in present experiments. 2
1.2	Free, forced, and mixed convection regimes for flow in horizontal circular tubes for $10^{-2} < \text{Pr} \frac{D}{L} < 1$ by Metais and Eckert [1964] 2
2.1	Moody Diagram by Moody [1944]. 4
2.2	Periodic eddy-promoter channel geometry. [Karniadakis et al., 1988] 5
2.3	A plot of the unsteady isotherms at one instant in time of the steady-periodic supercritical flow for the base geometry at $\text{Re} = 300$ 6
2.4	Characteristic dimensions of repeated-rib roughness. [Webb et al., 1971] . . 8
2.5	Flow patterns as a function of p/e . [Webb et al., 1971] 9
2.6	Sketch of experimental setup for Webb et al. [1971] 10
2.7	Symmetric vs. staggered ribs. [Han et al., 1978] 11
2.8	Rib cross-sectional shapes. [Han et al., 1978] 11
2.9	Experimental setup used by Han et al. [1978] 12
2.10	Dimensions of duct for Han [1984] 14
2.11	Dimensions of duct for Han [1988] 14
2.12	Schematic of test section used by Greiner et al. [1990] 15
2.13	Streakline flow visualization at $\frac{x}{D_h} = 24.4$: (left) $\text{Re} = 600$, steady flow; (right) $\text{Re} = 700$, traveling wave structure. [Greiner et al., 1990] 16
2.14	Streakline flow visualization showing three-dimensional wave structure at $\frac{x}{D_h} = 24.4$: (left) $\text{Re} = 1000$; (right) $\text{Re} = 2000$ [Greiner et al., 1990] 16
2.15	Partially grooved, rectangular cross-sectional channel used by Greiner et al. [1995]. 17
2.16	Three-dimensional computational domain and spectral element mesh used to investigate a periodically grooved transport passage. [Greiner et al., 1990] 18
2.17	Grooved channel geometry used by Wirtz et al. [1999] 19
2.18	Longitudinal vortices. [Jacobi and Shah, 1995] 20

2.19	Natural and passively generated vortices and vortex generators for heat exchanger applications.	21
2.20	A summary of passive vortex enhancement results by Jacobi and Shah [1995].	22
2.21	Some types of longitudinal vortex generators:	22
2.22	Cross sectional velocity vectors at axial locations $\frac{x}{h} = 1.3, 2.3, 4.3,$ and $9.3,$ showing the formation and development of longitudinal vortices in a channel with a delta winglet pair as shown by Zhu et al. [1993].	23
2.23	Structure of the temperature field in a turbulent channel flow with a delta winglet pair: isotherms for a temperature ratio of $\frac{T_w}{T_0} = 2$ at cross section $\frac{x}{H} = 1.3, 2.3, 4.3,$ and $9.3;$ $Re_H = 50,000,$ $Pr = 0.7$ as shown by Zhu et al. [1993].	24
2.24	Elevation of turbulent kinetic energy in the channel with a built-in delta winglet pair, $Re_H = 50,000,$ as shown by Zhu et al. [1993].	25
2.25	Schematic of the experimental facility of Pauley and Eaton [1988].	25
2.26	Vector plots of secondary flow: $Re_{\frac{H}{2}} = 67,000$ by Dep et al. [1995].	26
2.27	Isolines for turbulent kinetic energy at different cross-sections for $Re_{\frac{H}{2}} = 67,000$ by Dep et al. [1995].	27
2.28	Double vortices with rib at $Re = 1000, 1700.$	28
3.1	Photo of liquid loop test apparatus.	30
3.2	Liquid test section half geometry.	33
3.3	Thermocouple well geometry.	34
3.4	Pressure tap hole geometry.	34
3.5	Pressure tap tubes which were mounted in pressure tap holes.	35
3.6	Flange for mounting test section to test apparatus.	37
3.7	Flange mounted to test section.	37
3.8	End view of liquid test section channel.	38
3.9	Pulling thermocouple wires through slots in heater.	39
3.10	Test section installed in liquid loop.	41
3.11	Mineral wool insulation around liquid test section.	42

3.12	Insulation clamshell installed around liquid test section.	42
3.13	Fully insulated liquid test section.	43
3.14	Pressure measurement setup for liquid loop.	44
3.15	LabView front panel for liquid loop start-up.	46
3.16	WFC010 test section half.	47
3.17	WFC010 bump geometry (dimensions are in inches.)	48
3.18	WFC012 bump geometry (dimensions are in inches.)	48
3.19	WFC103 test section half.	49
3.20	WFC103 half-bump geometry (dimensions are in inches.)	50
3.21	Photo of air loop test apparatus.	51
3.22	Schematic of air loop test apparatus.	52
3.23	Schematic of inlet settling chamber, dimensions in mm [inches].	53
3.24	Test section sides prepared for assembly.	56
3.25	Installing top section onto sides.	56
3.26	Installing bottom section onto sides.	57
3.27	Fasteners used to mount heaters.	58
3.28	Fully insulated air test section.	59
3.29	Schematic of orifice plate installation.	60
3.30	Schematic of pressure measurement system.	60
3.31	Side of SFC010 test section, showing bumps.	62
3.32	SFC010 bump geometry, with dimensions.	62
3.33	SFC020 side geometry, for the inlet portion of the duct.	63
3.34	SFC020 side geometry, for the outlet portion of the duct.	63
3.35	SFC021 side geometry, for the inlet portion of the duct.	64
3.36	SFC021 side geometry, for the outlet portion of the duct.	64
5.1	Friction factor as measured within channel.	73

5.2	Friction factor as measured across settling chambers, no head losses removed.	74
5.3	Friction factor as measured across settling chambers, head losses removed. .	74
5.4	Friction factor error estimation.	79
6.1	Length averaged Nusselt number.	81
6.2	Length averaged Fanning friction factor.	82
6.3	Length averaged Colburn j factor.	84
6.4	Goodness factor comparison.	85
6.5	Wall and bulk fluid variation for WFC000 at $Re = 6493$	86
6.6	Nusselt number variation for WFC000 at $Re = 6493$	87
6.7	Wall temperature variation for WFC012 at $Re=18025$	87
6.8	Wall temperature variation for WFC103 at $Re=1191$	88
6.9	Length averaged Nusselt number.	89
6.10	Length averaged Fanning friction factor.	90
6.11	Length averaged Colburn j factor.	90
6.12	Goodness factor comparison.	91

LIST OF TABLES

Table		Page
6.1	Equivalent pipe sand grain roughness heights, in inches.	83
6.2	Roughness Reynolds number, R_k , values.	83

LIST OF SYMBOLS**Roman**

C_D	discharge coefficient
D	circular duct/pipe diameter
d	orifice flow meter bore diameter
D_h	hydraulic diameter
f	Fanning friction factor
F_{EL}	elevation correction factor
F_{EM}	manometer correction factor
H	channel height
h_w	measured differential pressure across orifice plate
j	Colburn j factor
k	convective heat transfer coefficient
L	linear distance along channel length
\dot{m}	mass flow rate
Nu	Nusselt number
N_{vp}	units conversion factor
\mathcal{P}	pressure

Pr	Prandtl number
P	electrical power (watts)
p	perimeter
Re	Reynolds number
T	temperature
U	mean fluid velocity
\dot{V}	volumetric flow rate
V	voltage, in microvolts
W	channel width
Y_1	gas expansion factor

Greek

η	efficiency
μ	fluid viscosity
ν	fluid kinematic viscosity
ρ	fluid density
ξ	head loss coefficient

Subscripts

b	value refers to the bulk fluid
D_h	value refers to hydraulic diameter

- f1* value refers to orifice plate high pressure tap
- FM* value refers to flow meter
- i* value refers to the inlet settling chamber
- o* value refers to the outlet settling chamber
- T* value refers to a thermocouple
- TH* value refers to thermal properties
- w* value refers to the channel wall
- x* value refers to channel cross section

1. INTRODUCTION

Much study has been done in the area of compact heat exchanger design. Automobile radiators are long-tested, tried-and-true designs that do an efficient job in a small space. Automobiles, however, have certain luxuries that are not afforded to most large machinery and tractors. While automobiles generally move quickly through a relatively clean air stream, machinery and tractors are generally slow-moving and often must ingest air littered with particulates and debris, such as in harvesting grain, bull-dozing, etc.

Because of these differences, machinery radiators must be designed differently than those for automobiles. The louvered fins used in automobiles would clog very quickly in the dirtier environment, and larger fans are needed to move the air in the absence of the fast-moving flow experienced on the open road.

One solution is to make heat exchangers with full-flow passages on the air side through which the air can move largely unrestricted. An example of such a heat exchanger is presented as Figure 1.1. This both helps to keep the heat exchanger from clogging and reduces the pressure drop experienced, allowing for more modest power to move the air through the heat exchanger. The downside to this design, however, is that the heat exchangers must be relatively larger than the louvered-fin design to obtain the same heat duty.

In an effort to reduce the size of such heat exchangers, surface enhancements are placed on the walls of the air-side channels to destabilize the flow and increase heat transfer, while keeping pressure drop to a minimum and at the same time leaving the channels open so debris can pass through and not clog them. Adding to the complexity of the problem is the fact that the Reynolds numbers based on hydraulic diameter experienced in the aforementioned heat exchangers is generally between 600 and 3600 which, for horizontal pipes, is in the transitional regime; though care is taken to ensure that the flow is fully in the forced convection regime (see Figure 1.2.)

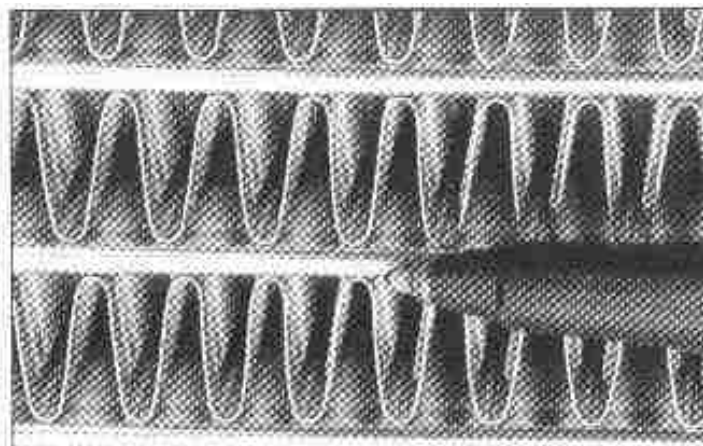


Figure 1.1: Example of radiator simulated in present experiments. Cooling liquid is passed through flat tubes in-between corrugated fins.

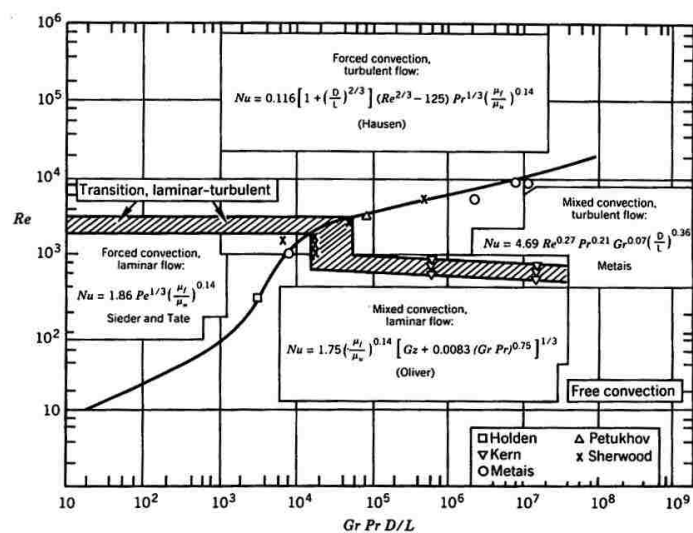


Figure 1.2: Free, forced, and mixed convection regimes for flow in horizontal circular tubes for $10^{-2} < Pr \frac{D}{L} < 1$ by Metais and Eckert [1964]

Two sets of experiments were performed in order to attempt to best represent the flow in the heat exchangers being studied. In both cases, a single channel in the heat exchanger was approximated as a rectangular duct. The channel was manufactured with the desired surface enhancements, and heaters installed. The channel was then well insulated

and fluid passed through the channel and around a closed-loop with heat rejection, allowing for a steady-state to be reached. Fluid temperature measurements were taken at the inlet and outlet of the test section. In addition, temperature measurements were taken at close intervals along the wall of the channel. Finally, differential pressure measurements were taken at points along the channel, as well as across the entire channel in some cases.

In the first set of experiments, air was used as the working fluid, and the channel was scaled to be ten times larger than the heat exchanger dimensions. The Reynolds numbers were kept similar in order to ensure similarity. For a detailed description of the experimental apparatus and procedure, see Sections 3.2 and 4.2.

In the experiments involving air as the working fluid, a significant amount of the heat provided by the heaters was conducted by the wall, making local effects effects impossible to resolve. Therefore, in the second set of experiments, water was used as the working fluid in an attempt to see more one-dimensional flow of heat from the heaters to the fluid. Again, the Reynolds numbers were maintained for similarity. The attempt paid off, and the experiments involving water did in fact produce much better resolution of local effects. For a detailed description of the experimental apparatus and procedure, see Sections 3.1 and 4.1.

In the following sections of the thesis a literature review is performed, the experimental apparatus and procedure are described, an explanation of the data reduction methods used is given, and, finally, results and conclusions are given and recommendations made.

2. LITERATURE REVIEW

2.1. SURFACE ROUGHNESS

In 1933 the German researcher Nikuradse [1950] investigated the affect of surface roughness on the pressure drop through circular pipes. He developed some very useful correlations, and discovered that the pressure drop is proportional to the surface roughness scale divided by the pipe diameter. Later, in 1940, Moody [1944] compiled the most current research of the day, including Nikuradse's, and created the now-famous and much used Moody charts for estimating friction factors and, to some extend, heat transfer coefficients in pipes. An example of the results of his research, called a Moody diagram, is included as Figure 2.1.

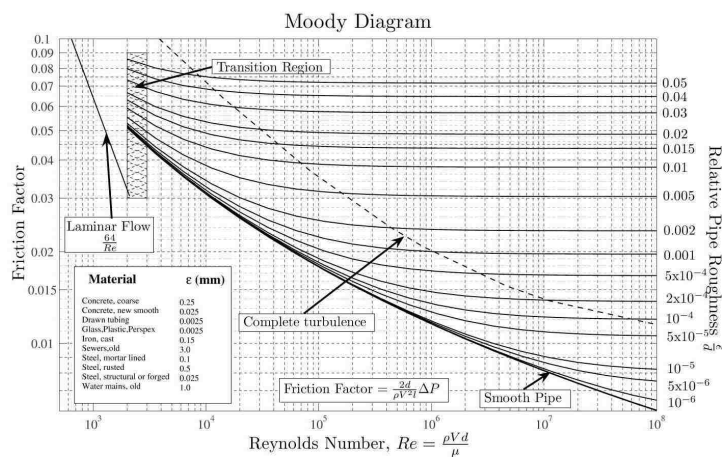


Figure 2.1: Moody Diagram by Moody [1944].

2.2. FLOW DESTABILIZATION

The primary method of augmenting heat transfer is to destabilize the flow, thus promoting mixing and enhancing energy flow from the solid wall to the fluid. There are both active and passive methods for destabilizing the flow. Active methods generally involve fluctuation of the flow rate in some way. Passive methods involve using flow geometries to generate the flow destabilization. For our purposes, we will only consider passive methods of destabilization. Karniadakis et al. [1988] studied flow destabilization using direct numerical simulation by placing flow-disrupting cylinders in a periodic array within a plane channel, a diagram of which can be seen in Figure 2.2. Simulations of the channel were run with and without the cylinders present, and results compared.

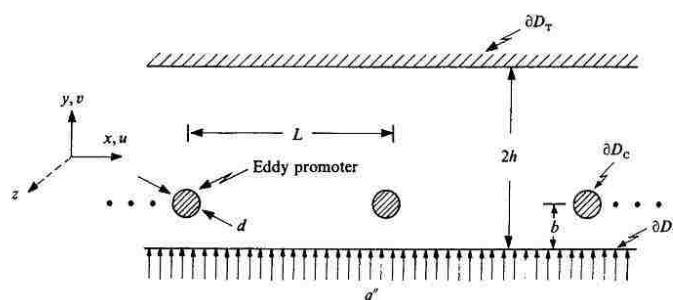


Figure 2.2: Periodic eddy-promoter channel geometry. [Karniadakis et al., 1988]

They reference Isaacson and Sonin [1976], the results of which implicate low-Reynolds-number configurations as producing minimum dissipation for a given mass transfer rate. The aim of their analysis was to determine if simple hydrodynamic arguments can be put forth that isolate the critical phenomena or parameters that determine the relationship between ‘desirable’ heat or mass transfer and ‘unwanted’ viscous dissipation.

They take the Reynolds’ analogy as the focus of their study and they note that, while the Reynolds analogy is only truly rigorous for the case of the laminar flat-plate boundary

layer with unity Prandtl number, it appears to be valid in flows in which direct pressure effects are small, in which a strong convective-diffuse balance prevails, and in which the gradients in velocity and temperature appear in similar ways in their respective equations. Then, taking the Reynolds analogy as given, they state that it then follows from simple momentum and energy integrals that shear stress, pressure drop, and viscous dissipation are all reduced if a lower-Reynolds-number flow can be found that achieves the same heat transfer rate as a higher-Reynolds-number flow. Thus, transport enhancement can best be described as a hydrodynamic stability problem. A more unstable flow (that is, a flow with a lower critical Reynolds number) will generate larger Reynolds fluxes at lower Reynolds numbers, and thus achieve the same Nusselt number at a lower Reynolds number, and therefore a lower dissipative cost, than a more stable flow.

They demonstrate that the most significant increase in space-average Nusselt number is due to the spatially homogeneous Tollmien-Schlichting wave, not due to local flow phenomena induced by the cylinder (see Figure 2.3.) They conclude that eddy-promoter flows achieve significant heat transfer at low Reynolds numbers, and do so while roughly preserving the Reynolds analogy, and that eddy promoter flows can save up to 500% in dissipation in the Nusselt-number (Nu) range of approximately $1 < Nu < 5$.

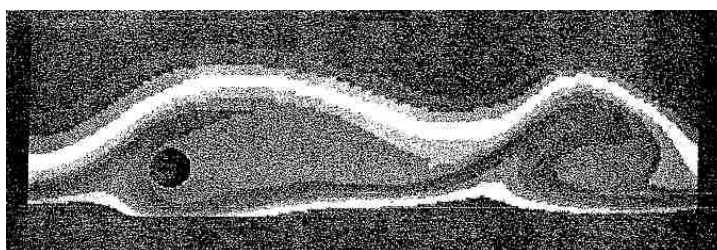


Figure 2.3: A plot of the unsteady isotherms at one instant in time of the steady-periodic supercritical flow for the base geometry at $Re = 300$. Transport enhancement is effected by Tollmien-Schlichting-induced convective mixing. [Karniadakis et al., 1988]

They further conclude that at larger Reynolds numbers the dissipation reduction in eddy-promoter flows decreases into the turbulent regime, though there is an exception at transition. The reason for this decrease in dissipation reduction is the fact that as Reynolds number increases the scales of motion destabilized by the eddy promoters are increasingly naturally unstable, so the eddy promoters make relatively less difference in flow mixing, while continuing to contribute to dissipation through cylinder drag. Therefore, if significant reduction in dissipation is to be realized as Reynolds number and Nusselt number increase, then destabilization should be applied at the naturally stable scales of motion (such as the viscous sublayer in turbulent flow.)

Kozlu et al. [1988] demonstrates an experimental method for optimizing the scale and type of flow destabilization. They considered the cylindrical eddy promoters as well as microgrooves along the wall. They found that for very low thermal load, laminar smooth wall flow performs best due to enhancements having little effect because of the strong stability of the low Reynolds number flow (a method for choosing optimal Reynolds number based on thermal load is presented in the article.) As thermal load increases the macro scale eddy promoters become relatively more efficient than the flat channel. Finally, as thermal load, and therefore Reynolds number, increases further, eddy promoters lose their effect due to the scales at which the eddy promoters have affect becoming naturally unstable. At this point microgrooves, which match the 'stable' part of the flow, namely the viscous sublayer, become most beneficial.

2.3. REPEATED RIBS

Perhaps the most studied method for flow destabilization and thus augmentation of heat transfer in ducts is by placing repeated ribs on the walls of the channel normal to the flow direction.

Webb et al. [1971] developed useful correlations for heat transfer for turbulent flow in tubes having repeated-rib roughness. They used the law of the wall similarity correlations developed by Nikuradse for friction; and for heat transfer they used a correlation based on application of a heat-momentum transfer analogy to flow over a rough surface, which was first used by Dipprey and Sabersky for sand-grain roughness. In their work, they used two non-dimensional parameters: rib height, e , divided by diameter, D , and rib spacing, p , divided by diameter, D (see Figure 2.4.)

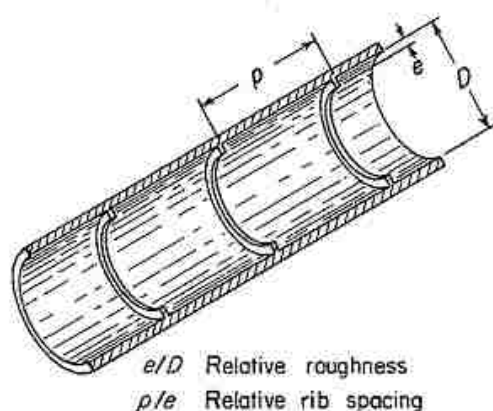


Figure 2.4: Characteristic dimensions of repeated-rib roughness. [Webb et al., 1971]

It was mentioned in the article that, while the repeated-rib surface can be classified as a “roughness” geometry, it may also be viewed as a problem in boundary layer separation and re-attachment. Note in Figure 2.5 that when the rib spacing is large, the flow detaches and a recirculation zone develops downstream of the rib, and flow reattaches 6-8 rib heights downstream from the separation point. It is at this reattachment point that experimental measurements [Edwards and Sheriff, 1961], [Emmerson, 1966] show the maximum heat transfer occurs.







Ref	p/e	Flow pattern
[15]	$\rightarrow \infty$	
[16]	10	
[16]	8	
[16] [17]	5	
[16] [17]	2	
[16] [18]	0.75- 1.25	

Figure 2.5: Flow patterns as a function of p/e . [Webb et al., 1971]

An experimental setup was used by Webb in which air was forced through a roughened tube with heaters attached to the tube and heat transfer and pressure drop measured. See Figure 2.6 for a schematic of the experimental setup. Four different roughness geometries were studied. The data were then plotted and correlations established. The friction data showed that $u_e^+ = 0.95(p/e)^{0.53}$ for $e^+ > 35$. Adding in the heat transfer data, a relation for Stanton number was determined, shown in Equations 2.1 and 2.2.

$$St = \frac{f/2}{1 + \sqrt{f/2}[4.3(e^{0.28}Pr^{0.57} - 0.95(p/e)^{0.53})]} \quad (2.1)$$

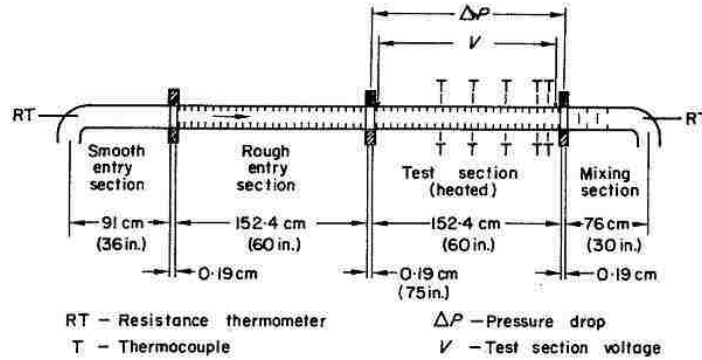


Figure 2.6: Sketch of experimental setup for Webb et al. [1971]

$$\sqrt{2/f} = 2.5 \ln(D/2e) - 3.75 + 0.95(p/e)^{0.53} \quad (2.2)$$

They concluded that law of the wall similarity with a logarithmic velocity distribution gives good correlations for repeated-rib friction data. It was also concluded that the heat-momentum transfer analogy based on the law of the wall similarity adequately correlates the heat transfer data over a wide range of e/D , p/e , and Pr . It is also postulated that law of the wall similarity and heat-momentum analogy may be applied to correlations for geometrically similar forms of arbitrary roughness.

Han et al. [1978] revisited the repeated rib geometry in an effort to study lower Reynolds number flow as well as the effects of rib symmetry (see Figure 2.7), rib angle of attack, and rib cross sectional shape (see Figure 2.8) on both friction and heat transfer. A similar experimental setup to Webb et al. [1971] was used (see Figure 2.9) and air was again the working fluid.

It is noted that for turbulent flows at lower Reynolds numbers a larger rib height to hydraulic diameter ratio is needed to achieve fully rough flow conditions. It is also noted that ribs perpendicular to the flow induce the largest form drag, and that reducing the angle of attack from 90 degrees can give a better thermal to hydraulic performance.

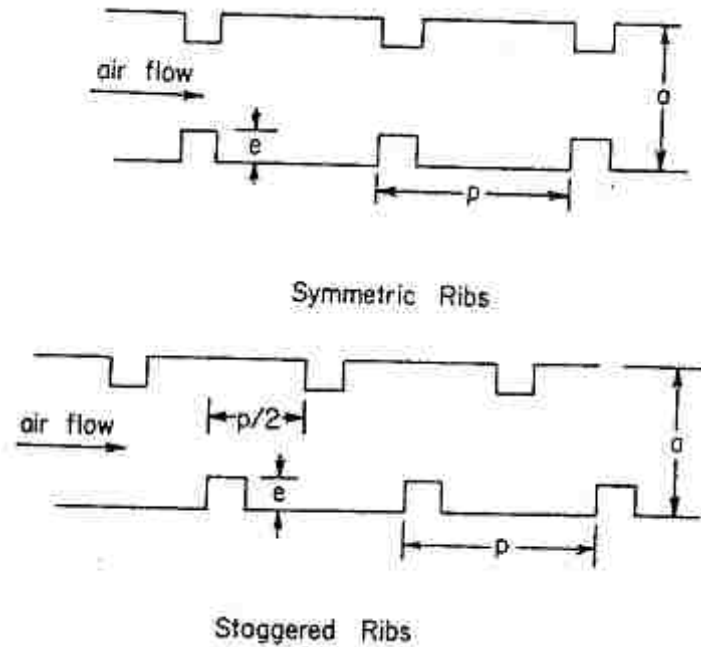


Figure 2.7: Symmetric vs. staggered ribs. [Han et al., 1978]

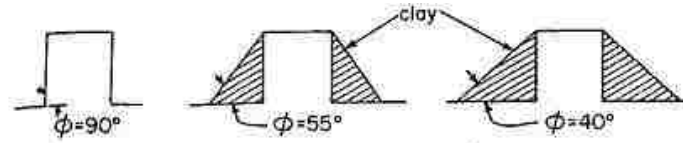


Figure 2.8: Rib cross-sectional shapes. [Han et al., 1978]

They, therefore, determine to find an optimal height to hydraulic diameter ratio as well as an optimal rib angle of attack.

A number of different rib shapes, heights, and angles of attack were investigated and it was concluded that symmetry is of little importance, and that rib cross-sectional shape has a marked effect on friction factor, but only a modest effect on heat transfer. It was determined that a rib angle of attack of 45 degrees gives higher heat transfer for the same friction power than that of 90 degrees. It was also found that both the Stanton

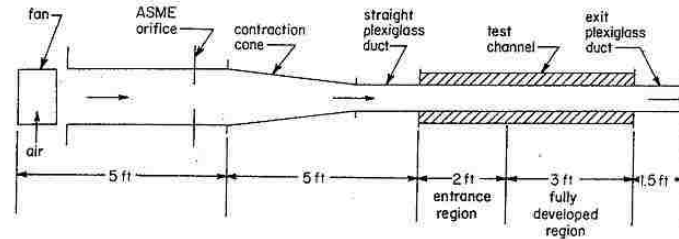


Figure 2.9: Experimental setup used by Han et al. [1978]

number and friction factor have a maximum value when the pitch-to-height ratio of the ribs is approximately ten.

Han [1984] once again investigated ribbed roughness in channels, but this time his aim was to discover the effect of having two opposite walls roughened, while having the other two smooth. This case is of particular interest for the present application since the geometry will be similar. When creating a heat exchanger such as the one shown in Figure 1.1 it is not feasible to roughen all four sides of the approximately rectangular channel. The convention, therefore, is to roughen the two vertical sides and leave the horizontal sides smooth.

The experimental apparatus was very similar to that used previously by Han et al. [1978], and consists of a blower forcing room air through the roughened section, with pressure and temperature measurements taken at various locations to determine overall heat transfer and pressure drop across the channel.

It was concluded that the Stanton number of the ribbed walls was increased by about 1.5 to 2.2 times compared to a smooth duct, but were about 10 percent lower than that for a four-sided ribbed duct. On the smooth walls the Stanton number was increased about 25 percent as compared to the four-sided smooth duct.

The average friction factor was about 2 to 6 times that of the four-sided smooth duct for the range of data tested, but about 30-45 percent lower than that of the four-sided ribbed duct.

Finally, it was concluded that the average friction factor can be determined by a weighted average of the four-sided smooth duct friction factor and the four-sided ribbed duct friction factor by the relation in Equation 2.3.

$$\bar{f} = \frac{Af_s + Bf_r}{A + B} \quad (2.3)$$

Where A is the duct width along the smooth walls, B is the duct width along the rough sides (see Figure 2.10,) f_s is the friction factor for the four-sided smooth duct, and f_r is the friction factor for the four-sided rough duct.

Similarly, the average Stanton number can be predicted by a weighted average of the four-sided smooth duct and the four-sided ribbed duct Stanton numbers, as in Equation 2.4.

$$\bar{St} = \frac{ASt_s + BSt_r}{A + B} \quad (2.4)$$

Where A and B are defined as above, St_s is the Stanton number of the four-sided smooth channel, and St_r is the Stanton number of the four-sided rough channel.

Han [1988] once again looked into the rectangular channel with two facing ribbed walls and two smooth walls. Much of the data presented and conclusions reached are similar to those already mentioned. One point of note, however, is that the heat transfer and friction characteristics are affected by aspect ratio and, particularly, whether the ribs are placed on the long or short walls of the channel. Han reports that when the channel aspect ratio, W/H , with ribs on side W as shown in Figure 2.11, is changed from $\frac{1}{4}$ to 4 with pumping power kept constant, that the ribbed side wall heat transfer is decreased, but

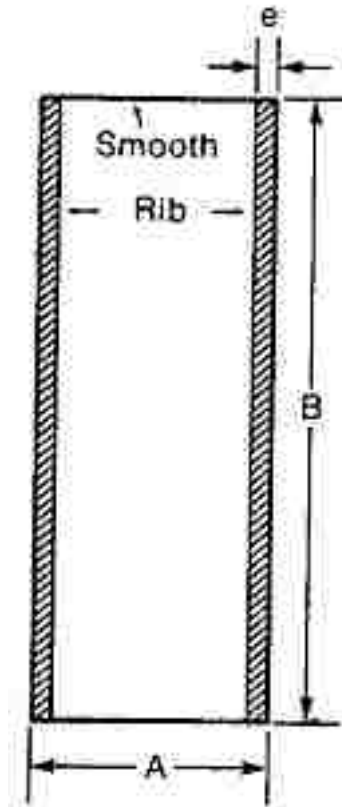


Figure 2.10: Dimensions of duct for Han [1984]

that the average heat transfer is increased, giving a more even distribution of heat removal and a more efficient system overall.

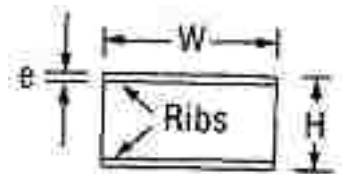


Figure 2.11: Dimensions of duct for Han [1988]

Up to this point, all of the flows looked at in this section have been in the fully turbulent regime. Greiner et al. [1990] performed a similar experimental procedure to those above, but for flows in the Reynolds number range of $300 < Re < 15,000$. A schematic of the test section which was used can be seen in Figure 2.12. In addition to heat transfer measurements, flow visualization was also used. For the case of flow visualization, the heater on top of the section was replaced with a Plexiglas cover and a tracer dye was injected, and the flow videotaped.

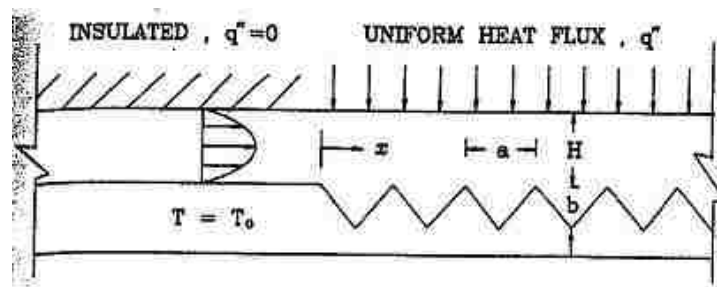


Figure 2.12: Schematic of test section used by Greiner et al. [1990]

Figures 2.13 and 2.14 show a representation of the streaklines observed. A progression can be seen with increasing Reynolds number. In Figure 2.13 at $Re = 600$ the flow is subcritical, and individual recirculation zones can be seen within each groove, while the outer flow is straight and parallel to the upper wall, as if there were no grooves at all, emphasizing what was said before that flow destabilizations are not beneficial for very low Reynolds number flows. At $Re = 700$ a traveling wave structure develops, and the outer flow is beginning to be disturbed. These streaklines are described as “smooth”, and mostly two-dimensional. In Figure 2.14 it can be seen that small-scale structures begin to be superimposed on top of the waves. As the Reynolds number increases, the length scales of the smaller structures decrease and the three-dimensionality of the flow increases. It is

noted that the Reynolds number above which flow is oscillatory 50 percent of the time is approximately 630.

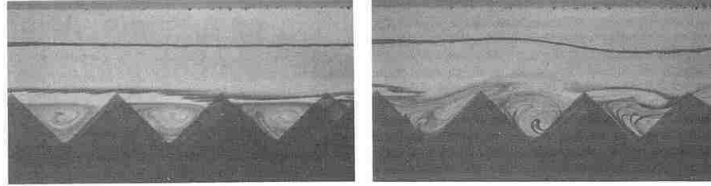


Figure 2.13: Streakline flow visualization at $\frac{x}{D_h} = 24.4$: (left) $Re = 600$, steady flow; (right) $Re = 700$, traveling wave structure. [Greiner et al., 1990]

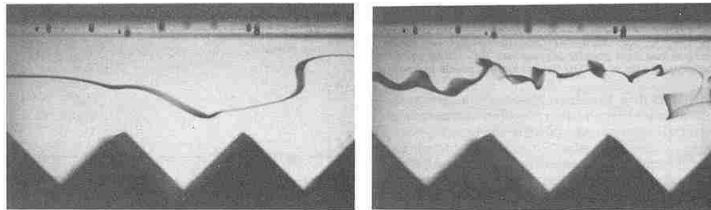


Figure 2.14: Streakline flow visualization showing three-dimensional wave structure at $\frac{x}{D_h} = 24.4$: (left) $Re = 1000$; (right) $Re = 2000$ [Greiner et al., 1990]

Heat transfer measurements showed that for this channel configuration, an enhancement in heat transfer in excess of 10 percent extends over the range $1200 < Re < 4800$, and $\frac{x}{D_h} > 16$, with the maximum enhancement of 65 percent occurring at $Re = 3000 \pm 1000$.

Greiner et al. [1995] further studied the behavior of the flow downstream of a grooved section similar to that described above, a schematic of which can be seen in Figure 2.15. The regime studied was $1000 < Re < 5000$. It was concluded that the unsteadiness produced by the grooves persists for up to 20 hydraulic diameters past the end of the grooved section. The recovery lengths for shear stress and pressure gradient drop

off rapidly as Reynolds number increases beyond $Re = 3000$, while the decrease in heat transfer augmentation is much less rapid, leading to an increase in heat transfer to pumping power ratio. The article states that the difference between the recovery lengths for shear stress and heat transfer indicate that heat/momentum transport mechanics in this region are uncoupled. It may, therefore, be most beneficial to have intermittently grooved channels to maximize heat transfer while minimizing required pumping power.

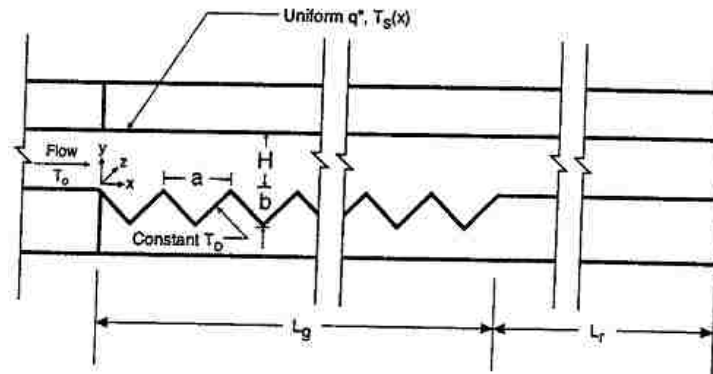


Figure 2.15: Partially grooved, rectangular cross-sectional channel used by Greiner et al. [1995]. The channel has width W normal to the page. The z -coordinate origin ($z = 0$) is at the center span.

Greiner et al. [1998] further performed a three-dimensional direct numerical simulation of a grooved channel. A single groove was modeled, with periodic boundary conditions along the length and width of the channel (x and z directions), with solid wall boundary conditions at the top of the channel and the bottom of the groove. The computational domain used, with axes labeled, is shown in Figure 2.16.

It was concluded that at $Re = 325$ the flow was steady and two-dimensional, but it exhibits a series of transitions with increasing Reynolds number. At $Re = 350$, two dimensional traveling waves are exhibited. For $Re = 482$, the flow becomes time-periodic and regular variations in cross-stream flow are observed. For $Re = 748$, the flow exhibits

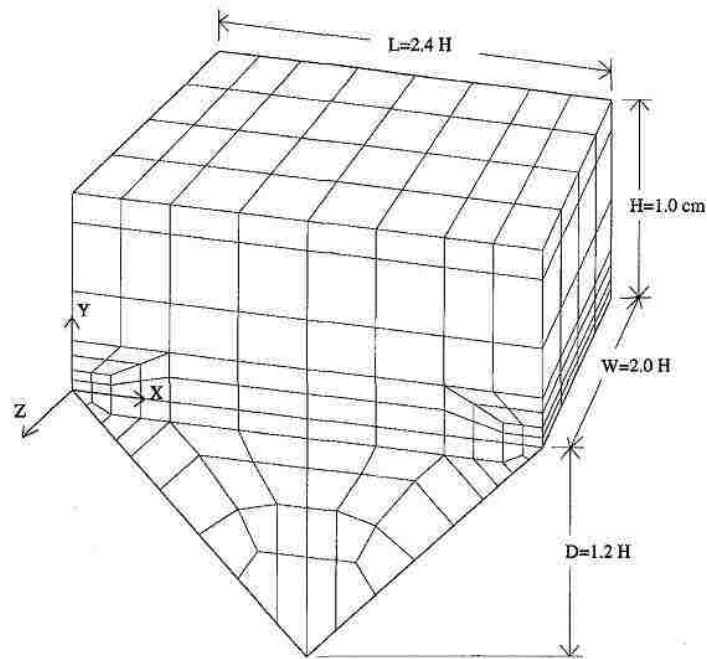


Figure 2.16: Three-dimensional computational domain and spectral element mesh used to investigate a periodically grooved transport passage. [Greiner et al., 1990]

irregularities in the z -direction, and more than one dominant frequency is observed. Finally, for $Re = 1530$, the flow becomes very irregular and a wide band of flow frequencies is observed.

It was also noted that two dimensional simulations of the grooved channel flow predict laminar-like (unmixed) friction factor and Nusselt number verses Reynolds number behaviors. The author recommends that three-dimensional computations are required to accurately quantify the heat and momentum transport behavior for $Re > 500$.

Wirtz et al. [1999] once again studied forced convection in a grooved channel experimentally. For this analysis the channel was grooved on both top and bottom, as shown in Figure 2.17. Interesting conclusions from this analysis include the finding that the heat flux is not uniform across the grooves, but that it has a minimum at the vertex of each groove. Also, the Nusselt number of the windward face of each groove is approximately

twice that of the leeward face. Finally, the fully developed j-factor becomes greater than equivalent flat channel values when $Re > 450$.

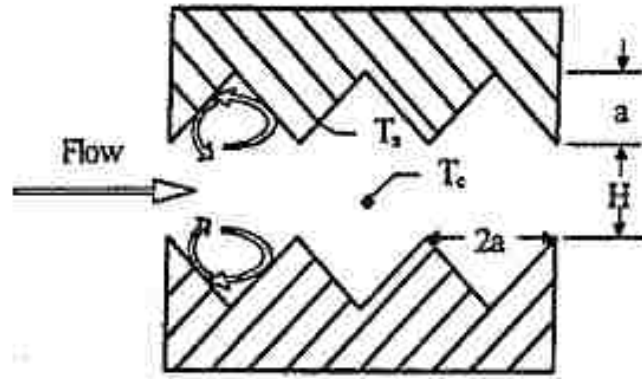


Figure 2.17: Grooved channel geometry used by Wirtz et al. [1999]

2.4. LONGITUDINAL VORTEX GENERATORS (LVGS)

Another common method for enhancing heat transfer on a surface is by the generation of longitudinal vortices. Longitudinal vortices are vortices which have their axis of rotation in the direction of the mean flow path as shown in Figure 2.18. These vortices tend to persist in the flow longer than transverse vortices. We will commence a review of some studies involving methods for generation of longitudinal vortices.

Jacobi and Shah [1995] reviewed the current literature of the day pertaining to longitudinal vortex generators. They mention several different methods for generating longitudinal vortices, shown in Figure 2.19, and compare the different methods for overall heat transfer enhancement as well as pressure drop penalty, where available. A table summarizing what was found is presented as Figure 2.20. It appears from the table that, for

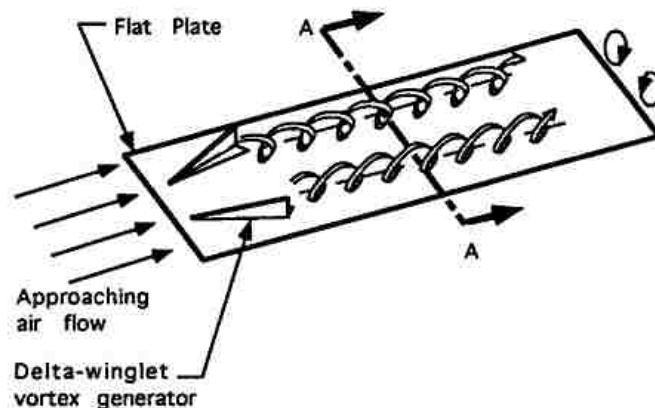


Figure 2.18: Longitudinal vortices. [Jacobi and Shah, 1995]

rectangular channels, heat transfer enhancement is on the order of 20-77%, with pressure drop penalty ranging from 45-145%.

Jacobi and Shah [1995] concluded that, while some data existed, much more research needed to be done before a real understanding of LVG geometry could be had. They made particular mention of more LVG testing needing to be done in channels and pipes since most compact heat exchangers utilize flow through channels, not flow over flat plates. They also surmise that laminar flow with passively induced longitudinal vortices could prove to be more efficient than turbulent flow in compact heat exchangers due to the decreased entropy generation of the less chaotic flow.

Zhu et al. [1993], with the help of numerical techniques, studied heat transfer augmentation due to LVGs in a rectangular channel. Figure 2.21 shows the different LVG geometries studied. To illustrate what is happening when the flow passes over a LVG Figure 2.22 shows some cross sectional velocity vectors at various x locations within and downstream of a channel with a delta winglet pair showing the formation and development of longitudinal vortices. Similarly, Figure 2.23 shows the structure of the temperature field. Note how the vortices mix the flow and bring the higher temperatures from the walls into

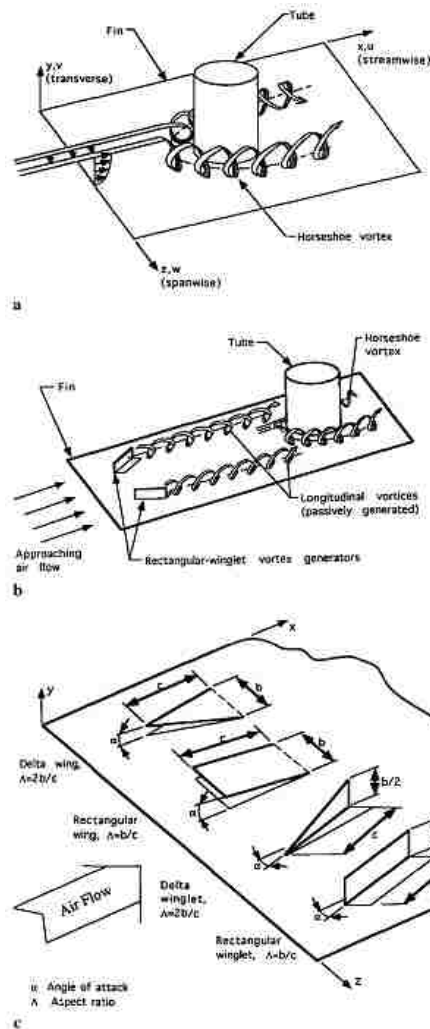


Figure 2.19: Natural and passively generated vortices and vortex generators for heat exchanger applications. (a) The natural formation of a laminar horseshoe vortex at a fin-tube junction; (b) typical passively generated longitudinal vortices; (c) common vortex generators and the associated geometrical definitions. [Jacobi and Shah, 1995]

the inner flow. Finally, Figure 2.24 shows an increase in turbulent kinetic energy due to the longitudinal vortices. They concluded that this increase in turbulent kinetic energy, along with the exchange of the fluid between the near wall and core region of the channel, were the mechanisms which augmented the heat transfer from the wall to the fluid. For the geometry studied, they reported an increase in mean heat transfer of 16-19%, with a

Ref.	Geometry	$Re/(10^3)$	Overall Heat Transfer ^a Enhancement	Pressure Drop Penalty	Method of the Study
21	Cubic protuberances and delta winglets	61	76% cube 42% counter 15% corot (local)	Unknown	Luminescent phosphor
22	Plate-fin heat exchanger (full scale)	0.3–2.2	50%	20–30%	LCT ^b
23	Flat plate/rectangular winglets	30–300	100%	Unknown	Conventional thermocouples
24	Rectangular channel with a delta wing, delta winglets, and rectangular winglets	1.36–2.27	20–60% (delta wing)	Unknown	LCT
25, 42	Rect. channel with delta wing (no hole) Rect. channel with delta wing (hole)	0.50	34% 10%	79% 48%	Computational
26, 27	Parallel plates with a delta winglet pair	1.0–4.0	84%	Unknown	Computational
28, 29	Turbulent boundary layer/channel wall	50	16–19%	300–400%	Computational
30–32	Rectangular channel delta wings winglet pair multiple pairs, inline multiple pairs, staggered	1.0–2.0 5.6 4.6 4.6	50% 77% 60% 52%	45% Unknown 145% 129%	LCT and drag measurements
33–36	Rectangular channel with one tube, winglet pair downstream of tube	5.0	20%	–10% (lower ΔP)	LCT/drag [33, 34]; computational [35, 36]
38, 39	Three tube rows inline round staggered round flat tubes	0.6–3.0	55–65% 9% 100%	20–44% 3% 100%	LCT and drag

^a Typical or maximum overall heat transfer enhancement unless otherwise noted.

^b Transient liquid crystal thermography.

Figure 2.20: A summary of passive vortex enhancement results by Jacobi and Shah [1995].

corresponding increase in flow losses of 400-500% over that of turbulent flow in a channel with no vortex generator. They also presented ratios of Nusselt number with and without LVGs on each wall for the different LVG types and made recommendations for choosing the best type of LVG for a given flow based on their findings.

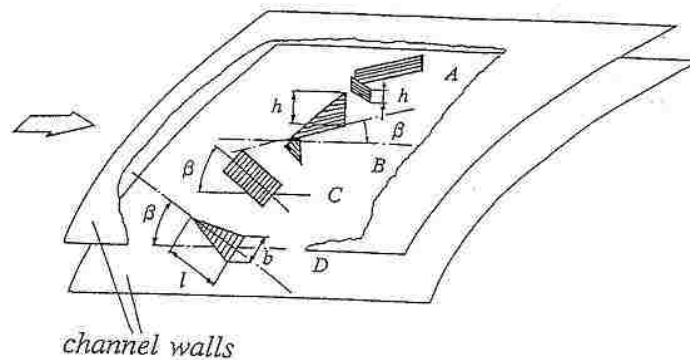


Figure 2.21: Some types of longitudinal vortex generators: A) Rectangular Winglet Pair (RWP); B) Delta Winglet Pair (DWP); C) Rectangular Wing (RW); D) Delta Wing (DW). [Zhu et al., 1993]

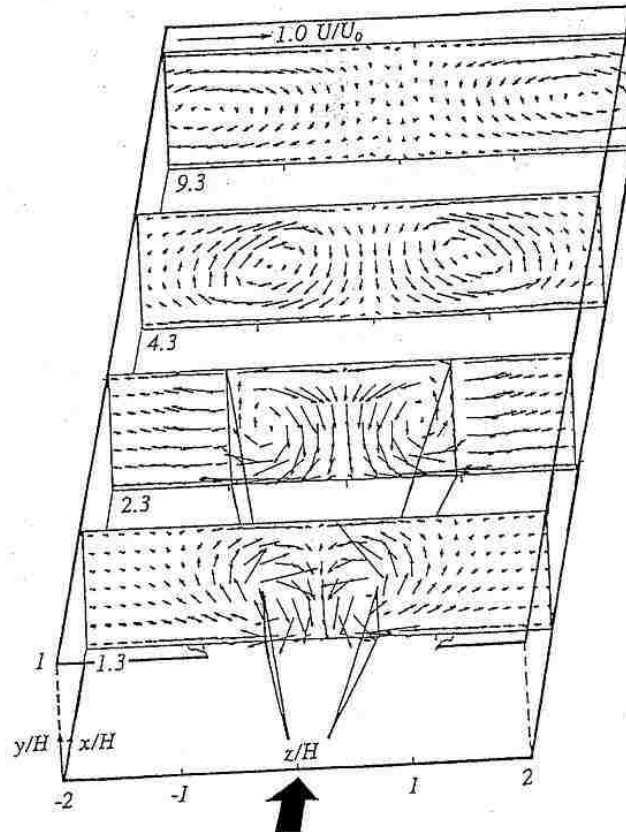


Figure 2.22: Cross sectional velocity vectors at axial locations $\frac{x}{h} = 1.3, 2.3, 4.3,$ and $9.3,$ showing the formation and development of longitudinal vortices in a channel with a delta winglet pair as shown by Zhu et al. [1993].

Dep et al. [1995] did very similar work to Zhu et al. [1993] and compared their results to previous experimental work. They used a RANS $k - \epsilon$ model, the details of which I will leave to the reader to reference the paper. They found that the numerical model gave good results compared to the experiments done by Pauley and Eaton [1988]. Figure 2.25 shows the schematic of the experimental facility used by Pauley and Eaton [1988]. The numerical domain chosen by Dep et al. [1995] was configured to mimic this geometry. Figure 2.26 shows vector plots of the secondary flow for both the numerical and experimental case at three x locations after the LVG. Although the results seem to correspond quite well at $x = 97\text{cm}$ and $x = 188\text{cm}$, at $x = 142\text{cm}$ the experiments show larger secondary ve-

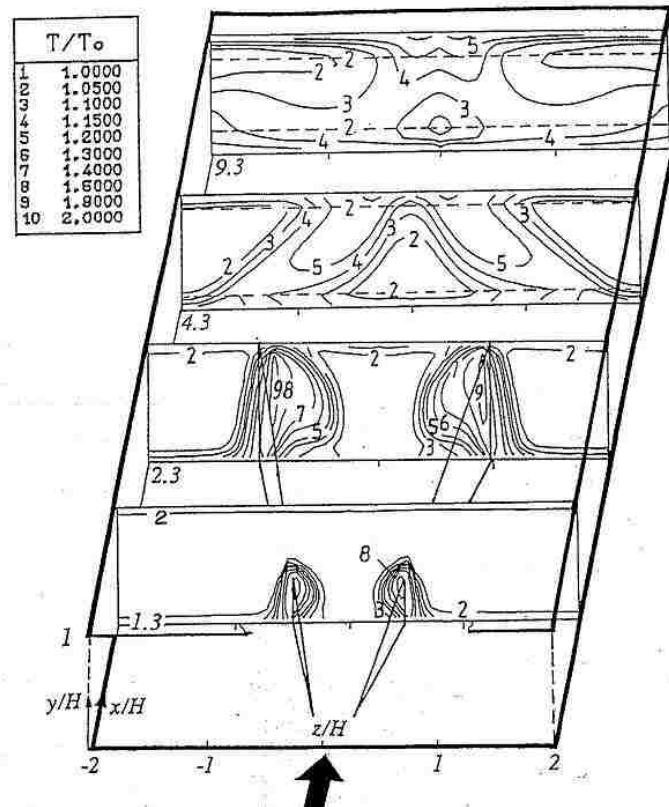


Figure 2.23: Structure of the temperature field in a turbulent channel flow with a delta winglet pair: isotherms for a temperature ratio of $\frac{T_w}{T_0} = 2$ at cross section $\frac{x}{H} = 1.3, 2.3, 4.3,$ and 9.3 ; $Re_H = 50,000$, $Pr = 0.7$ as shown by Zhu et al. [1993].

locities than those computed numerically, though the dissipative trends are shown in both. Finally, Figure 2.27 shows isolines of turbulent kinetic energy at different x locations for both the numerical and experimental setups. Again, the results look to be in good harmony at $x = 97cm$ and $x = 188cm$, but unfortunately the $x = 142cm$ location is not presented. No quantitative measurement of error between the numerical and experimental results are given.

Biswas et al. [1996] did similar numerical work with a single LVG winglet as well as a winglet pair. They studied the effect of different winglet angles of attack on Nusselt number as well as on the quality factor (j/f). Increased angle of attack uniformly increased

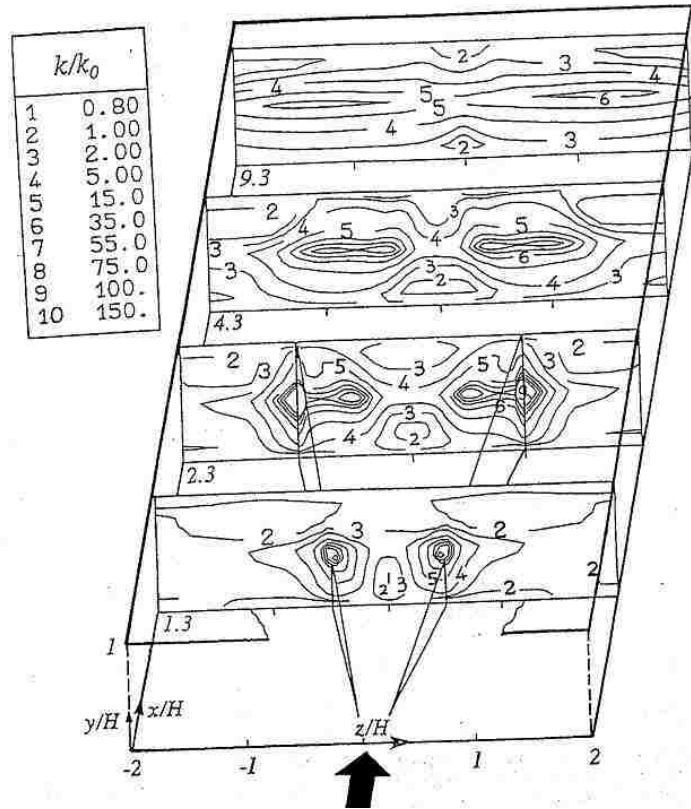


Figure 2.24: Elevation of turbulent kinetic energy in the channel with a built-in delta winglet pair, $Re_H = 50,000$, as shown by Zhu et al. [1993].

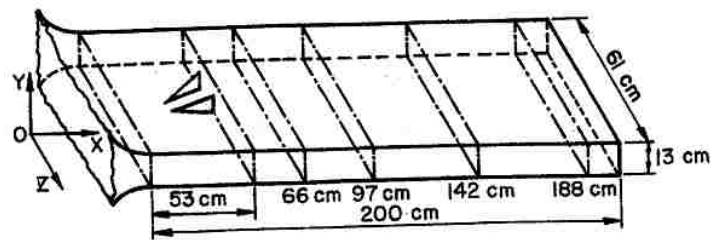
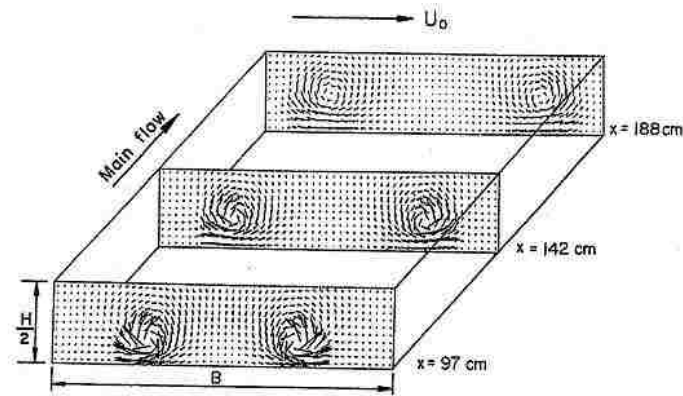
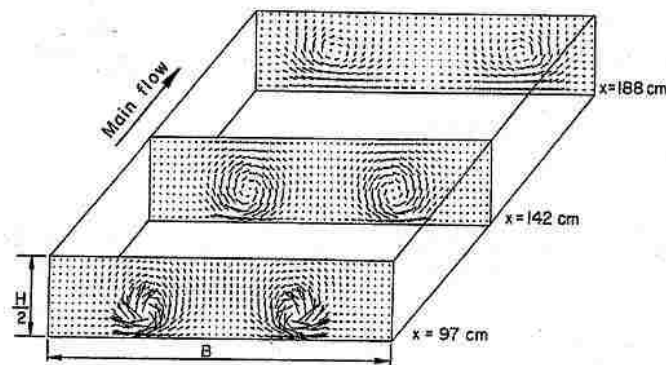


Figure 2.25: Schematic of the experimental facility of Pauley and Eaton [1988].

Nusselt number, while decreasing the quality factor (j/f) for the regime studied ($Re = 1580$, $\alpha = 3$, $Pr = 0.7$.)



(a) Experiment due to Pauley and Eaton (1988 a, b)



(b) Present computation

Figure 2.26: Vector plots of secondary flow: $Re_{\frac{H}{2}} = 67,000$ by Dep et al. [1995].

In their conclusion, they give an explanation of the method by which a winglet induces a longitudinal vortex. They state that the main vortex is formed by the flow separation at the leading edge of the winglet, while the corner of the winglet induces a horseshoe-like vortex. These vortices induce a vortex opposite in rotation to both of themselves. The combined effect of these vortices distorts the temperature field and serves ultimately to bring about enhancement of heat transfer between the fluid and neighboring surfaces.

Xiao-wei et al. [2007] published some nice visualizations of LVG induced flow, a representation of which is shown in Figure 2.28. They concluded that vortex intensity

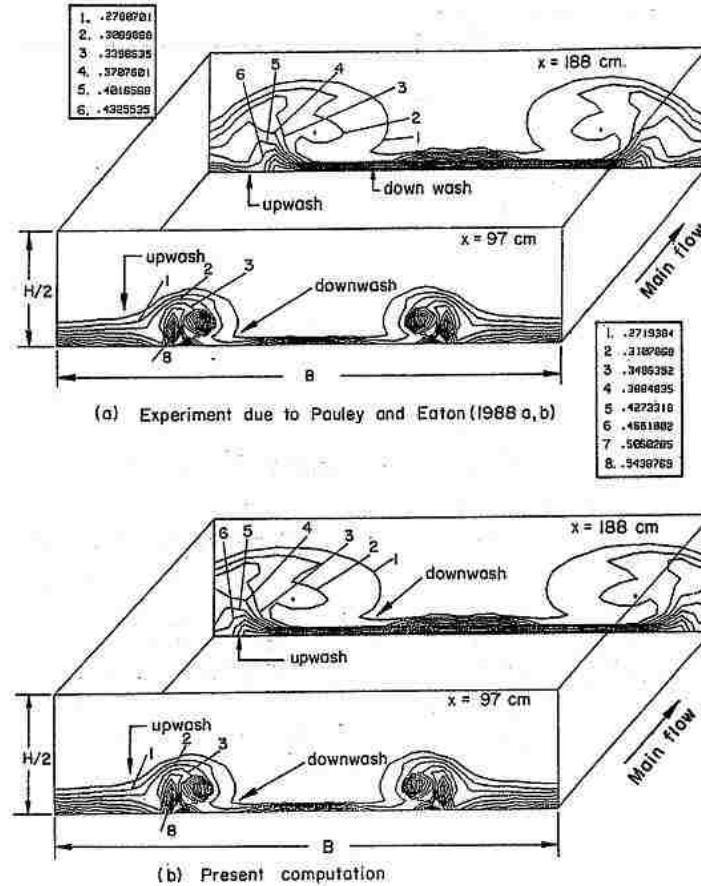


Figure 2.27: Isolines for turbulent kinetic energy at different cross-sections for $Re_{\frac{H}{2}} = 67,000$ by Dep et al. [1995].

increased with increased Reynolds number and that the distance over which the vortices flowed downstream decreased with increasing Reynolds number.

Wu and Tao [2008] performed a numerical simulation of a delta winglet LVG and verified that increasing angle of attack uniformly increases pressure drop. They also found that punching the LVG out and leaving a hole in the fin increased heat transfer near the location of the LVG, but has little effect on the overall heat transfer. Finally, they found that an angle of 45 degrees gives the highest Nusselt number compared to the other angles studied (15, 30, 60, and 90 degrees.)

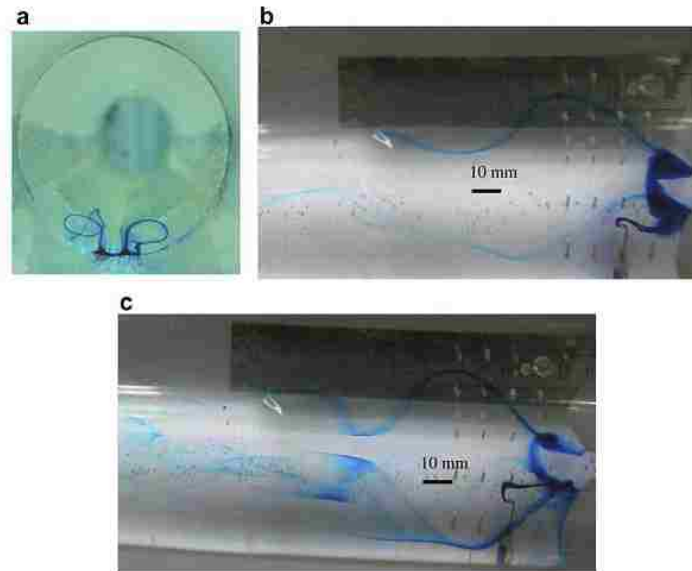


Figure 2.28: Double vortices with rib at $Re = 1000, 1700$. (a) $Re = 1000$, (b) $Re = 1000$, (c) $Re = 1700$, by Xiao-wei et al. [2007].

3. EXPERIMENTAL APPARATUS

This section describes in detail the experimental apparatus used to conduct the experiments for both the liquid and air experiments. Though the premise was the same in both cases, there is enough of a difference in the two apparatus that they are treated separately here. Section 3.1 describes the experiments involving water, and Section 3.2 describes the experiments involving air.

3.1. LIQUID LOOP

The experimental apparatus consisted primarily of a closed loop through which water was circulated. Installed in the loop was an aluminum channel with surface enhancements machined in the channel walls, referred to hereafter as the test section. Heaters were installed on the test section, and a heat exchanger was installed in another part of the loop for heat rejection. The loop, along with supporting instruments, was mounted to a 10 foot long pallet rack for convenience. The apparatus was constructed and first used by Bridges [2007], though modifications were made to accommodate the current research. A photo of the entire apparatus is presented as Figure 3.1. Each portion of the apparatus is described in more detail in the following sections.

3.1.1. Flow Loop. The majority of the flow loop was constructed using 5/8 in. nominal diameter type L nitrogenized ACR/MED rigid copper tubing and brass Swagelok-style 3/4 in. O.D. tube fittings. The subsections below describe each portion of the loop in the order of fluid flow, starting with the pump.

3.1.1.1. Pump. The pump used was a Dayton 6PA10 stainless steel rotary gear pump, with optional thickened gasket. The pump material allowed for high temperature operation, as well as good corrosion resistance. The pump was driven by a Dayton 6XH74

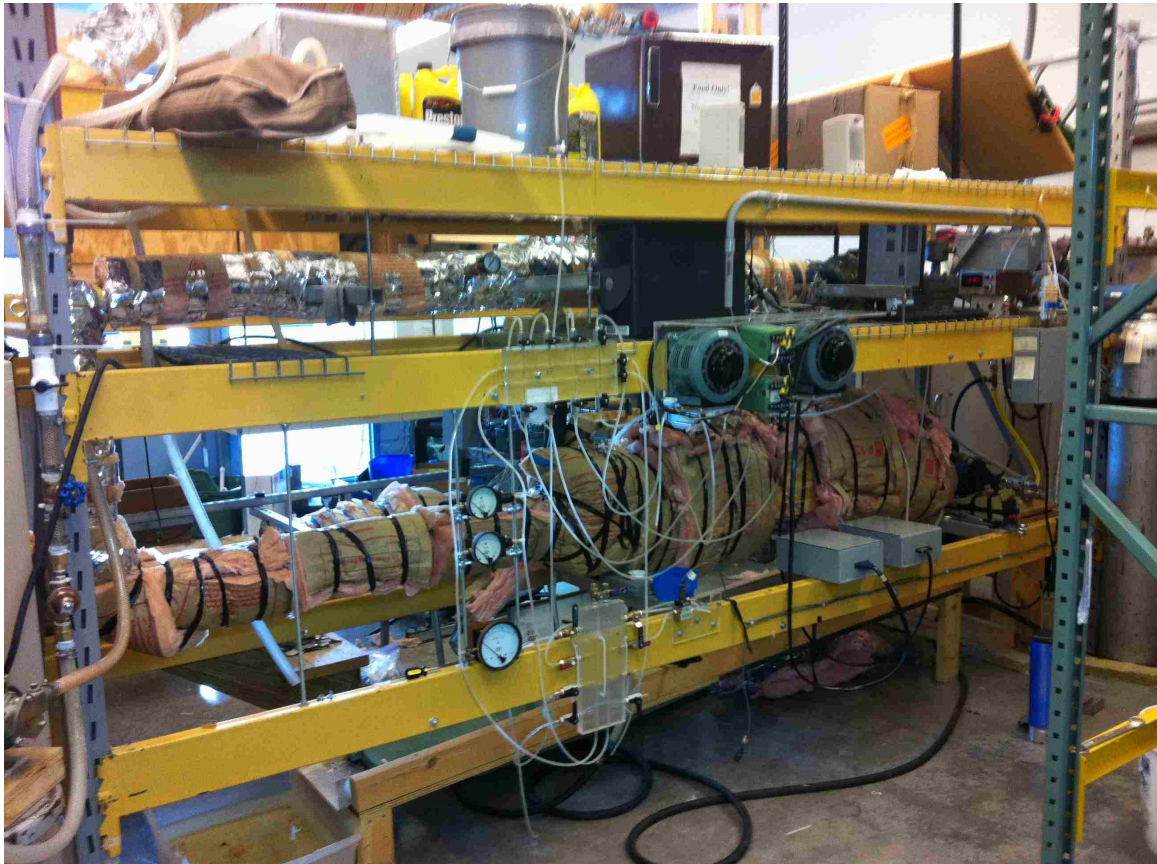


Figure 3.1: Photo of liquid loop test apparatus.

3/4 hp, 1,200 rpm motor. The pump and motor were mounted to a stand isolated from the rest of the apparatus and connected to the loop with rubber hoses to mitigate vibration as much as possible.

3.1.1.2. Flow meter. A Micro Motion R-series Coriolis flow meter was used to monitor the mass flow rate traveling through the closed loop. The meter was connected to a Micro Motion 2700 series transmitter, which was wired into the data acquisition system, details of which can be found in Section 3.1.3.1 below. The flow rate was controlled using a needle valve located just after the flow meter.

3.1.1.3. Heat exchanger for heat rejection. Heat rejection was accomplished using a shop-made concentric counter-flow heat exchanger. The heat exchanger was constructed by assembling a 40 in. long, $1\frac{1}{2}$ in. nominal diameter copper tube over a section of the flow loop with reducer fittings and tee's such that coolant could flow around the inner pipe, through which the loop fluid passed. The building cold water supply was used as the coolant, and was regulated up to a maximum of 2.4 gpm using a gate valve and rotameter.

3.1.1.4. Bleed valves. A bleed valve was placed at the highest point in the loop. It consists of a tee installed at a right-angle junction, instead of an elbow, and a short piece of pipe pointing upward with a valve installed. The valve is closed during loop operation, but may be opened for bleeding when necessary. This valve was also used to relieve the loop pressure due to expansion of the water during heating. Bleed valves were also installed in each settling chamber.

3.1.1.5. Inlet settling chamber. The inlet settling chamber consisted of a large rectangular duct made from welded $\frac{1}{4}$ inch thick plate aluminum. On the inlet side a fitting to receive the loop tubing was installed, and a flange was made on the outlet side onto which the test section was bolted. A groove was machined into the flange to accept a square rubber o-ring type gasket, which was secured in place with RTV silicone. Within the settling chamber were two screens placed before and after a section of honeycomb. The screens were made from 0.025 in. diameter stainless steel wires at ten wires per inch length and width. The honeycomb was a $1\frac{1}{2}$ in. thick section of aluminum honeycomb intended for use in composite board manufacture. The hexagon side length was approximately 1/10 in. giving a length-to-cell-diameter ratio of roughly 8.5.

The inlet settling chamber is rigidly mounted to a set of linear motion bearings which extend to the outlet settling chamber in such a way as to maintain alignment of the two chambers.

3.1.1.6. Test section. The test sections were machined from aluminum stock to represent a scaled-up, single channel in the representative heat exchanger shown in Figure 1.1. The scale factor was three, giving a channel width of 1.125 inch, height of 0.3 inch, and length of 26.5 inches. Once assembled, each test section was fitted with phenolic flanges at each end, the bolt pattern of which matched the respective settling chambers.

A detailed description of test section construction, instrumentation, assembly, and installation can be found in Section 3.1.2.

3.1.1.7. Outlet settling chamber. The outlet settling chamber was identical to the inlet settling chamber, and was bolted to the outlet side of the test section. Unlike the inlet settling chamber, which is fixed in place, the outlet settling chamber is mounted to a pair of $\frac{3}{4}$ in. linear motion bearings, allowing it to slide toward or away from the inlet settling chamber, while maintaining their alignment.

3.1.1.8. Building water supply connection. The loop was filled by the building water supply, which was connected via a tee after the outlet settling chamber. The water supply was regulated using a needle valve. Also present was a pressure gage with which to monitor the loop gauge pressure. The building line pressure was used to bring the loop operating pressure up to a nominal 10 psi for all experiments to prevent cavitation at the pump inlet.

3.1.1.9. Auxiliary heater. A Zerostart 330-5004 engine block heater was installed to aid in bringing the loop up to operating temperature more quickly. It had a maximum output of 2.5 kW and was controlled by a Powerstat S1002 variable autotransformer with a maximum rating of 2 kW. The heater's internal thermostat was bypassed so it would not shut off based on a preset fluid temperature, as it had been normally designed to do.

3.1.1.10. Recirculation loop. A recirculation loop was installed which, when opened, allowed a portion of the water in the loop to circulate from the pump outlet back into the pump inlet. The purpose for the recirculation loop was to lessen the burden on the

pump at very low flow rates by preventing a high pressure build-up between the pump and the flow-regulating needle valve.

3.1.2. Test Section Design, Fabrication, and Installation. Each test section consisted of two halves bolted together to form a complete channel. Each half was machined from a single piece of aluminum stock via a computer numerically controlled mill. Surface enhancements were machined into the long edge of each channel, and grooves were machined into the short edge of each channel to accommodate the seals and side wall insulators described below. A dimensional drawing of a typical test section half cross section is presented as Figure 3.2.

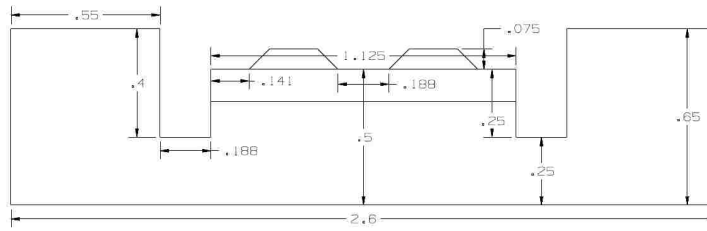


Figure 3.2: Liquid test section half geometry.

3.1.2.1. Thermocouple wells. Thermocouple wells were drilled along the centerline of both test section halves. They consist of a 1 mm hole drilled to within .010 inch of the bottom surface of the channel. This assured that the temperatures measured were as close as possible to the wall temperature at the surface. For convenience in installation, a clearance hole of diameter 0.067 in. was drilled to within 0.5 in. of the surface. A dimensional drawing showing a typical thermocouple well is presented as Figure 3.3.

Once the test sections were complete, thermocouples were cemented into the holes using Omegabond 600 high temperature chemical set cement.

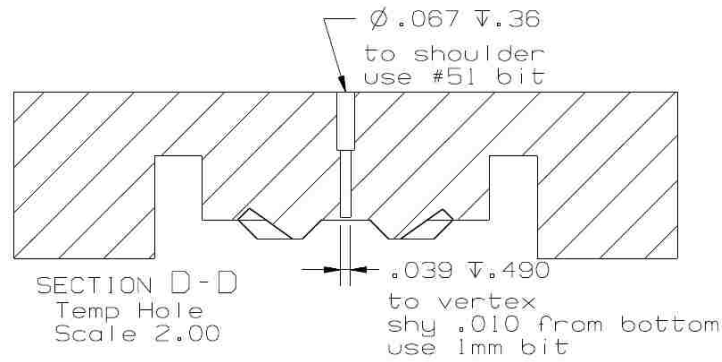


Figure 3.3: Thermocouple well geometry.

3.1.2.2. Pressure tap holes. The pressure tap holes were very similar to the thermocouple holes, except that they were drilled completely through the test section, allowing pressure to be measured. A dimensional drawing of a typical pressure tap hole is presented as Figure 3.4.

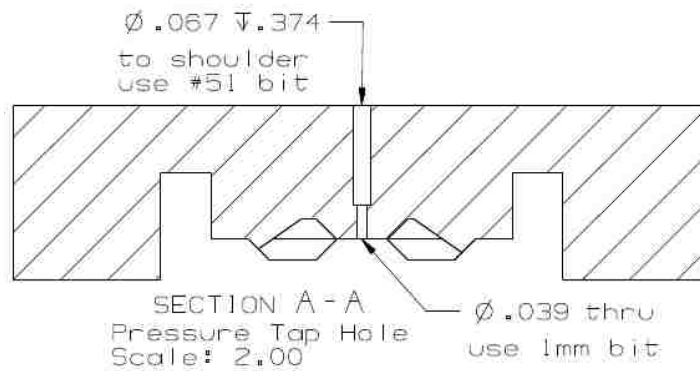


Figure 3.4: Pressure tap hole geometry.

Once the test sections were manufactured, tubes were installed into the pressure tap holes using J.B. Weld. The tubes consisted of a 0.065 in. O.D. steel tube mounted inside

a 0.065 I.D. copper tube, as shown in Figure 3.5. The tube allowed the pressure taps to be connected to the pressure transducer manifold during installation.



Figure 3.5: Pressure tap tubes which were mounted in pressure tap holes.

3.1.2.3. Seals and side wall insulators. The two shorter walls of each channel were insulated to promote 1-dimensional flow of heat from the heaters into the water. The side walls were machined out of $\frac{1}{4}$ inch phenolic to fit, along with rubber seals, into the grooves machined into the test section halves. More detail on the side insulators can be found in Section 3.1.2.6.

3.1.2.4. Heaters. Two custom mica etched foil heaters from Hi-Heat Industries were ordered, which were sized to precisely fit the test section halves, one for each channel half. In addition to being sized to the wetted portion of the channel, slots were made in the center to allow the thermocouple wires and pressure taps to pass through. The heaters were capable of delivering approximately 1.400 kW each, for a total of 2.8 kW to the test section. The heaters were very thin and delicate; they were, therefore, permanently installed between two aluminum plates which were machined to the same shape as the heaters. Each plate adjacent to the test section was cut from $\frac{1}{16}$ in. 6061-T6 aluminum, while the plate opposite the heater was cut from $\frac{1}{8}$ in. 6061-T6 aluminum. In addition, a layer of ceramic paper was placed between the heater and the outer plate, providing a softer and more even clamping surface, as well as creating a thermal barrier.

3.1.2.5. Flanges. At each end of the test section was a flange to accommodate bolting of the test section to the settling chambers. The flanges were machined from $\frac{1}{8}$ in. phenolic plate. Phenolic was used because of its machinability, thermal resistance, and strength. Each flange was drilled with the bolt pattern to match the settling chambers, and an opening was machined through which the tongue of the test section would fit snugly. A rabbet was also machined around the opening so the test section would be recessed slightly into the flange for added support. A photo of one flange is presented as Figure 3.6. Each flange was attached to the test section using high temperature RTV silicone and clamped by running long threaded rods through two pairs of the flange holes and bolting such that there was good tension and the flanges were square to the test section. If the flanges were not square, they would be stressed as they were installed and would likely leak. A photo of a flange installed on one end of a test section is presented as Figure 3.7.

3.1.2.6. Assembly. With the thermocouples and pressure tap tubes installed, the test sections were ready for assembly. Assembly proceeded in the following steps:

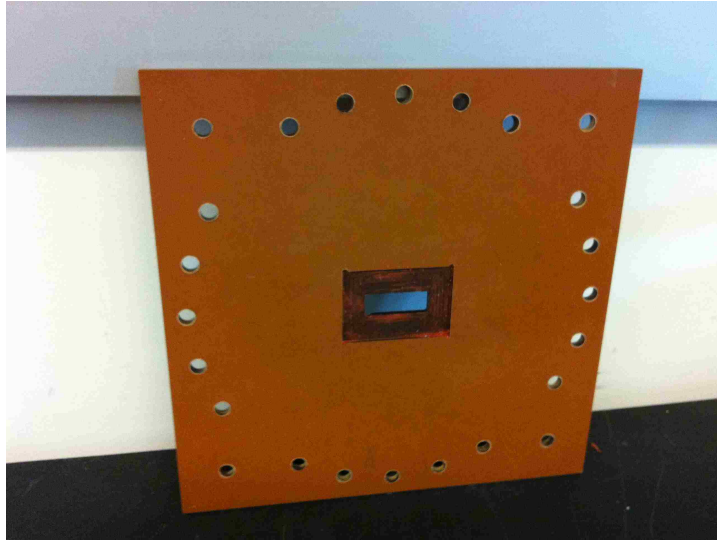


Figure 3.6: Flange for mounting test section to test apparatus.

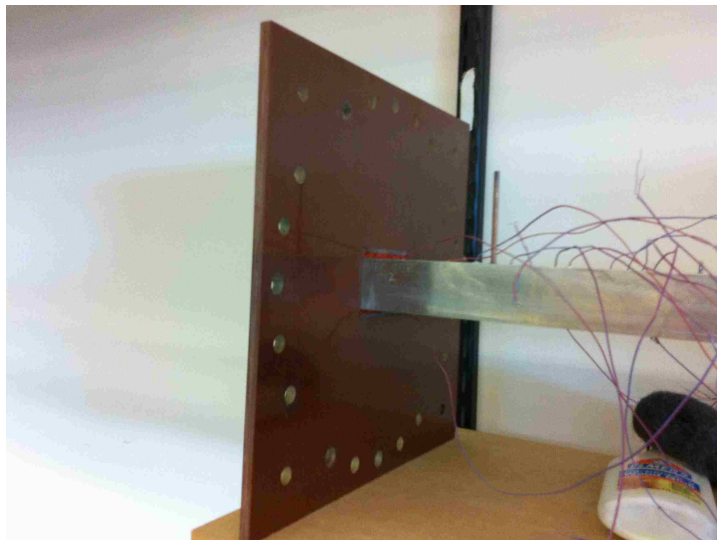


Figure 3.7: Flange mounted to test section.

1. *Assembled halves*: The bottom half was placed with the channel facing upward on supports to ensure the thermocouple wires were not damaged by sitting directly on the table. Two lengths of 0.139 in. diameter rubber sealing cord were installed, one in each groove. The two phenolic insulating side walls were then installed. Two more

lengths of sealing cord were then placed in the grooves in the top channel and held in slight tension while the top channel was carefully placed onto the bottom. Once the top channel grooves had received the phenolic side walls, tension was released and the top channel slid down to rest onto the bottom half. Thirty-six #8-32x1" socket head cap screws were then used to secure the two halves together, compressing the sealing cord. The cord was then trimmed to length and the assembly of the two halves was complete. Figure 3.8 shows an end view of a completely assembled channel.



Figure 3.8: End view of liquid test section channel.

- Installed heaters:* Once the halves were assembled, the two heater assemblies were installed, one each, on the top and bottom of the test section as follows: The assembled test section was placed on blocks with the top surface facing upward. The thermocouple wires were then pulled through the corresponding slot in the heater, as shown in Figure 3.9, and the heater was slid over the pressure tap holes to rest on

top of the test section. The test section was then flipped over and the other heater similarly placed. Installation was completed by using 34 #8-32x2” socket head cap screws with nuts to secure the heaters firmly in place.

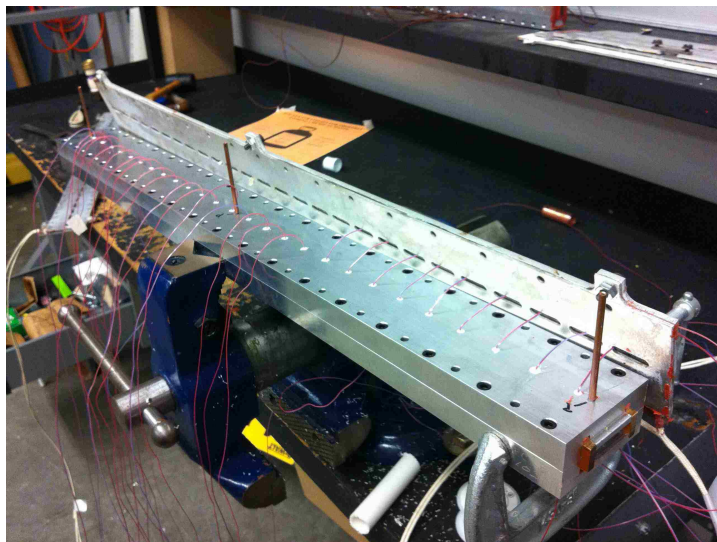


Figure 3.9: Pulling thermocouple wires through slots in heater.

- Installed flanges:* With the heaters installed, the flanges were ready to be installed as follows: The test section was placed on a block of such a height that the installed flanges would clear the bench once installed. The flanges were then test fit and sanded as necessary. Once everything was fitting well, RTV silicone was spread in a thin layer on both the flange and the test section surfaces. The flanges were then set in place and a long threaded rod placed through the lowermost hole in both flanges, and nuts installed. Care was taken at this step not to knock the flanges off of the test section. Use of small diameter threaded rod was beneficial to accomplish this. Another long threaded rod was placed through the uppermost hole in each of the two flanges and nuts installed. The nuts were then alternately tightened until both

were snug and the distance between the two flanges at each rod location was equal, thus assuring even clamping pressure and assisting in making the flanges square. The test section was then removed from the blocks and placed with the flanges resting on the bench, and both flanges were squared to the test section in all directions. Any variations from square were corrected, using a small rubber mallet when necessary. The RTV was allowed to dry and the threaded rods removed.

With the test section halves assembled and heaters and flanges installed, the test section was ready to be installed into the testing apparatus.

3.1.2.7. Installation. The outlet settling chamber was slid on the linear bearings so that it was as far away from the inlet settling chamber as possible. Blocks were placed across the rails to support the test section at the proper height. The test section was then placed on the blocks between the settling chambers so that it was resting against the inlet settling chamber. The outlet settling chamber was then moved so that it was just touching the test section flange. One bolt and washer was then threaded onto each end of three threaded rods. The bolts were threaded toward the middle of the threaded rods so as to fit between the flanges when installed. One of the threaded rods was then placed through the uppermost hole in the two flange pairs, such that it was spanning the entire test section. The other two rods were similarly installed in two of the bottom holes such that the three rods had the same number of flange holes between each of them. An additional washer and bolt were then threaded onto each end of the rods and tightened until the settling chambers were just snug against the test section flanges. The threaded rods served to keep the outlet settling chamber from sliding back when the loop was pressurized, thus preventing the phenolic from deforming and causing leaks. The inner bolts on the threaded rod were then tightened against the test section flanges, and nine bolts with nuts and washers installed in every other hole in each manifold. It was determined that it was not necessary to install a bolt in every hole. The installed test section can be seen in Figure 3.10.

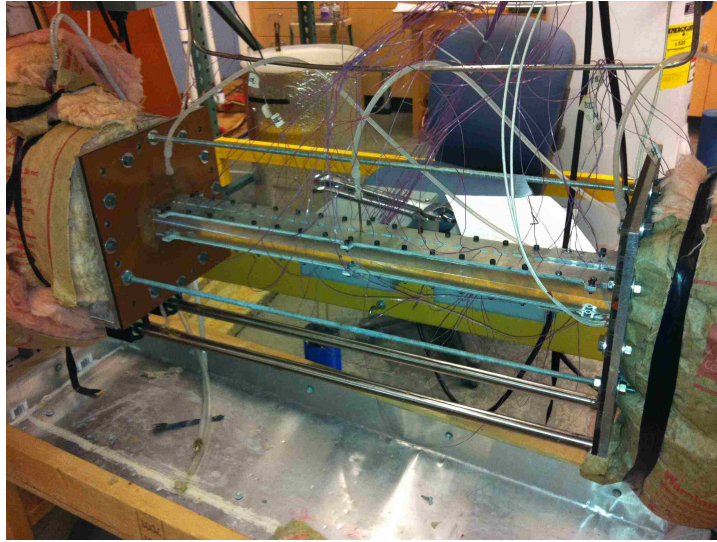


Figure 3.10: Test section installed in liquid loop.

Once the test section was installed between the settling chambers, the thermocouples were wired to the data acquisition card and their placement recorded. The pressure tap tubes were fitted with nipples, and rubber tubing was attached, which led to the respective manifold positions. The test section was then well insulated as described in the following section.

3.1.2.8. Insulation. The test section surface was insulated using one inch thick mineral wool insulation as shown in Figure 3.11. Mineral wool was chosen because of its ability to withstand high temperatures. Once the test section was covered with mineral wool, it was further insulated with standard R-13 home insulation, which was fitted into a clamshell-style box designed to go around the test section, as seen in Figure 3.12 as well as in Figure 3.11 mentioned previously.

Once the test section was fully insulated, the flanges were insulated by wrapping household R-13 insulation around them and securing it with vinyl tape. The gap in the top

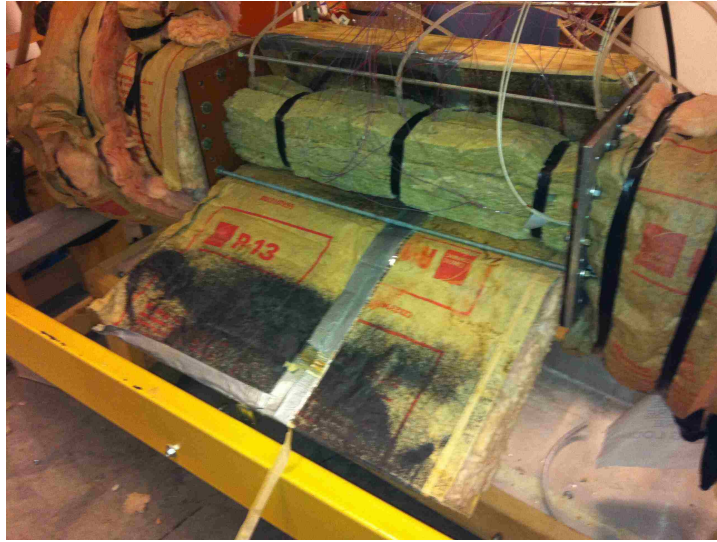


Figure 3.11: Mineral wool insulation around liquid test section.



Figure 3.12: Insulation clamshell installed around liquid test section.

of the clamshell was also insulated using another piece of R-13. The fully insulated test setup can be see in Figure 3.13.

3.1.3. Instrumentation. The following sections describe the various pieces of instrumentation used in the liquid flow loop, beginning with the flow meter.



Figure 3.13: Fully insulated liquid test section.

3.1.3.1. Flow meter. Since Reynold's number was critical to the data reduction process, it was important to have accurate measurements of mass flow rate and fluid density. A Micro Motion R025 Coriolis flow meter was used in conjunction with a Micro Motion 2700 series transmitter to measure both quantities. Each quantity was output on a 0-10 V scale. The meter and transmitter combination is accurate to $\pm 0.5\%$ of the mass flow reading within its range of 0 to 0.38 kg/s.

3.1.3.2. Differential pressure gauge. Differential pressure measurements were made using a Validyne DP15-26 pressure transducer connected to Validyne CD-23 carrier demodulator, which had an accuracy of $\pm 0.25\%$ of its full scale reading of 1.4 in.w.g. Through the use of a manifold, each pressure tap on the test section could be applied to either the high or low side of the transducer. The inlet and outlet settling chambers also had pressure taps installed which could be applied to the high and low sides of the transducer, respectively. The pressure measurement setup is presented as Figure 3.14.

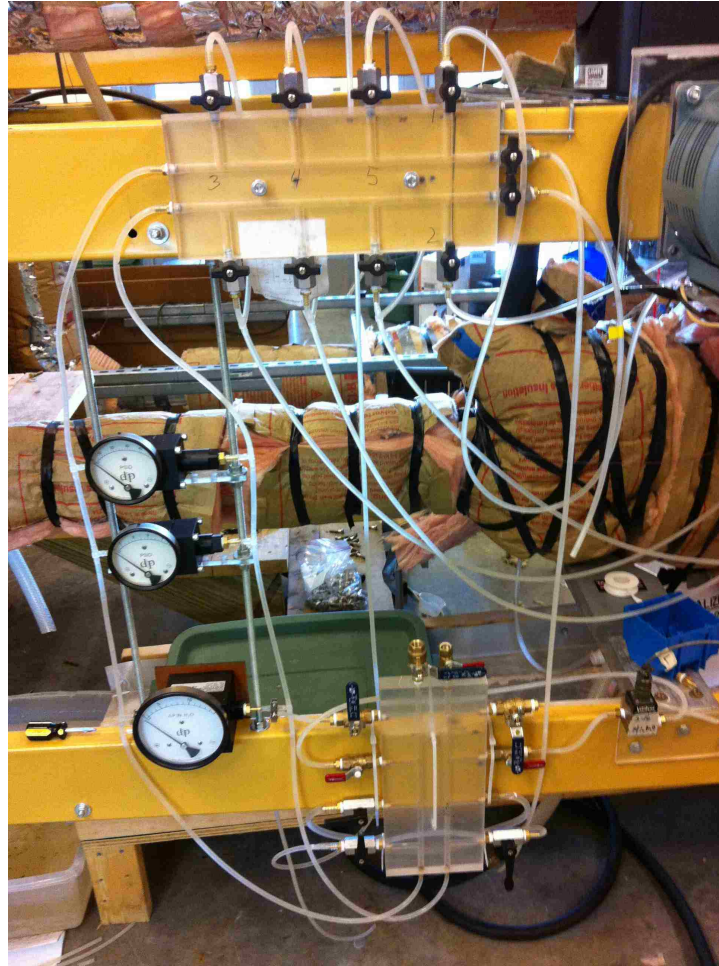


Figure 3.14: Pressure measurement setup for liquid loop.

3.1.3.3. Test section heater power control and monitoring. The power to the each of the two test section heaters was varied using a Powerstat 136B variable autotransformer, and was monitored using a Ohio Semitronic GW5-019DY01 AC watt transducer. The watt transducers had an accuracy of $\pm 0.2\%$ of the reading, or $\pm 0.04\%$ of full scale voltage, and did output 0 - 10 V linearly withing the operating range of 0 to 2,400 W.

3.1.3.4. Thermocouples. Standard 30 gage ANSI type-T (copper-constantan) thermocouples were used for both fluid and surface measurements. They were manufactured using a THERMX Model 258B thermocouple welder with argon as the shielding gas.

The fluid thermocouples were prepared, once welded, first by dipping them in Dow Corning I-2577 Conformal Coating. They were then fed through a short length of $\frac{1}{8}$ in. O.D. copper tubing so the bead protruded just past the end. They were then held in place and further sealed by RTV silicone to waterproof them. Omegalok SSLK compression fittings were used to mount the tubing to the apparatus.

The inlet settling chamber contained four thermocouples evenly spaced throughout, and the outlet settling chamber contained two thermocouples, which were strategically placed so that the fluid coming out of the test section would flow over them soon after exiting. Thermocouples were also placed, one each, in tees in the copper tubing running into the inlet settling chamber and out of the outlet settling chamber.

The test section wall thermocouples, once welded, were dipped in Dow Corning I-2577 Conformal Coating to electrically insulate them from the test section once installed. The installation of test section wall thermocouples is discussed in Section 3.1.2.

Each thermocouple was wired to one of two National Instruments CB-68-LPR connecting blocks in Non-Reference Single Ended (NRSE) mode. Each connecting block was installed in a well insulated electrical box. All thermocouple measurements were referenced to an ice bath, one for each box, to mitigate any error due to temperature variations at the terminal block. Preparation of the ice baths were in accordance with ASTM [1981].

3.1.3.5. Data acquisition system. Two LabView programs were used in operation of the loop. The first, which was used as the loop was coming to steady-state, monitored the bulk inlet and outlet temperatures, as well as the heater wattages, wall temperatures, and pressure drop in real-time. An example of the program's front panel can be seen in

Figure 13. Once the loop had come to steady-state, the second program was used to record the data. All data was recorded at 1000 Hz for 30 seconds.

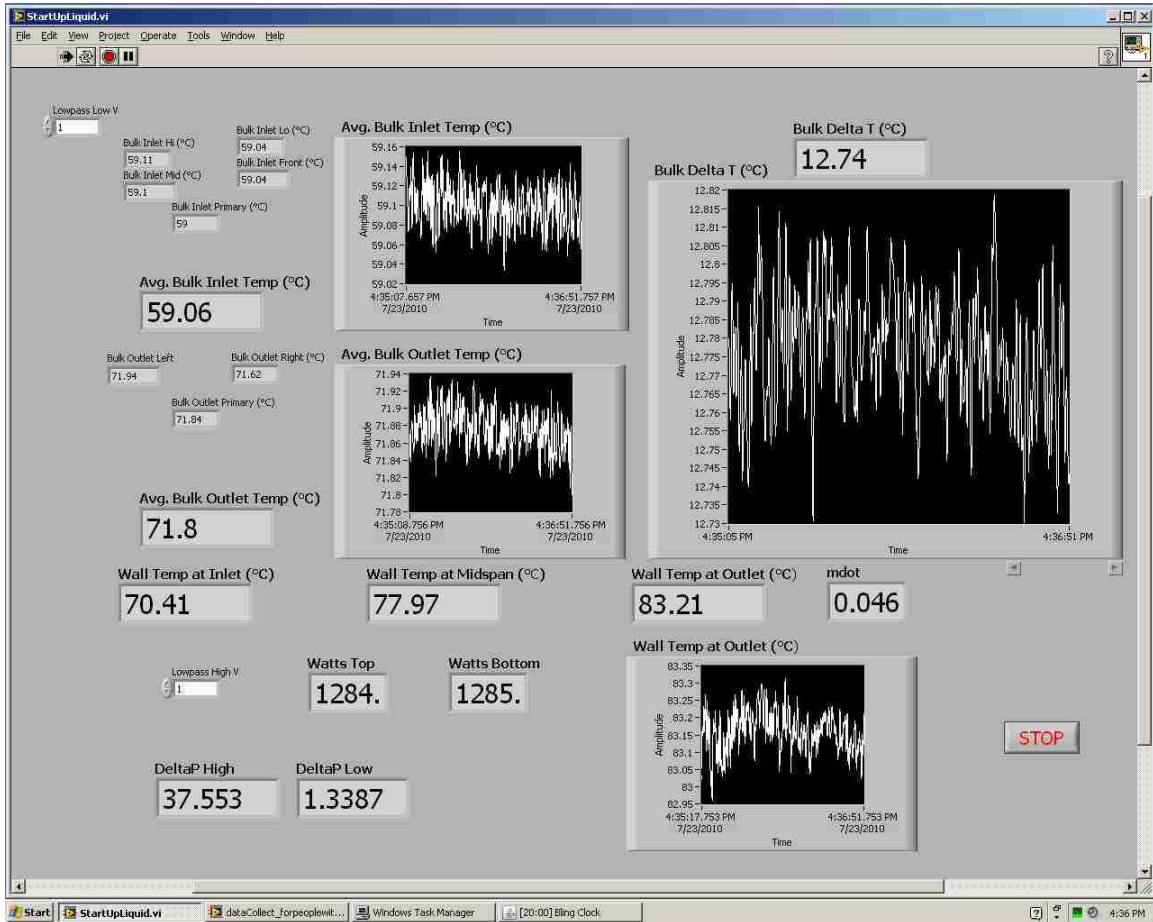


Figure 3.15: LabView front panel for liquid loop start-up.

3.1.4. Liquid Test Section Surface Geometries. This section discusses the surface geometries used for each of the four liquid test sections. They were numbered WFC###, where WFC stands for Water Fin Channel. Each section is described in detail below:

3.1.4.1. Water fin channel 000. WFC000 was a smooth, rectangular channel of width 1.125 inch and height 0.3 inch, with no surface enhancements. It was to be used as a

baseline for comparison with the enhanced geometries, as well as to validate the test setup by comparison with published results.

3.1.4.2. Water fin channel 010. WFC010 was a bumped test section. The bumps spanned the most of the width of the test section, ending 0.141 inches inside of each side wall, as shown in Figure 3.16. The cross section of the bumps, including dimensions, is presented as Figure 3.17.

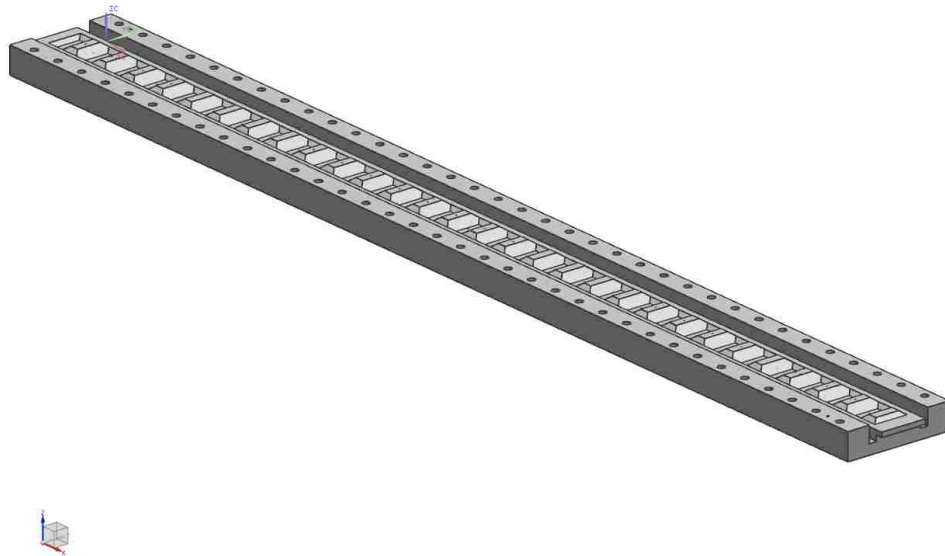


Figure 3.16: WFC010 test section half.

3.1.4.3. Water fin channel 012. WFC012 was identical to WFC010, except that the bumps were shorter. Since the bump angle was the same, the flats on the peaks and valleys were also longer. The cross section of the WFC012 bumps, including dimensions, is presented as Figure 3.18.

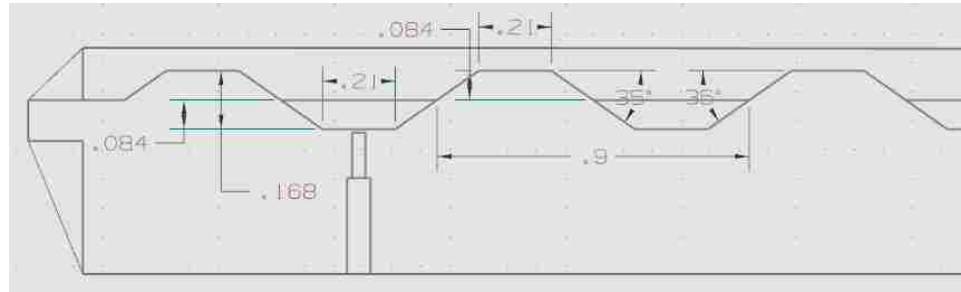


Figure 3.17: WFC010 bump geometry (dimensions are in inches.)

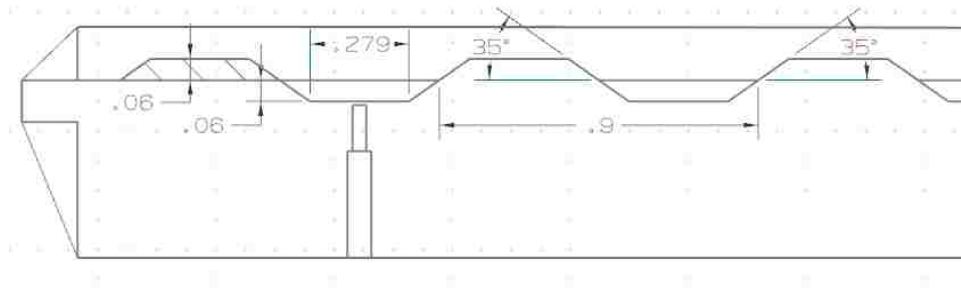


Figure 3.18: WFC012 bump geometry (dimensions are in inches.)

3.1.4.4. Water fin channel 103. For WFC103, a new approach was studied. For this test section, the bumps were meant to resemble rifling, inducing a rotation in the bulk flow. The bumps were similar to those in WFC010, except that they were turned 45 degrees to the flow. The bumps on the top of the channel were rotated so they were perpendicular to those on the bottom, creating the desired rifling. Instead of having the bumps span the entire width of the test section, a valley was left in the middle so that the overlapping bumps would not cause a significant area restriction. One test section half is presented as Figure 3.19, and the half-bump geometry is shown, with dimensions, as Figure 3.20.

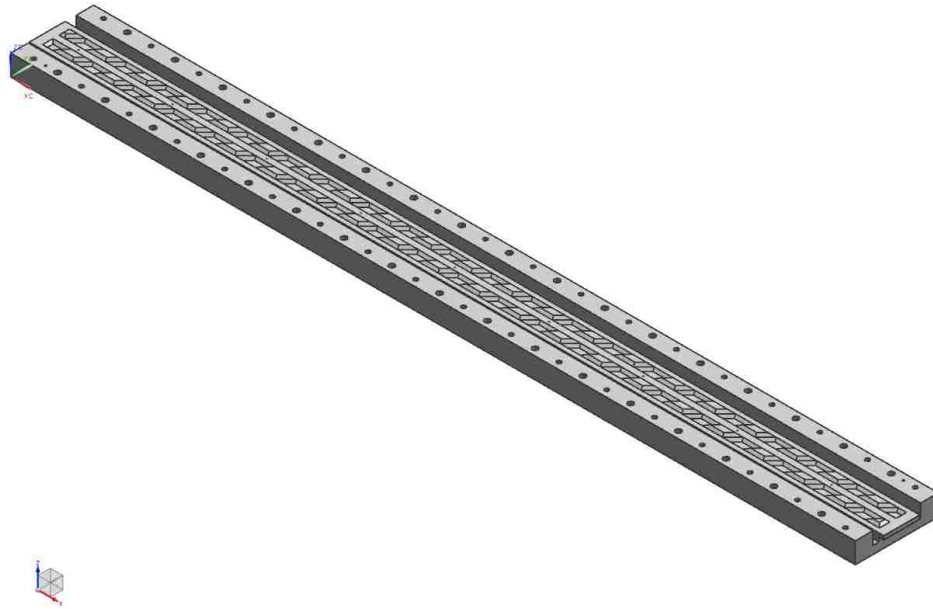


Figure 3.19: WFC103 test section half.

3.2. AIR LOOP

The experimental apparatus consisted primarily of a closed loop through which air was recirculated through the heated test sections as well as an optional heat recovery ventilation (HRV) unit for heat rejection. The loop, along with supporting instruments, were mounted to a 10 foot long pallet rack for convenience. The apparatus was constructed and first used by Rucker [2007], though some minor modifications were made to accommodate the current research. A photo of the entire apparatus is presented as Figure 3.21. Each portion of the apparatus is described in more detail in the following sections.

3.2.1. Flow Loop. The loop was constructed primarily of clamp-together six-inch diameter sheet metal ducting from K&B Duct. Exceptions were just before and after the pump, which was two-inch rubber hose, and between the outlet settling chamber and the

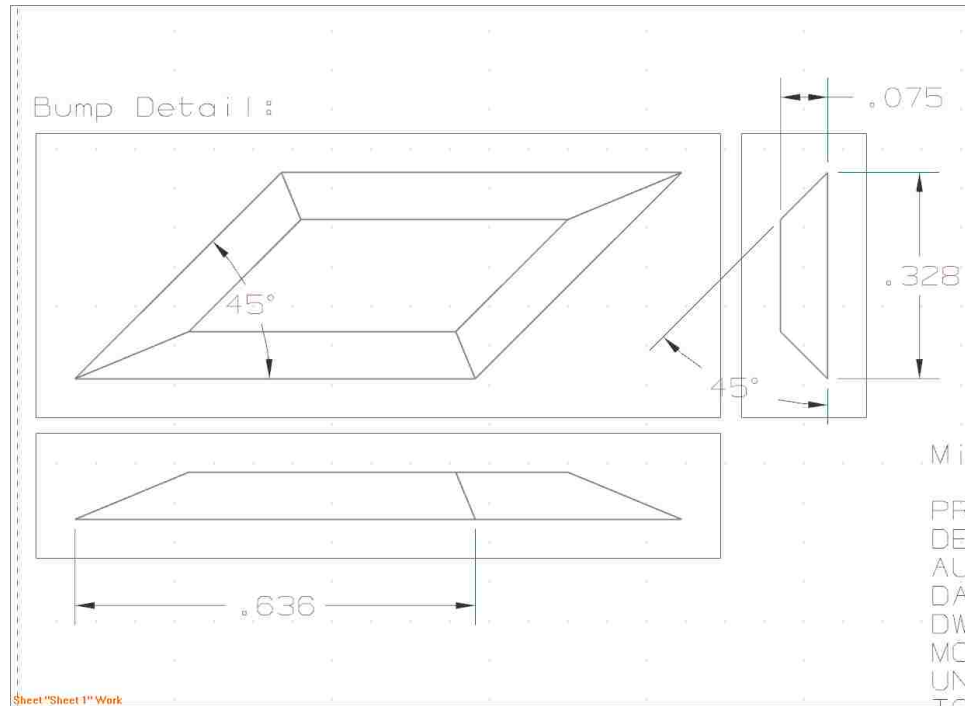


Figure 3.20: WFC103 half-bump geometry (dimensions are in inches.)

orifice flow meter, which was six-inch diameter PVC pipe to ensure there were no leaks in that section.

The subsections below describe each portion of the loop in the order of air flow, starting with the blower.

A schematic of the loop is presented as Figure 3.22.

3.2.1.1. Blower. A blower was placed in the upper corner of the loop to drive the flow. It was an Ametek model 116637M, with a maximum volumetric flow rate of 100 cfm. It could overcome up to a 6750 Pa static pressure loss. The blower was configured to receive two inch rubber hose, so a reducer was placed just before the blower to transition from the six inch loop ducting. Two inch rubber hose was then used to secure the blower to the loop. A 2-inch PVC gate valve was placed just after the blower to regulate the air flow



Figure 3.21: Photo of air loop test apparatus.

through the loop. An expander was placed after the throttling valve to transition from the 2-inch rubber hose back to the 6-inch ducting.

3.2.1.2. Heat recovery ventilator (HRV). The heat recovery ventilator was a Nu-Air Ventilation Systems model NU120-2 with aluminum core. The HRV warmed incoming air some, but due to its inefficiency the incoming air was not as warm as the exhaust air, thus mimicking closed-loop heat rejection.

3.2.1.3. Inlet settling chamber. The inlet settling chamber was an eight-inch wide by 6 inch tall plexi-glass duct containing four screens and a section of honeycomb for flow conditioning. The screens had a wire diameter of 0.011 inch with a mesh count of 18x16

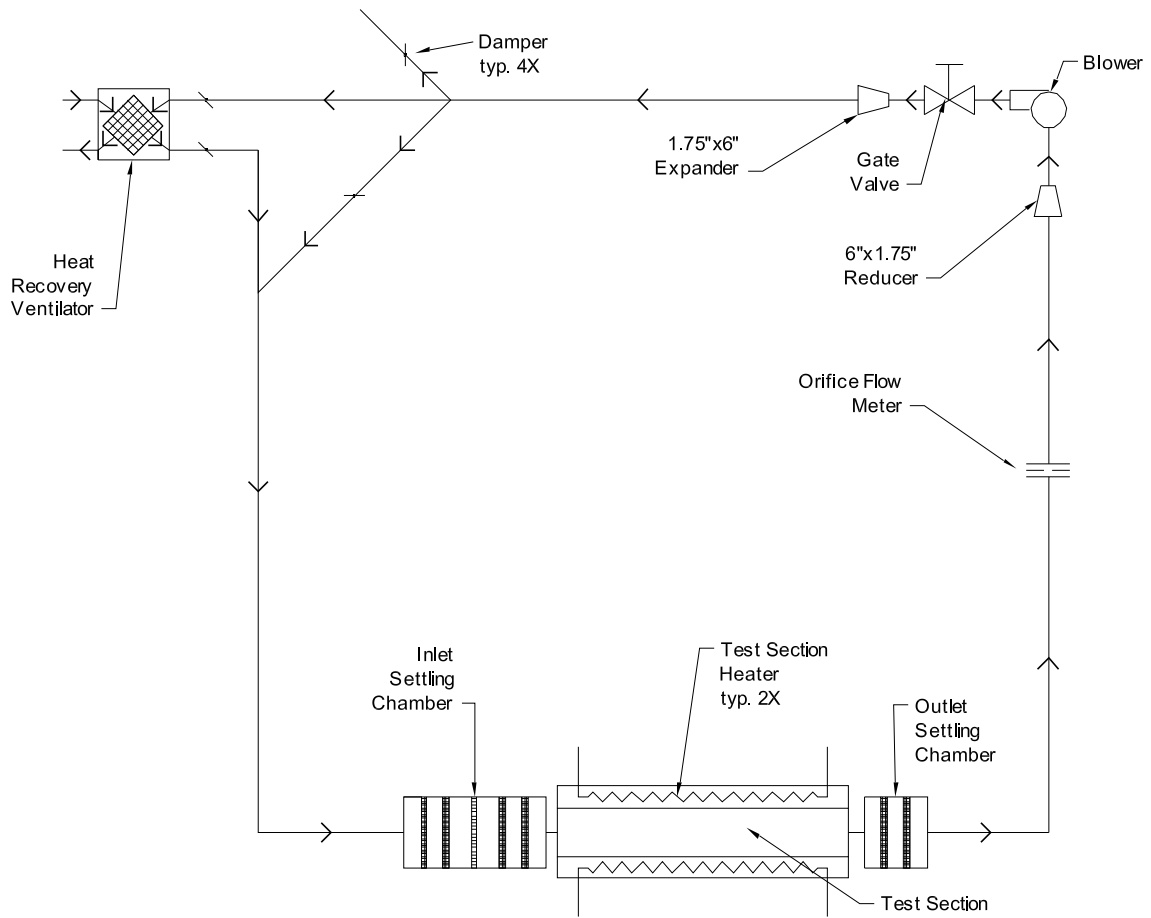


Figure 3.22: Schematic of air loop test apparatus.

wires per inch and were made of aluminum. Rucker [2007] chose the design. A schematic is presented as Figure 3.23.

3.2.1.4. Test section. The test section was machined from aluminum to represent a scaled-up, single channel in the representative heat exchanger. The scale factor was 10, giving a channel height of 3.75 inches, width of 1 inch, and length of 36 inches. Each of the four sides of the rectangular channel were fitted with a heater.

A detailed description of test section construction, instrumentation, assembly, and installation can be found in Section 3.2.2.

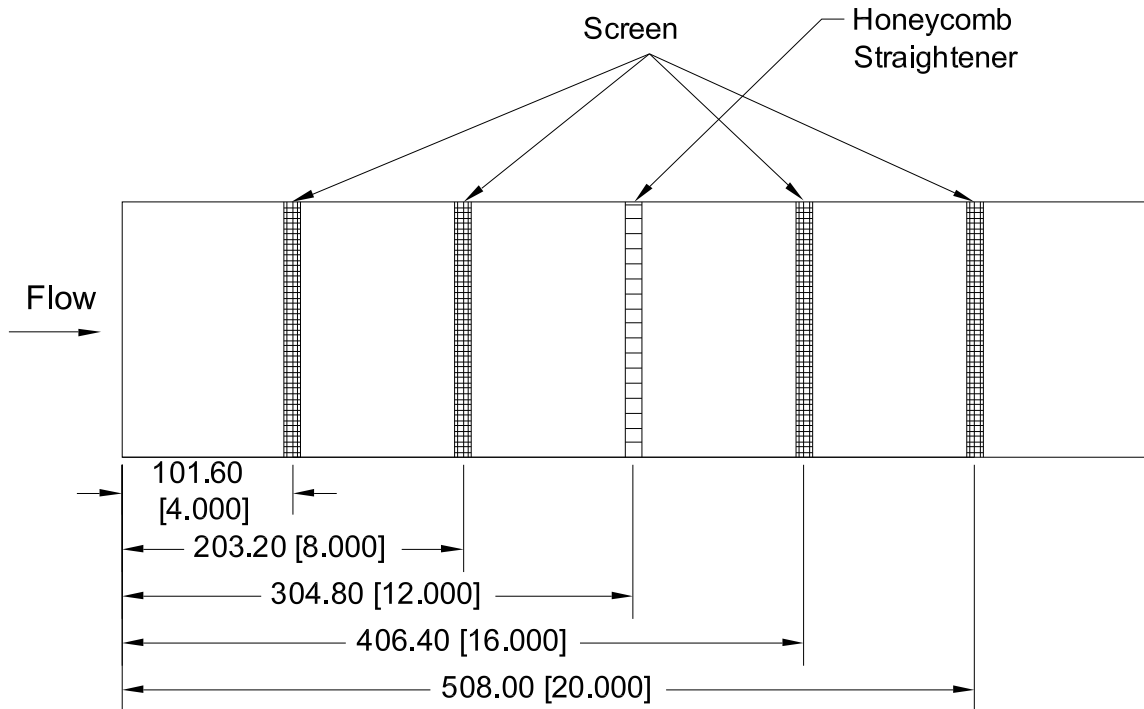


Figure 3.23: Schematic of inlet settling chamber, dimensions in mm [inches].

3.2.1.5. Outlet settling chamber. The outlet settling chamber was constructed similarly to the inlet settling chamber, except it only included two screens, also spaced four inches apart, and no honeycomb. The outlet settling chamber was 10 inches wide by 6 inches tall.

3.2.1.6. Orifice plate flow meter. After exiting the outlet setting chamber, the flow passed through a 1.0917 inch diameter quadrant-edged orifice plate flow meter, which is described in more detail in Section 3.2.3.1.

The flow then returned to the blower, and the loop was complete.

3.2.2. Test Section Design, Fabrication, and Installation. The test sections consisted of two major parts: The top and bottom pieces were generic, and were re-used on each test section assembly, while the sides featured the destabilizing geometry and were

changed. Because of the limitations of the travel of the CNC machine used to manufacture each piece, it was not possible to make each side in one piece. The sides, therefore, were manufactured in two pieces, and the top and bottom were manufactured from three pieces each. In this way, the joints were staggered and the assembly held itself together once fasteners were installed.

The following subsections describe in more detail the construction, assembly, and installation of the test sections.

3.2.2.1. Construction of sides. Each set of sides was first drawn in UGS NX in 3-D. The drawings were then used to CNC mill the destabilizing geometry into the sides, as well as drill and, where applicable, tap all fastener holes, thermocouple wells, and pressure tap holes.

3.2.2.2. Thermocouple wells. Thermocouple wells were machined along the center of each side, as well as the top and bottom of each test section. The exact linear placement varied due to geometry considerations. The side onto which the primary flow destabilizers were machined contained approximately 30-40 thermocouples over its length. The geometry of the thermocouple wells were identical to those in the experiments involving water, as described in Section 3.1.2.1.

3.2.2.3. Pressure tap holes. Three pressure tap holes were machined into the top segments, such that when assembled they were located near the inlet, center, and outlet of the test section. The pressure tap holes were also identical to those used in the experiments involving water, as described in Section 3.1.2.2.

3.2.2.4. Heaters. Each of the four sides of the test section had a heater installed. The heaters were etched-foil type with silicone rubber insulation. The heaters had a capacity of 2.1 W/in^2 and a maximum operating temperature of 200°C . The heaters were sandwiched between two $\frac{1}{8}$ inch aluminum plates before being bolted to the sides of the test section. The heaters and aluminum plates had slots and holes cut in them to allow the thermocouple wires and pressure taps to pass through.

3.2.2.5. Flanges. The test section flanges were machined from $\frac{1}{4}$ inch phenolic plate. A rectangle was machined in the middle to receive the test section, and a bolt pattern was drilled to match the inlet and outlet test sections, similarly to the flanges for the water test sections.

3.2.2.6. Assembly and installation. The test sections were assembled by bolting the top and bottom sections to the side section to form a rectangular channel. The fasteners used were 8-32x1/2" socket head cap screws. Ceramic paper was placed between the sides and the top and bottom to prevent heat from conducting between them as much as possible. Thermally conductive paste was applied at the joint of each side section and the joint of each of the top and bottom sections to allow heat to travel more readily across the joints, simulating an unbroken section. The assembly and installation process for each test section proceeded as follows:

1. *Assembled test section:* The sides were placed in the correct order on the bench. Thermal paste was applied to the joints, and the pieces butted together and placed the correct distance apart, as shown in Figure 3.24. Ceramic paper was then cut and placed on top of the sides in preparation for bolting on the top sections. The top sections were then bolted on one at a time, and thermal paste applied at all joints. Figure 3.25 shows a top piece being installed onto the sides. The test section was then flipped over and placed on blocks to protect the top thermocouples and pressure taps. Once the test section was flipped over, the bottom sections could be installed. It was slightly easier to line everything up properly if the center bottom section was installed before the two end sections, as shown in Figure 3.26.
2. *Installed flanges and installed test section in loop:* Once the test section was assembled, the flanges were glued to each end using high temperature RTV silicone. A thin, even layer of silicone was spread on each flange, and another on each mating test section surface, and the flanges pressed into place. The test section was still



Figure 3.24: Test section sides prepared for assembly.

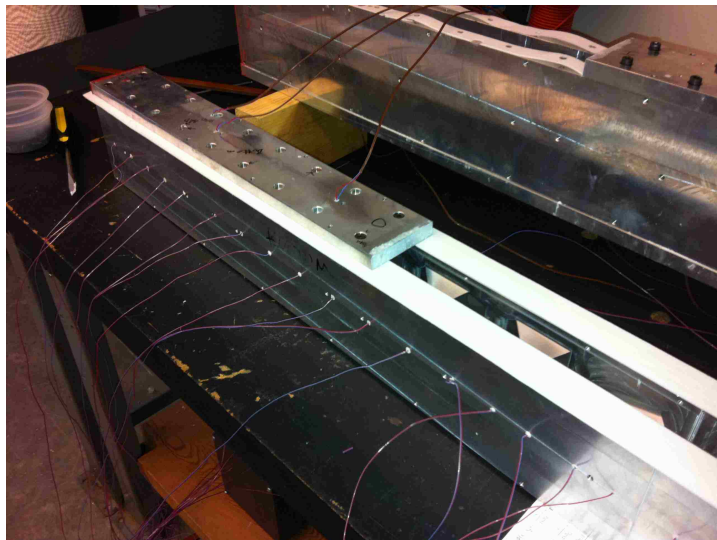


Figure 3.25: Installing top section onto sides.

on blocks, which prevented the flanges from contacting the bench. The test section was then carefully placed into the flow loop between the inlet and outlet settling chambers, and threaded rod used to clamp the settling chambers to the test section. The blower was turned on to ventilate the test section as the RTV was allowed to

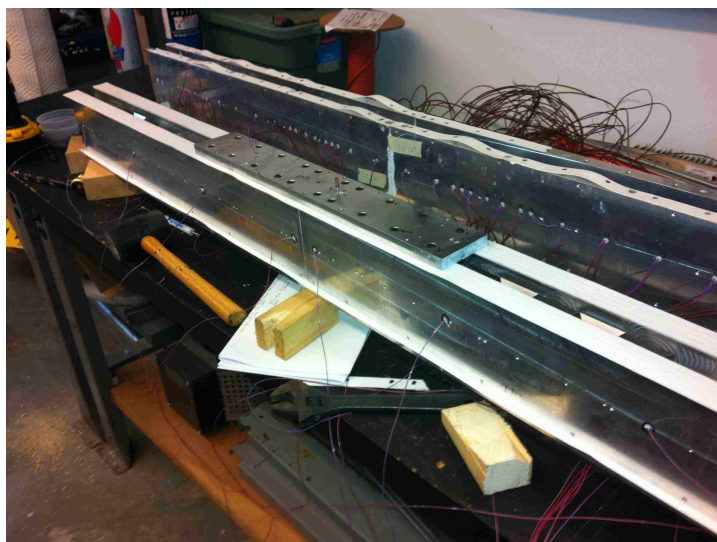


Figure 3.26: Installing bottom section onto sides.

dry. While the RTV was drying, the rest of the bolts were installed on the flanges to complete installation of test section into the flow loop.

- 3. Installed heaters:* Once the test section was installed in the flow loop, the heaters were installed. Each heater was fastened using #6-32x1/4" socket head cap screws around the edges, as well as #6-32x3/8" socket head cap screws with washers along the center. Figure 3.27 shows the position of the fasteners. One fastener was also used to secure a ground wire from the test section to the test apparatus frame to ensure that any shorts of the heater to the test section were immediately grounded and would not present a risk to the operator.
- 4. Hooked up thermocouple wires and pressure taps:* The thermocouple wires were then installed on the data acquisition card and their positions recorded. The pressure taps were also connected to the pressure gauge manifold using rubber tubing.

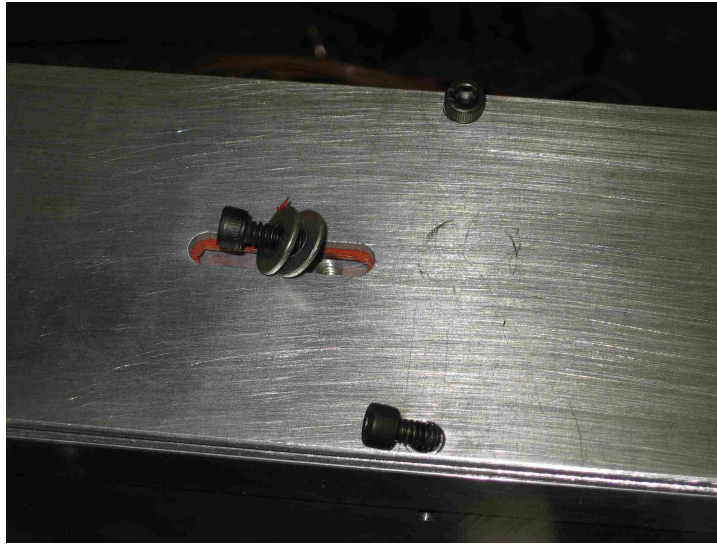


Figure 3.27: Fasteners used to mount heaters.

With the test section assembled and the heaters installed, the test section was ready to be insulated.

3.2.2.7. Insulation. The test section was insulated first with one inch thick mineral wool insulation and then wrapped in household R-13 insulation, similar to the tests involving water. The inlet and outlet settling chambers were then insulated with household R-13 insulation. Care was taken to ensure all surfaces were covered and well insulated, including the bottom and the flanges. A picture of the fully insulated test section is presented as Figure 3.28.

3.2.3. Instrumentation. The instrumentation used in the experimental setup were the flow meter, pressure gauge, test section heater controls, watt transducers for heaters, thermocouples for temperature measurement, and a data acquisition system. Each piece of instrumentation is described in more detail in the following subsections.

3.2.3.1. Flow meter. The flow meter was a 1.0917 inch diameter quadrant-edged orifice plate flow meter, which accommodated flow measurement from 1 to 29.5 cfm, with



Figure 3.28: Fully insulated air test section.

a corresponding pressure drop of 0.0023 to 2 in. w.g. The orifice plate was mounted in the loop between two PVC holding blocks and two 150# ANSI flanges. Each interface also included a Buna-N gasket. A schematic of the orifice mounting set-up is included as Figure 3.29. The pressure difference across the orifice plate was measured using a Dwyer Micrometer manometer as described in the following section.

3.2.3.2. Pressure gauge. The pressure gauge used was a Dwyer Micrometer manometer, which had a maximum pressure difference reading of 2 in. w.g., with an uncertainty of ± 0.00025 in. w.g. A manifold was constructed which allowed the gauge to measure the pressure drop across the orifice flow meter or to measure the pressure drop across any two test section pressure taps by adjusting the valves on the manifold. A schematic of the pressure measurement set-up is presented as Figure 3.30.

3.2.3.3. Test section heater control. The test section heaters were controlled using two Superior Electric 116C variable transformers to vary the voltage, and thus heater power.

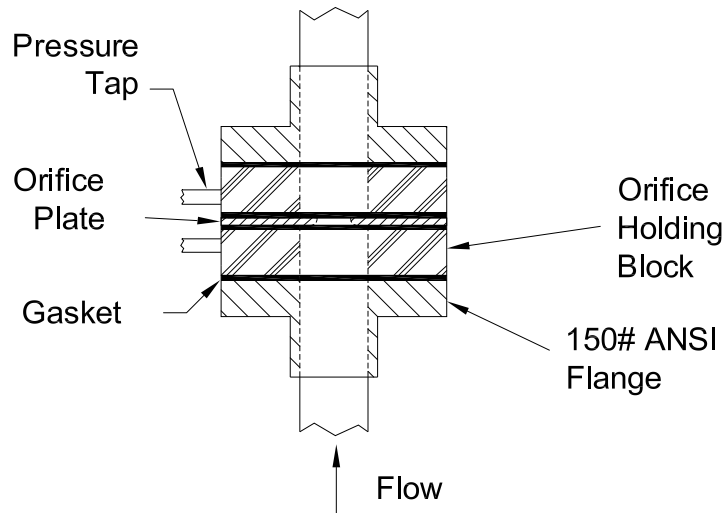


Figure 3.29: Schematic of orifice plate installation.

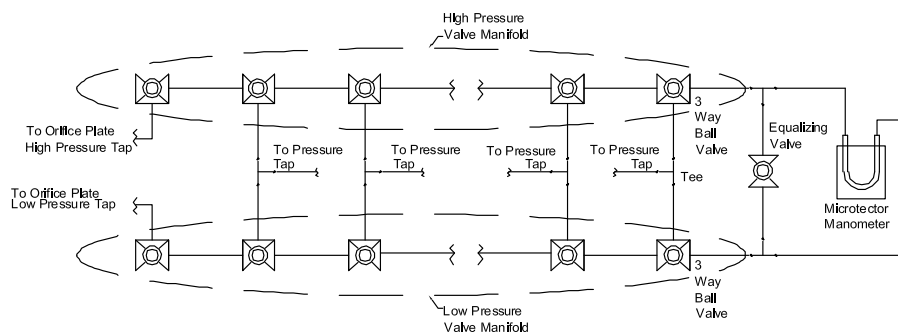


Figure 3.30: Schematic of pressure measurement system.

3.2.3.4. Watt transducers. The watt transducers which were used to measure heater wattage were model GW5 from Ohio Semitronics. They had an accuracy of $\pm 0.2\%$ of the reading plus $\pm 0.04\%$ of full scale wattage. The output of each transducer was 0-10 VdC, corresponding linearly with its range of 0-1200 W.

3.2.3.5. Thermocouples. Each settling chamber had eight thermocouples evenly spaced in a plane perpendicular to fluid flow. The average of the eight thermocouples gave a good approximation of the bulk air temperature.

The test section thermocouples were identical to those used in the experiments involving water, described in Section 3.1.3.4.

3.2.3.6. Data acquisition system. Similarly to the experiments involving water, one program was written to monitor the experiment until steady state was reached, and another was used to collect the data. The data collection program was identical to the one used in the experiments involving water.

3.2.3.7. Room air temperature and relative humidity measurement. The room air temperature and relative humidity were measured using a TH Pen model 8708 digital thermo-hygrometer.

3.2.3.8. Room barometric pressure. The room barometric pressure was measured using an Omega model EWS-BP-A barometric pressure transmitter, which was calibrated to output a voltage between 1-5 VdC, corresponding linearly with its range of 20.8-32.0 inches of mercury.

3.2.4. Air Test Section Surface Geometries. This section discusses the surface geometries used in the three air test sections. Section SFC010 was a bumped plain bumped geometry, while SFC020 and SFC021 were LVG geometries with differing dimensional characteristics. Each test section is described in detail in the following subsections.

3.2.4.1. Scaled fin channel 010. The surface enhancements on SFC010 were similar to those on WFC010, but scaled up by $\frac{10}{3}$. Figure 3.31 shows the inlet portion of the enhanced side of the channel. The outlet portion is similar, and continues the same bumps. The opposite side of the channel is a reverse image of the first. Thus, when one side has a bump, the other has a valley, thus maintaining a constant cross-sectional area. The bump dimensions are shown as Figure 3.32.

3.2.4.2. Scaled fin channel 020. The surface enhancements on SFC020 were periodic LVG patches. The inlet portion of the enhanced side is shown as Figure 3.33, and the outlet portion is shown as Figure 3.34. All lvg's are 0.335 inches tall, with a 45° slope. Again, the opposite side has valleys to match the LVG bumps on the enhanced side.

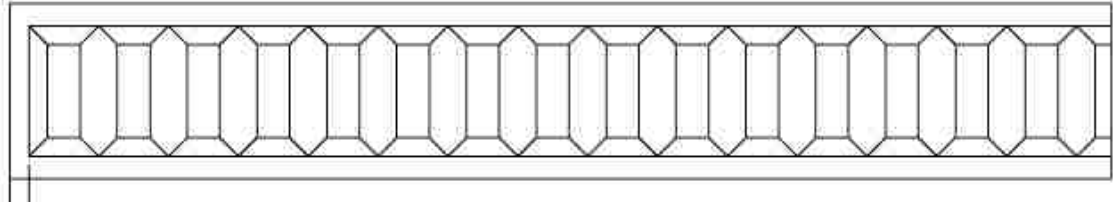


Figure 3.31: Side of SFC010 test section, showing bumps.

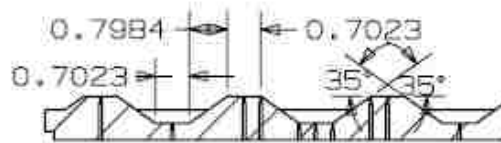


Figure 3.32: SFC010 bump geometry, with dimensions.

3.2.4.3. Scaled fin channel 021. The enhancements on SFC021 were LVG patches as well, but this time the LVG geometry was different. The inlet portion of the enhanced side is shown as Figure 3.35, and the outlet portion is shown as Figure 3.36 All lvg's are 0.335 inches tall, with a 45° slope. To reduce machining time and material cost, and since it was assumed that the difference would be negligible, the unenhanced surface from SFC020 was re-used for SFC021.

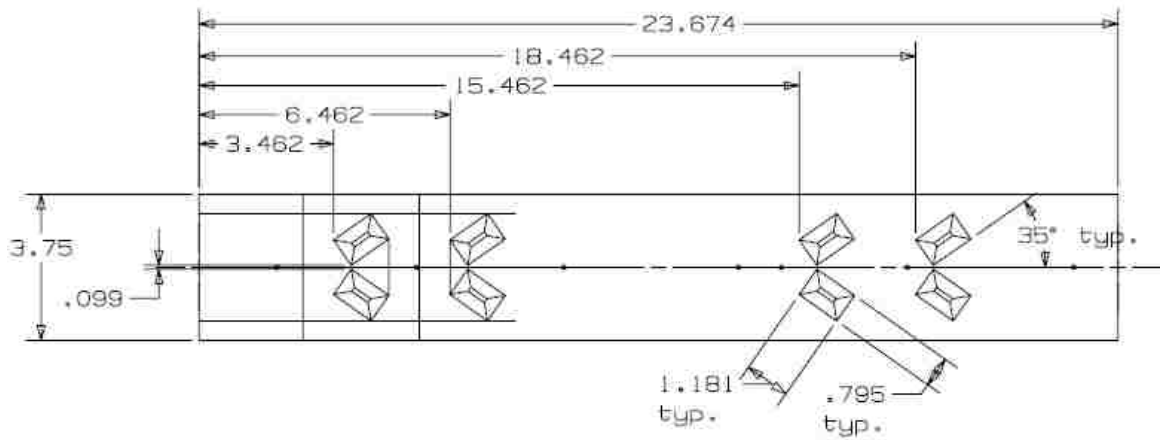


Figure 3.33: SFC020 side geometry, for the inlet portion of the duct.

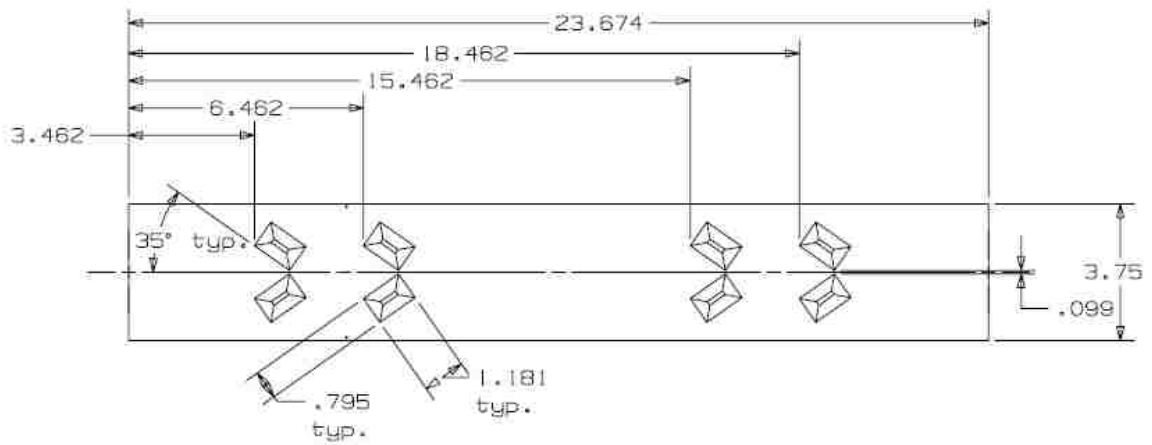


Figure 3.34: SFC020 side geometry, for the outlet portion of the duct.

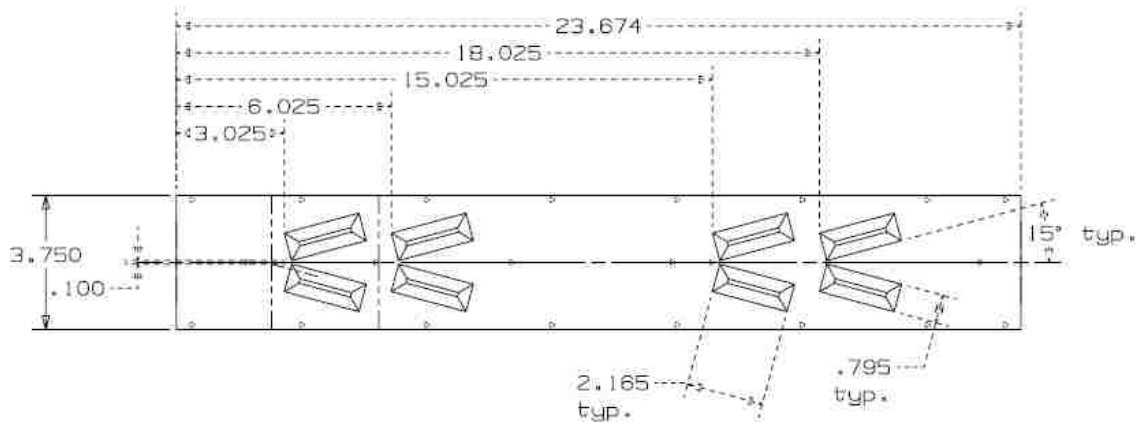


Figure 3.35: SFC021 side geometry, for the inlet portion of the duct.

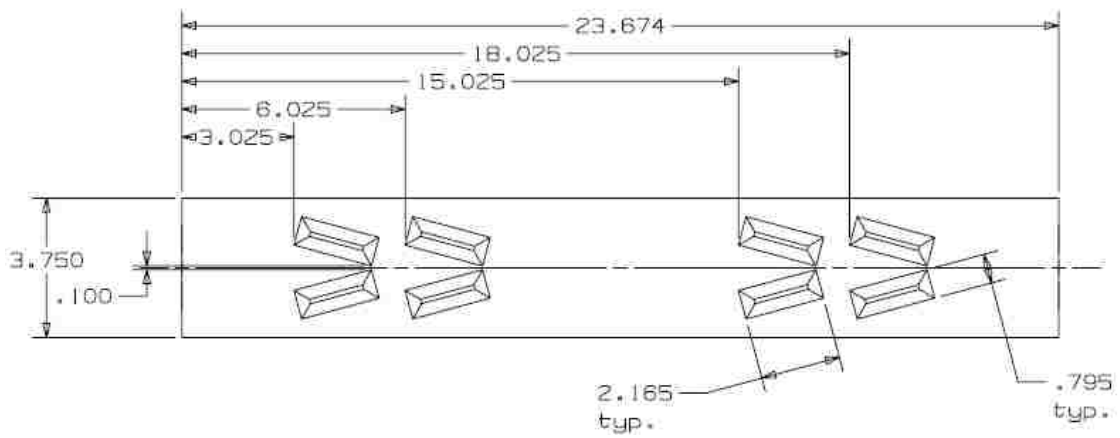


Figure 3.36: SFC021 side geometry, for the outlet portion of the duct.

4. EXPERIMENTAL PROCEDURE

This section describes the procedure for conducting the experiments once the test sections are manufactured, assembled, installed, and insulated. The procedure for manufacture, assembly, installation, and insulation of the test sections was described in Section 3. Again, the two sets of experiments were described separately, with Section 4.1 describing the experiments involving water, and Section 4.2 describing the experiments involving air.

4.1. LIQUID LOOP EXPERIMENTS

The steps for operation of the liquid loop were as follows:

1. *Prepared Loop:* Before filling the loop, it was important to ensure that the drain valve at the bottom of the loop was closed and that the each bleed valve on the settling chambers as well as the bleed valve in the upper corner were open, so that water could freely flow into the loop without compressing the air in the loop. Also, the pressure equalization valve on the pressure manifold was open so that the filling of the loop did not over pressurize the sensitive pressure transducer.
2. *Filled Loop:* Once the loop was prepared, it was filled with building supply water by opening the needle valve. As the loop filled, water would begin to flow out of the bleed valves in sequence, from the closest to the furthest from the filling point. As the water began to flow out of each bleed valve, it was closed and the loop continued filling, until water was flowing out of the top most bleed valve. It was not immediately closed, as doing so would begin to pressurize the loop. Instead, the supply water was turned off. The bleed valve was left open for the next step: bleeding of the pressure transducer manifold.

- Bled the pressure transducer manifold:* Once the loop was full of water, it was necessary to bleed the pressure transducer manifold to remove all air. Even a small amount of air in the loop or the manifold could cause large discrepancies in pressure readings.

The pressure transducer manifold was bled using an over-head five gallon bucket filled with water, which was plumbed into the pressure transducer manifold. A valve was opened which allowed water to flow via gravity from the bucket into the loop through the manifold. Thus, each part of the manifold was bled by opening valves in turn so that the bubbles could escape either out the bleed valves in the manifold, or back into the loop. As water was released from the bucket into the loop the excess water would spill out of the main bleed valve.

The reason for using the bucket instead of loop pressure for bleeding was to reduce the chance of over pressurizing the pressure transducer. Once all air was bled from the manifold, the transducer itself was bled by slowly loosening the bleed screws in turn until they were both opened. Once all air was out of the line from the manifold to the transducer, the bleed screws were closed.

Once the manifold was bled, the valve to the bucket was closed and the building water needle valve turned on to allow a slow flow of water into the loop. The loop was again bled to remove any air that had entered during the manifold bleeding process. The loop water was also circulated by turning on the pump to ensure all bubbles had been worked loose, and each bleed valve was again opened in turn to ensure all air was allowed to escape.

- Pressurized loop:* Once the loop was satisfactorily bled, it was pressurized to 10 psi. It was necessary to run the loop under pressure to prevent cavitation at the pump inlet, as well as to prevent dissolved gases from being released from solution as the water heated up.

Once the loop was pressurized and bled, it was ready to run. Pressure measurements were taken first, then temperature measurements were taken, as described in the following two subsections:

4.1.1. Pressure Drop Measurements. All pressure drop measurements were conducted at room temperature, as follows:

1. *Adjusted flow rate:* The pump was turned on and the flow rate adjusted using the flow rate needle valve until the desired flow rate was attained. If the flow rate was particularly low, it was necessary to open the recirculation gate valve to reduce power requirements on the pump and to stabilize the flow rate.
2. *Selected pressure taps:* Valves on the pressure transducer manifold were used to select the pressure taps across which to measure the pressure drop.
3. *Collected data:* Data was collected for thirty seconds at a rate of 1000 Hz and stored in a file using LabView.
4. *Repeat:* The above procedure was repeated until all desired pressure drop data at all desired operating points had been collected.

4.1.2. Temperature Measurements. Once the pressure measurements were taken, the temperature measurements were taken according to the following procedure:

1. *Turned on data monitoring system:* The data monitoring system was turned on so that the critical system variables could be monitored. The values monitored by the data monitoring system were mass flow rate, pressure drop, heater wattages, and various fluid and wall temperatures throughout the loop.
2. *Adjusted flow rate:* The pump was then turned on and the flow rate adjusted using the flow rate needle valve until the desired flow rate was attained. If the flow rate

was particularly low, it was necessary to open the recirculation gate valve to reduce power requirements on the pump and to stabilize the flow rate.

3. *Turned on test section heaters:* The test section heaters were then turned on and adjusted to the desired power. The auxiliary heater could also be turned on at this point to speed up loop heating. Once the loop neared steady state operating temperature, the auxiliary heater was turned off.
4. *Monitored loop:* The loop was monitored as it heated up, and water was bled off as necessary to avoid over pressurizing the loop.
5. *Turned on cooling water:* Once the loop reached the desired operating temperature, the cooling water was turned on and the flow rate adjusted to maintain the loop temperature. The loop was then allowed to find a steady state.
6. *Collected data:* Once the loop reached a steady-state, the data was collected for thirty seconds and saved in a file, ready for data reduction.
7. *Repeat:* Once the data has been taken, the flow rate, wattage, and cooling water rate were changed, and a new steady state was found, data taken, and this process was repeated until data had been taken for all desired flow conditions.

4.2. EXPERIMENTS INVOLVING AIR

The steps for operation of the air loop are as follows:

1. *Set flow rate:* The flow rate was set by turning on the bower and opening the gate valve until the correct pressure difference across the orifice flow meter was measured.
2. *Set heater wattage:* The heater wattages were then adjusted until they were at the proper output level.

3. *Monitored loop:* The loop was then monitored, and allowed to reach steady state.
4. *Collected data:* Once the loop reached steady-state, the temperature and wattage data were collected for thirty seconds and saved to a file. The various pressure drop data were then taken by manually adjusting the manometer manifold valves to select the desired points and manually reading and recording the manometer. Each reading was taken either two or four times. The room air temperature and relative humidity were then measured and recorded. Finally, a voltage reading was taken from the barometer.

5. DATA REDUCTION

All experimental data were either measured and recorded by hand, or were recorded using a custom LabView program. The program took samples at a rate of 1000 Hz, and samples were recorded for at least 30 seconds once the experiment had come to steady state, giving a total of at least 30,000 samples. The data were stored in columns in a text file, and each column was averaged for use in the data reduction process. The purpose of taking so many samples was to mitigate any effect of random noise in the data.

5.1. DIRECTLY MEASURED QUANTITIES

This section discusses those properties which were directly measured by the instrumentation.

5.1.1. Temperature. Thermocouple data was recorded as a voltage created by the difference in temperature at the two ends of each thermocouple. For each block of thermocouples, an ice bath was used. The ice bath voltage was subtracted from the thermocouple voltage, giving a voltage difference representing the difference between the thermocouple temperature and that of the ice bath, designated as ΔV_T , in microvolts. A polynomial given by Nanmac Corp. [2006] was then used to convert the voltage difference to temperature, given as Equation 5.1.

$$\begin{aligned}
 T = & \\
 & 2.5928 \times 10^{-2} \Delta V_T - 7.602961 \times 10^{-7} \Delta V_T^2 + \\
 & 4.637791 \times 10^{-11} \Delta V_T^3 - 2.165394 \times 10^{-15} \Delta V_T^4 + \\
 & 6.048144 \times 10^{-20} \Delta V_T^5 - 7.293422 \times 10^{-25} \Delta V_T^6
 \end{aligned} \tag{5.1}$$

Where T is the temperature in degrees Celsius.

The bulk inlet and outlet temperature values were taken as the average of all thermocouples in the respective settling chambers. The bulk temperature of the fluid in the channel was taken as a linear variation due to the uniform imposed heat flux. For property determination, the temperature used was the average of the two settling chamber temperatures.

5.1.2. Mass Flow Rate. Since mass flow rate was measured differently for each of the flow loops, they will be discussed separately in the subsections following:

5.1.2.1. Liquid Loop. As mentioned previously, the mass flow rate in the liquid loop was directly measured using a coriolis flow meter. During the data acquisition, the voltage reading was sampled as a column in the previously mentioned data file and averaged. The mass flow meter did output a voltage which was linearly proportional to the observed mass flow rate. The conversion from voltage to mass flow rate was given by Equation 5.2

$$\dot{m} = 0.06763V_{FM} - 0.1253 \quad (5.2)$$

where \dot{m} was the mass flow rate in kg/s and V_{FM} was the flow meter voltage reading.

5.1.2.2. Air Loop. The air loop mass flow rate was calculated using the volumetric flow rate given by the orifice plate flow meter. The pressure drop across the orifice plate was converted to volumetric flow rate using an equation given by Miller [1996] and presented here as Equation 5.3

$$\dot{V} = F_{EL}F_{EM}N_{vp} \frac{C_D d^2}{\sqrt{1 - (d/D)^4}} \frac{Y_1}{\sqrt{\rho_{f1}}} \sqrt{h_w} \quad (5.3)$$

where F_{EL} was an elevation correction factor, F_{EM} was a manometer correction factor, N_{vp} was a units conversion factor, C_D was the discharge coefficient for the quadrant orifice plate, d was the orifice bore diameter, D was the duct inside diameter, Y_1 was the gas expansion

factor, ρ_{f1} was the density at the high pressure tap of the orifice plate, and h_w was the measured differential pressure across the orifice plate.

Once \dot{V} was known, then \dot{m} , the mass flow rate, was calculated by multiplying \dot{V} by the air density, ρ_{f1} .

5.1.3. Differential Pressure. Differential pressure was also measured differently for each of the flow loops. The next two subsections discuss each loop in turn.

5.1.3.1. Liquid Loop. The pressure transducer voltage readings, as recorded by the procedure in Section 4.1.1, were converted to pressure readings using Equation 5.4

$$\Delta P = 1.4 \times V \quad (5.4)$$

where ΔP was the pressure drop reading, in inches of water and V was the transducer voltage.

In addition to those pressure taps in the test sections, pressure taps were also installed in the bulk inlet and outlet settling chambers. These taps gave better results for the pressure drop across the enhanced surfaces, since they were not affected by local unsteadiness within the channel due to bumps. The settling chamber taps were, therefore, used in the pressure drop calculations, and the entrance and exit losses were subtracted out. The entrance and exit losses were calculated using Equation 5.5

$$\Delta P_{ts} = \Delta P_b - \xi \frac{1}{2} \rho U^2 \quad (5.5)$$

where ΔP_{ts} is the pressure drop across the test section, in N/m^2 , ΔP_b is the pressure drop across the settling chambers, also in N/m^2 , ξ is a non-dimensional head loss coefficient, and U is the mean fluid velocity, in m/s . The coefficient was calculated to be $\xi = 1.5$ by adding the known coefficients for a sudden contraction, 0.5, and sudden expansion, 1.0. The coefficient was verified using the plain channel test section. Figure 5.1 shows the

friction coefficient calculated using the measured pressure drop internally across the test section. Figure 5.2 shows the friction factor using the measured bulk pressure drop without losses subtracted, and finally Figure 5.3 shows the friction factor using the bulk pressure drop with losses subtracted.

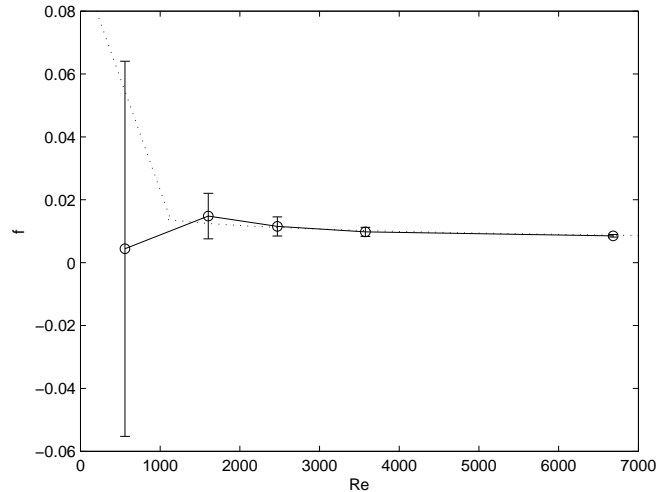


Figure 5.1: Friction factor as measured within channel.

The calculation of the friction factor is discussed in Section 5.2.1. The error bars indicate uncertainty due to the pressure transducer, discussed in Section 5.3.2.

5.1.3.2. Air Loop. The differential pressure between the various pressure taps was found by manually opening one valve each on the high and low side of the manifold to allow air flow between the desired points and the Dywer manometer, and manually observing and recording the reading. Each reading was repeated either two or four times, and an average was taken.

5.1.4. Heater Power. Heater power was converted directly from the voltage reading given by the watt transducers using Equation 5.6 for the liquid loop, and Equation 5.7

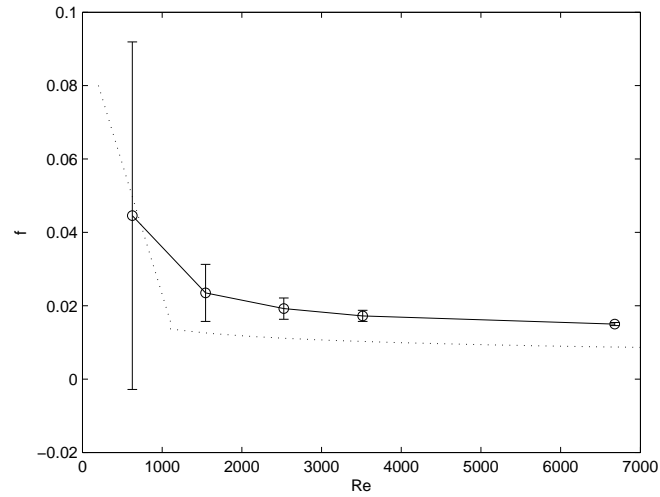


Figure 5.2: Friction factor as measured across settling chambers, no head losses removed.

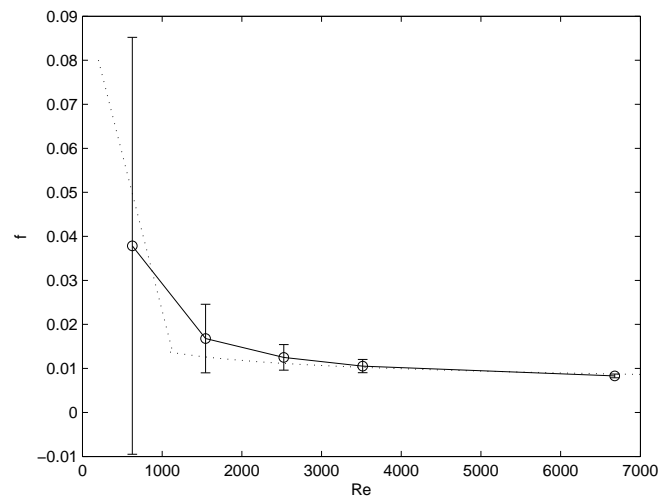


Figure 5.3: Friction factor as measured across settling chambers, head losses removed.

for the air loop where P was the power, in watts, and V was the watt transducer voltage reading.

$$P = 2400 \times V \quad (5.6)$$

$$P = 1200 \times V \quad (5.7)$$

5.2. CALCULATED QUANTITIES

Most of the quantities calculated were compared to the Reynolds Number based on hydraulic diameter, Re_{D_h} , as expressed in Equation 5.8 where D_h was the hydraulic diameter of the channel, μ was the viscosity of the fluid, ν was the kinematic viscosity of the fluid, and U was the mean fluid velocity. In the case of air, U was calculated by dividing the volumetric flow rate, \dot{V} , by the duct cross-sectional area, $W \times H$. In the case of water, U was calculated by dividing the mass flow rate, \dot{m} , by the density, ρ , and the duct cross-sectional area.

$$Re_{D_h} = \frac{\rho U D_h}{\mu} = \frac{U D_h}{\nu} \quad (5.8)$$

Hydraulic diameter was calculated using Equation 5.9 where A_x was the cross-sectional area, p was the perimeter, H was the channel height, and W was the channel width.

$$D_h = \frac{4A_x}{p} = \frac{2HW}{H+W} \quad (5.9)$$

5.2.1. Frictional Losses. The primary indicator used to compare frictional losses was the Fanning friction factor, f . The formula used to calculate the Fanning Friction Factor is given in Equation 5.10 where ΔP was the pressure drop between the two pressure taps and L was the distance between the taps.

$$f = \frac{\Delta P}{2\left(\frac{L}{D_h}\right)\rho U^2} \quad (5.10)$$

5.2.2. Heat Transfer. The primary indicator used to compare heat transfer was the length averaged Nusselt number based on hydraulic diameter, $\overline{\text{Nu}}_{D_h}$, defined as in Equation 5.11.

$$\overline{\text{Nu}}_{D_h} = \frac{1}{L} \int_0^L \text{Nu}(x) dx \quad (5.11)$$

In order to get the length averaged Nusselt number, a numerical integration was performed using the local Nusselt numbers at each thermocouple location. The local Nusselt numbers were each multiplied by the distance from half way to the previous thermocouple to half way to the next thermocouple, and the results summed. In the case of the first thermocouple, the distance was from the inlet to the point half way to the second thermocouple, and for the last thermocouple the distance was from the point half way to the next-to-last thermocouple and the exit. These products were then summed, and the total divided by the channel length to determine the length average Nusselt number.

In order to calculate the local Nusselt number, it is necessary to first calculate the local convective heat transfer coefficient, h . This was done via Equation 5.12 where T_{b_o} and T_{b_i} were the outlet and inlet bulk fluid temperatures, respectively, T_w was the wall temperature as measured by the thermocouple, and T_b was the local bulk fluid temperature, as calculated using an assumption of a linear change in fluid temperature across the channel, W was the channel width, and l was the channel length.

$$h = \frac{q_s''}{T_w - T_b} = \frac{\eta_{th} P}{2Wl(T_w - T_b)} = \frac{\dot{m}Cp(T_{b_o} - T_{b_i})}{2Wl(T_w - T_b)} \quad (5.12)$$

The local Nusselt number was then defined as Equation 5.13 where k was the convective heat transfer coefficient of water at the average bulk temperature.

$$\text{Nu}_{D_h} = \frac{hD_h}{k} \quad (5.13)$$

In order to compare heat transfer to frictional losses, the length averaged Colburn j factor was calculated using Equation 5.14 where Pr is the Prandtl number at the bulk average fluid temperature in the channel.

$$j = \frac{\overline{\text{Nu}}}{(\text{Re})(\text{Pr})^{\frac{1}{3}}} \quad (5.14)$$

5.2.3. Goodness Factor. Once the Colburn j factor and the Fanning friction factor were calculated, the goodness factor was calculated as j/f . This factor gives a good indication of the trade-off between heat transfer and frictional losses. A high goodness factor indicates relatively good heat transfer for the frictional penalty paid.

5.3. UNCERTAINTY ESTIMATION

5.3.1. Reynolds Number. The possible sources of uncertainty for the Reynolds number are the measurement of fluid velocity, determination of hydraulic diameter, and the determination of fluid density and viscosity. Of these, determination of fluid velocity is the most likely source of error. Some error may be introduced by not applying a viscosity correction factor due to the wall temperature, but the error involved is expected to be very small due to the relatively small temperature difference between the bulk fluid and the wall.

The accuracy of the liquid loop mass flow rate meter was very high at $\pm 0.0025\%$ of the reading, so there should have been very little error in fluid velocity determination there. The accuracy of the orifice plate on the air loop, however, was not as high, with an expected accuracy of approximately $\pm 2.5\%$ as observed by Rucker [2007]. Since Reynolds number

varies linearly with fluid velocity, it is expected that the accuracy of Reynolds number would be on the same order.

5.3.2. Friction Factor. The primary source of error for the calculation of friction factor was the measurement of the pressure drop across each channel. For the experiments involving air, the pressure drop was measured using the Dwyer micrometer manometer earlier mentioned, which had an accuracy of ± 0.00025 in. w.g. and the convenience of not needing calibration. The manometer zero was checked before each set of readings and adjusted if necessary to ensure the greatest accuracy.

Due to the relatively high pressure of the liquid flow loop and the small pressure drop being measured, it was very difficult to get an accurate reading for the lower flow rates. The diaphragm-type pressure transducer was very sensitive to overpressure, and would need recalibration or could even be ruined if the pressure difference across the diaphragm became too high. Because of this, the transducer used had a larger range than what would have been ideal for the lowest flow rates. The ΔP at the lowest flow rates was on the order of 0.01 inches of water. The pressure transducer used had an accuracy of 0.25% of full scale, which was 14 inches of water, giving an overall accuracy of ± 0.0035 inches of water. It was attempted to use a diaphragm with a scale of 0 - 1.4 inches of water, but efforts to install and bleed the diaphragm without permanently damaging it were not successful.

Another source of error in the pressure transducer was a potential bias in the calibration. It was necessary to calibrate the sensor dry with a dead weight pressure tester, then introduce water into the chambers once installed in the loop. Even after very careful bleeding of the loop, manifolds, and pressure transducer, the zero would shift to a reading on the order of -0.03 inches of water, still within the tolerance of the transducer. For each run, the actual zero reading was recorded and added as a tare value to the reading taken. Since the origin of this zero shift was unknown, it was included as a possible bias error. Figure 5.4 shows a plot of friction factor of the WFC000, the plain flat tube, with error bars representing this potential bias error. Also on the same plot is the expected results

from Moody [1944]. It is clear that the error is substantial at lower Reynolds numbers, but diminishes at higher Reynolds numbers, and thus higher pressure drops.

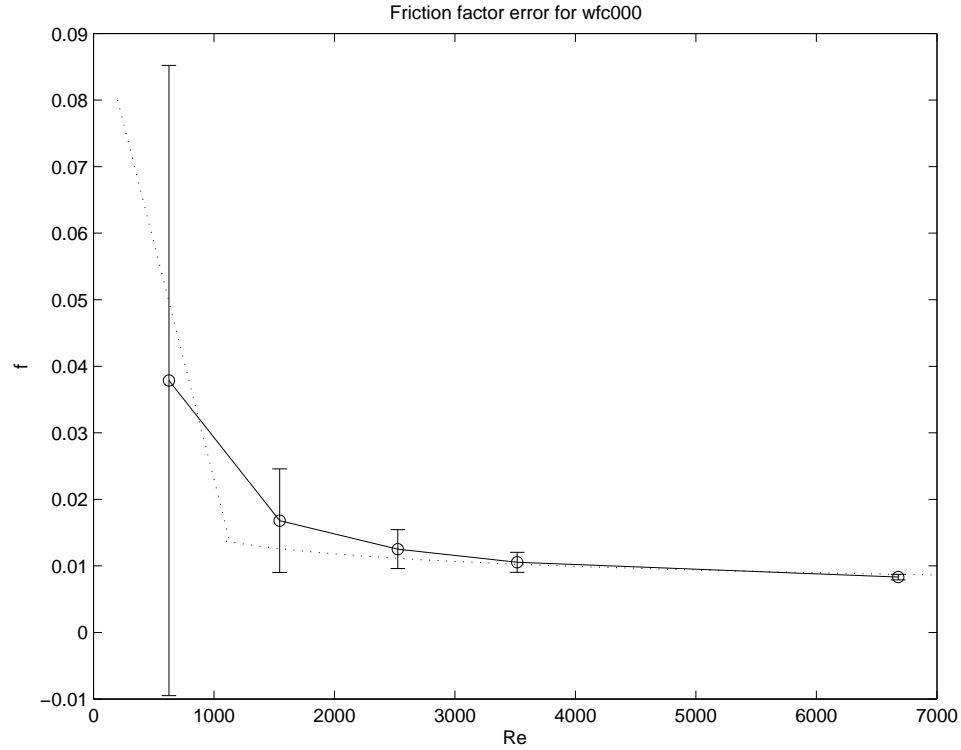


Figure 5.4: Friction factor error estimation.

5.3.3. Heat Transfer Results. The primary source of potential error in the heat transfer results was the assumption of an adiabatic wall boundary condition. Actual insulating efficiencies, as expressed by Equation 5.15 were between 96% and 99%. For each run, the efficiency was calculated and used in the convective heat transfer coefficient calculations. It is, therefore, expected that the heat transfer readings would generally be accurate to $\pm 5\%$.

$$\varepsilon = \frac{\dot{m}C_p(T_{b_o} - T_{b_i})}{P} \quad (5.15)$$

6. RESULTS AND DISCUSSION

6.1. LIQUID-LOOP TEST SECTIONS

6.1.1. Overall Results. The primary purpose of this study was to determine the effectiveness of each of the selected geometries in promoting overall heat transfer from a solid channel wall to the bulk fluid, while at the same time minimizing overall pressure drop. Figure 6.1 is a plot of the length averaged Nusselt number based on hydraulic diameter of each of the test sections. Also included is a correlation by Gnielinski [1976] and the Dittus-Boelter equation [Winterton, 1998] for comparison to the plain channel.

It would seem WFC010, the plain bump geometry, had the highest heat transfer in general, with WFC103, the rifling geometry, being a very close second. Next is WFC012, which was similar to WFC010 besides having a shorter bump height.

The overall heat transfer, however, is only one half of the picture. Figure 6.2 shows the length averaged Fanning friction factor for each of the test sections. Here, WFC010, which had the highest heat transfer coefficient, also had by far the highest friction coefficient. However, WFC103, which had nearly the same heat transfer performance as WFC012 had the lowest friction penalty of all of the enhanced geometries. We can also see that WFC012 had a substantially lower friction penalty than WFC010, though it was slightly higher than WFC103.

The friction factor results were also compared to equivalent sand grain roughness heights, k_s , using the Colebrook equation, shown in Equation 6.1, and tabulated, along with actual bump heights, in Table 6.1.

$$\frac{1}{\sqrt{4f}} = -2.0 \log_{10} \left(\frac{k_s/D_h}{3.7} + \frac{2.51}{Re\sqrt{4f}} \right) \quad (6.1)$$

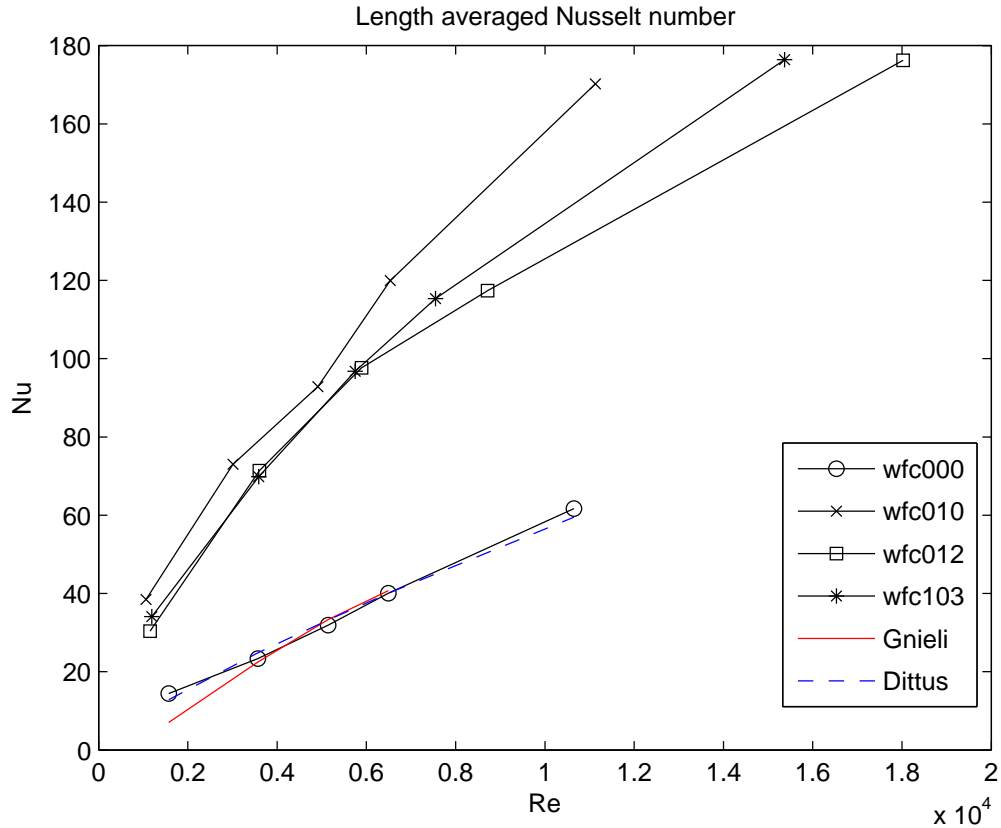


Figure 6.1: Length averaged Nusselt number.

The equivalent sand grain heights were then used to compute the roughness Reynolds number, Re_k , as calculated in Equation 6.2 and tabulated in Table 6.2.

$$Re_k = \frac{Re \sqrt{f/2}}{D_h/k_s} \quad (6.2)$$

Fully rough is defined as $Re_k > 70$. As Reynolds number decreases, only WFC010 remains fully rough, with the rest lying in the transitionally rough regime. This would account for the higher Nusselt numbers and friction coefficients of the WFC010 geometry, particularly at lower Re .

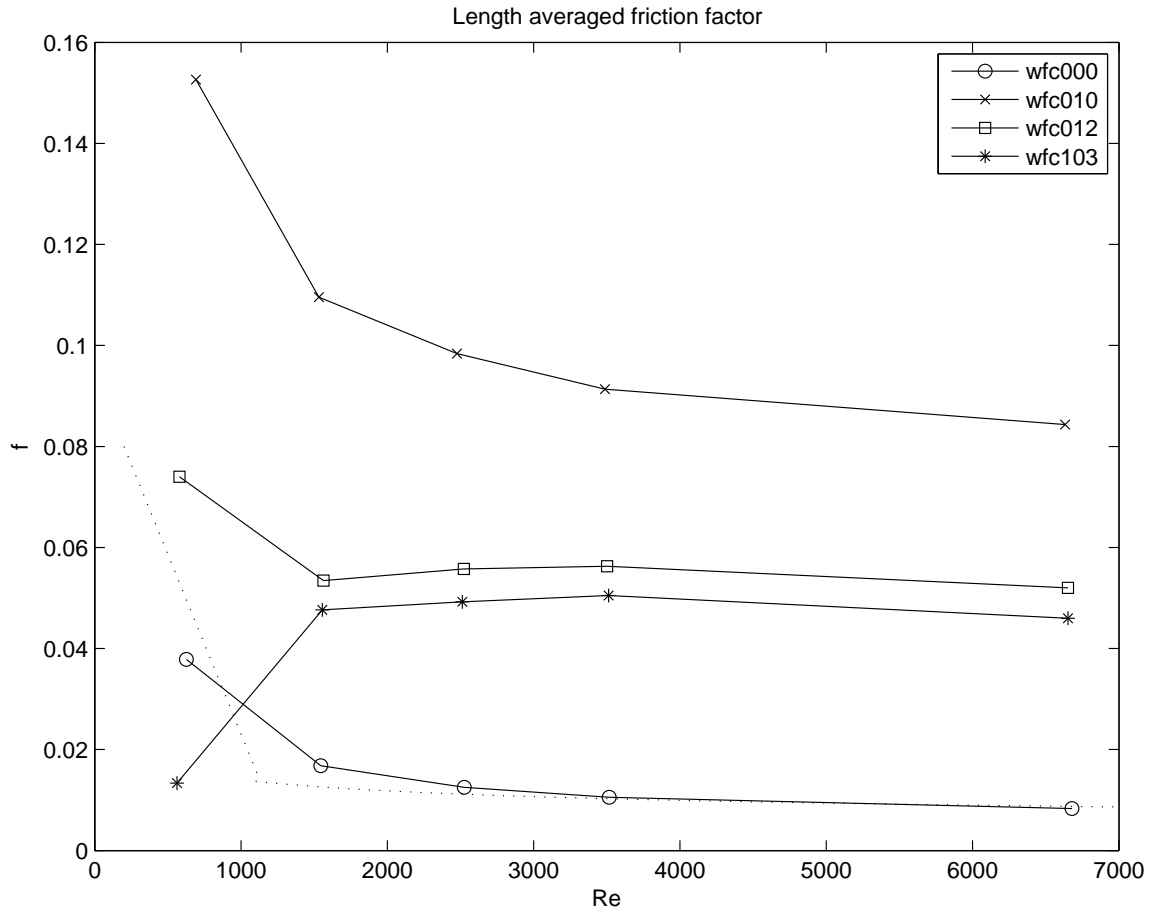


Figure 6.2: Length averaged Fanning friction factor.

Figure 6.3 presents the calculated Colburn j -factor, j , which was used to compare the heat transfer and friction results directly. A goodness factor, calculated as j/f was calculated and the results are presented as Figure 6.4. Note that, while WFC010 had the highest heat transfer coefficient, it also had the lowest goodness factor of all of the enhanced geometries. Also, of all of the enhanced geometries, WFC103 clearly had the highest goodness factor. Note that while the plain channel, WFC000, would seem to be a good choice based on goodness factor alone, the very low heat transfer provided would require a very large heat transfer surface if it were chosen. Conversely, though the WFC010 geometry

Table 6.1: Equivalent pipe sand grain roughness heights, in inches.

Re	WFC000	WFC010	WFC012	WFC103
615	0.0240	0.2132	0.0838	-0.0003
1549	0.0025	0.1479	0.0505	0.0409
2509	0.0008	0.1297	0.0549	0.0439
3505	0.0004	0.1178	0.0561	0.0462
6654	0.0001	0.1058	0.0491	0.0390
Actual bump heights:				
	0.000	0.168	0.120	0.075

Table 6.2: Roughness Reynolds number, R_k , values.

Re	WFC000	WFC010	WFC012	WFC103
615	4.3623	86.0478	19.7373	-0.0270
1549	0.7619	111.9536	27.2588	20.7085
2509	0.3484	150.3384	48.8584	36.5252
3505	0.2023	185.3158	69.6080	54.4314
6654	0.1026	304.2074	111.0761	83.1062

had the lowest goodness factor, it may still be a desirable option if one desired to build a heat exchanger of the smallest size possible, and if power requirements were of little consequence. Also note that the plain channel's perceived high goodness factor falls off at lower Reynold's numbers. Since the purpose of surface enhancements is to destabilize the flow and make transition happen at a lower Re, it is hypothesized that at lower, more laminar, Reynolds numbers, the enhanced geometries would all have higher goodness factors than the plain channel.

6.1.2. Local Observations. The temperature data obtained was of a fine enough resolution that some local observations were able to be made. Plots showing wall temperature and local Nusselt number variations plotted against channel position for the liquid experiments are presented in the Appendix.

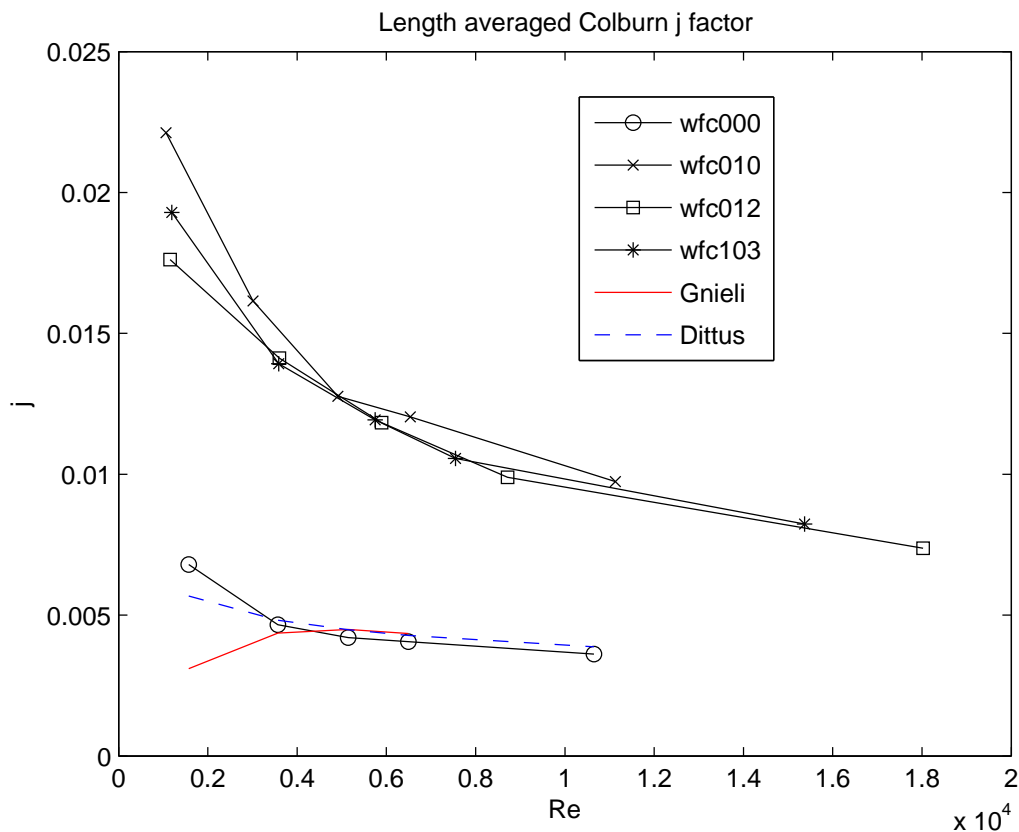


Figure 6.3: Length averaged Colburn j factor.

The plain tube had a wall temperature distribution which increased more rapidly in the channel inlet, and became more linear as it approached the midpoint and remained mostly linear to the outlet. As one might expect, the local Nusselt number was also highest toward the entrance, and decreased and finally leveled off toward the outlet. The phenomenon was more dramatic for the higher Reynolds number flows. It is hypothesized that increased turbulence in the entrance was a contributing factor. An example plot of wall temperature and Nusselt number variations are presented as Figures 6.5 and 6.6.

The bumped geometries, WFC010 and WFC012, had temperature distributions which were much closer to being linear across their length. They did, however, show a

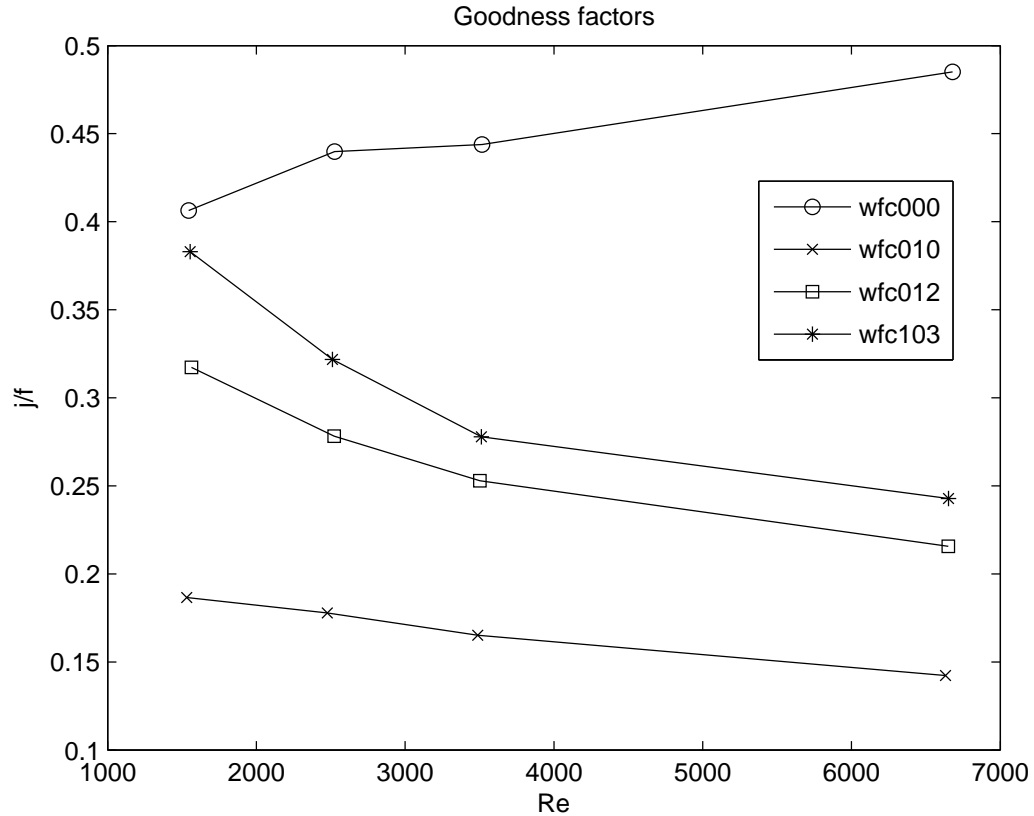


Figure 6.4: Goodness factor comparison.

wavy, almost periodic distribution. The distribution was further studied to try to determine the cause for the waviness. It was hypothesized that the waviness was actually showing variations in temperature at various locations on each individual bump, and that the variations were aliased such that a larger periodic distribution was observed. Figure 6.7 shows the temperature distribution along with a linear regression of the data and the channel wall geometry. A vertical line is drawn at the center of each bump. It was observed that the majority of the points lying above the linear regression are just behind a bump centerline, while the majority of those below the regression are just in front of the bump centerline. It was hypothesized, therefore, that the majority of the cooling is done at the leading edge of

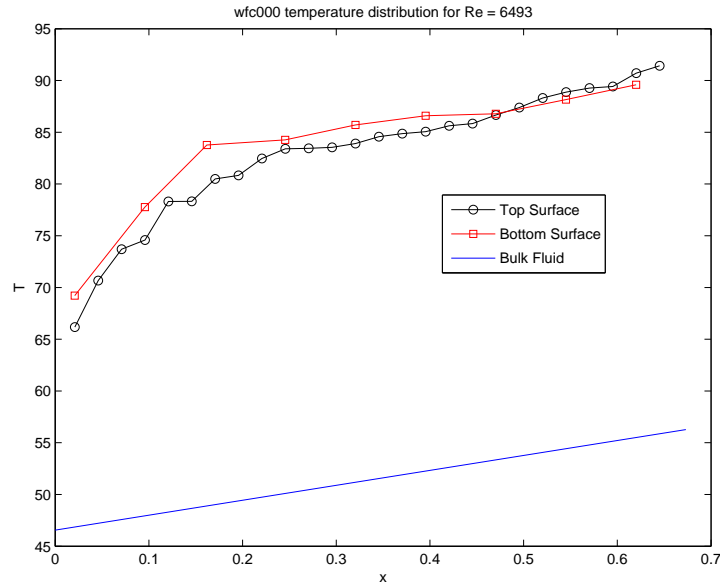


Figure 6.5: Wall and bulk fluid variation for WFC000 at $Re = 6493$.

the bump. This result is intuitive if we consider that the fluid begins to develop a boundary layer as when it hits the bump. Heat transfer is best when the boundary layer is smallest. As the fluid flows over the bump toward the back, the boundary layer grows and the fluid nearest the wall is heated and is thus less effective at cooling the wall by the time it reaches the bump trailing edge.

Test section WFC103, the rifling geometry, showed the most linear temperature distribution of all of the enhanced geometries. An example wall distribution is shown in Figure 16, suggesting an even fluid heating throughout the length. Due to the highly three-dimensional nature of the WFC103 geometry, it would be difficult to make any local observations with a one-dimensional approach as was done in this study.

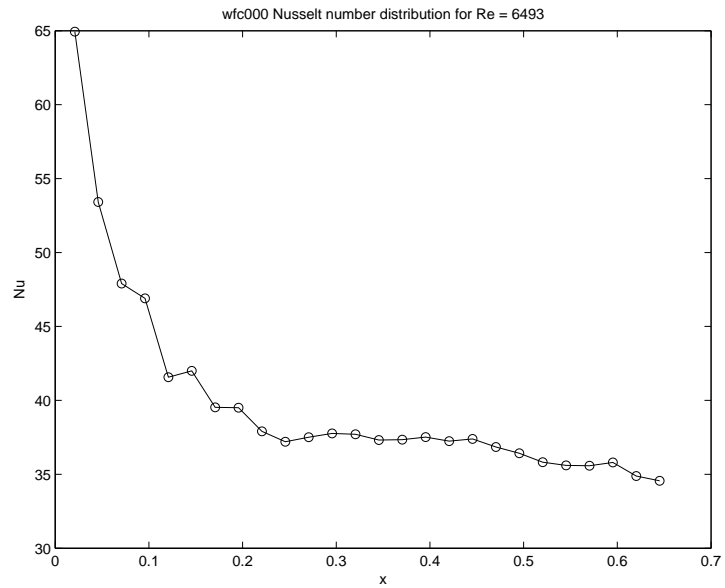


Figure 6.6: Nusselt number variation for WFC000 at Re = 6493.

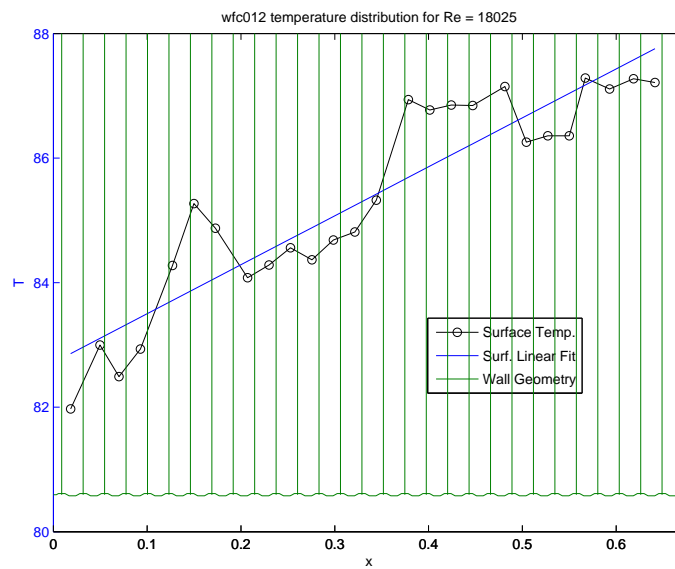


Figure 6.7: Wall temperature variation for WFC012 at Re=18025.

6.2. AIR LOOP TEST SECTIONS

Figure 6.9 is a plot of the length averaged Nusselt number based on hydraulic diameter of each of the test sections studied, including test sections done by Rucker [2007]

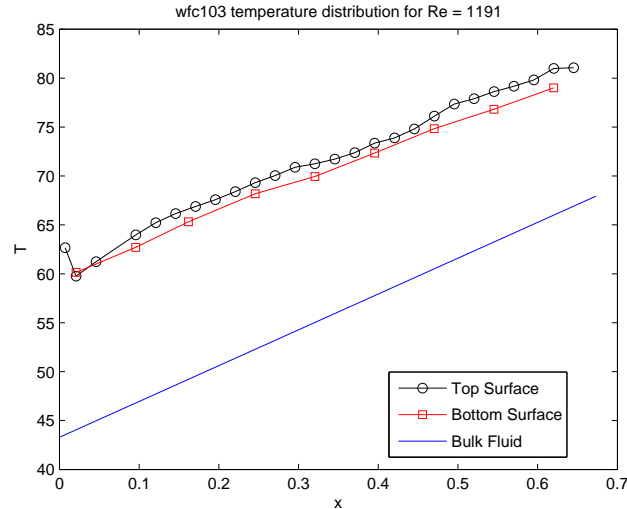


Figure 6.8: Wall temperature variation for WFC103 at Re=1191.

for comparison, as denoted by ‘sjr’ replacing ‘sfc’ in the legend. The LVG geometries, SFC020 and SFC021, are similar, both being somewhat lower than the plain bumped geometries at higher Reynolds numbers, but doing better at lower Reynolds numbers. The Nusselt numbers for the higher Reynolds numbers are consistent with those found in the liquid tests for similar geometries.

Figure 6.10 shows the length averaged Fanning friction factor for each of the test sections. SFC020 and SFC021 again have similar heat frictional losses, with considerably lower friction factors than the plain bump test sections previously studied. The SFC021 geometry was also similar in design to the SFC020, both having LVG patches. The SFC021 geometry’s LVG’s were longer, and at a shallower angle of attack to the fluid flow.

Figure 6.11 presents the calculated Colburn j -factor, j . A goodness factor, calculated as j/f was calculated and the results are presented as Figure 6.12. The SFC020 and SFC021 again gave similar results, each doing substantially better than the previous geometries. SFC020 did better at lower Reynolds numbers, while SFC021 did better at higher

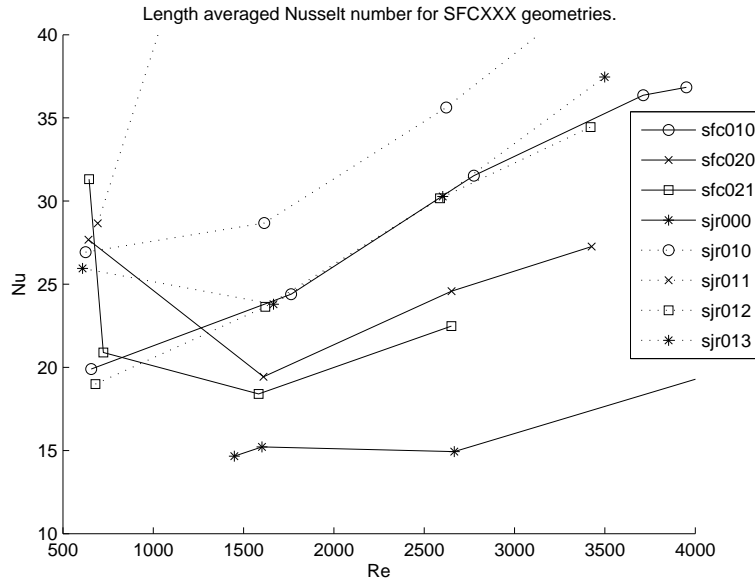


Figure 6.9: Length averaged Nusselt number.

Reynolds numbers. This is intuitive due to the sharper angle of attack of the SFC020 geometries, which would tend to cause transition earlier. While the longer, shallower LVG's of the SFC021 geometries would cause less flow mixing, they would also have less of an effect on pressure drop.

Due to the large mass of aluminum in the walls of the SFCXXX geometries and the relatively low convective heat transfer of the air on the walls, there was a significant amount of conduction within the walls. This conduction acted to spread out the temperature profile along the length, making any local effects impossible to distinguish.

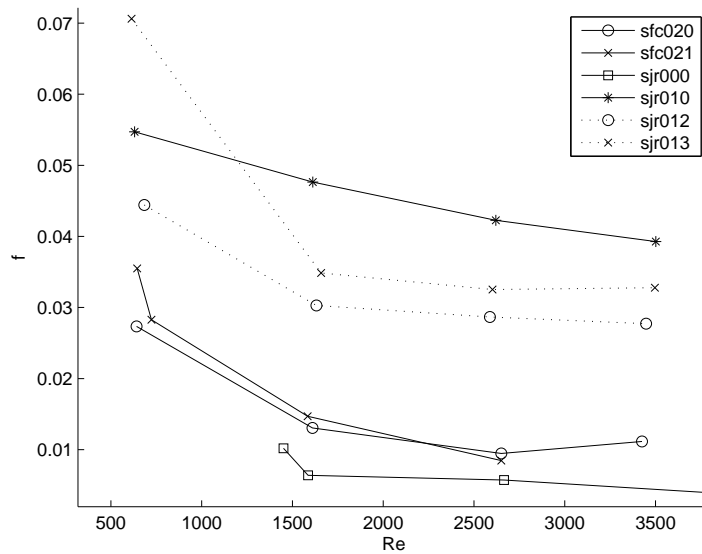


Figure 6.10: Length averaged Fanning friction factor.

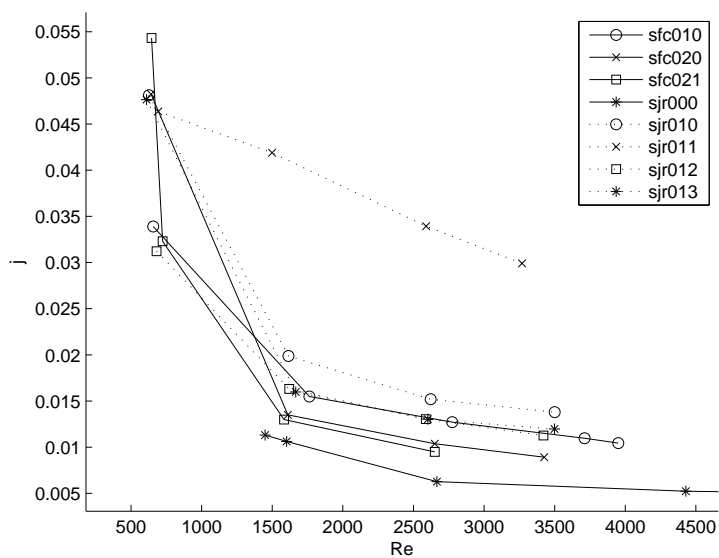


Figure 6.11: Length averaged Colburn j factor.

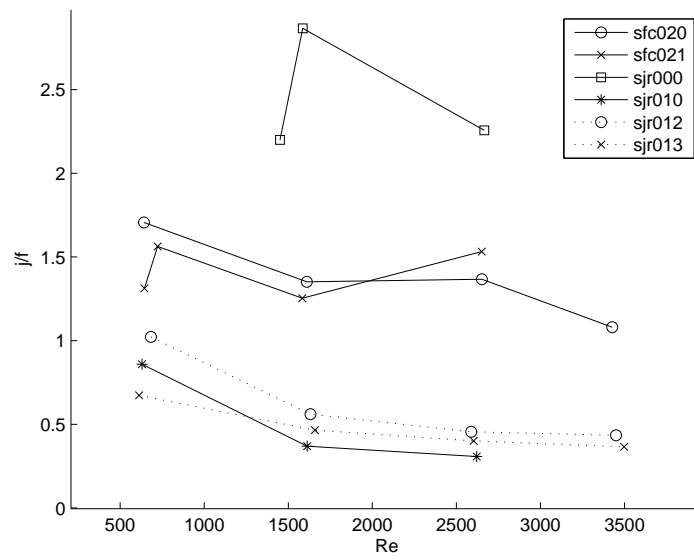


Figure 6.12: Goodness factor comparison.

7. CONCLUSIONS AND RECOMMENDATIONS

It was concluded that, while the plain bump geometry in the baseline bump (XFC010) channels have relatively high heat transfer coefficients, the frictional losses were observed to be too great to justify the higher heat transfer, except in the case of desiring to make a heat exchanger as small as possible while neglecting power requirements. Shortening the bumps, as in the XFC012 geometries does decrease heat transfer somewhat, but the decrease in frictional losses are of a greater magnitude, giving a better goodness factor overall.

Of all of the test sections studied, the XFC103 rifling geometry was the most intriguing. It was observed to have heat transfer coefficients better than the XFC012 geometries, while having the lowest frictional losses of all of the enhanced geometries studied. Employing the XFC103 geometries, therefore, would allow heat exchangers with sizes on the order of those having the XFC012 geometry, but requiring significantly less power to drive the flow.

The LVG geometries, XFC020 and XFC021, were also promising, giving relatively high heat transfer for a more modest pressure drop than the bumped geometries.

Further study into the rifling geometries would be recommended. Ideas for future research would be varying rifling bump angle of attack, height, width, and leading/trailing edge angles, as well as intermittent rifling along the channel. Since the exact dimensions chosen in this study were more or less educated guesses, it is certainly likely that better geometries exist. Future research could also include studies of the local and three dimensional phenomena at work in rifled channels. Visualization and numerical methods could be employed, as well as studies similar to this one, but with thermocouples strategically placed to capture local wall temperature variations.

As mentioned previously, studying the current geometries at lower Reynolds number with accurate pressure drop measurements would also add quality to the data.

APPENDIX

This appendix contains figures showing the wall temperature variations for each of the various experiments discussed in the preceding document. Also presented are the Nusselt number variations. Each figure's caption indicates the test section designation as well as the Reynolds number at which the test was run.

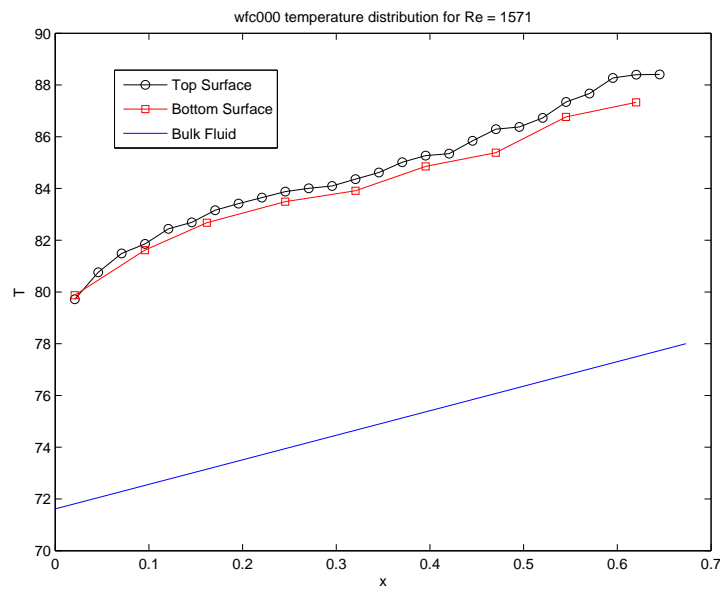


Figure 1: Wall and bulk fluid variation for wfc000 at Re = 1571.

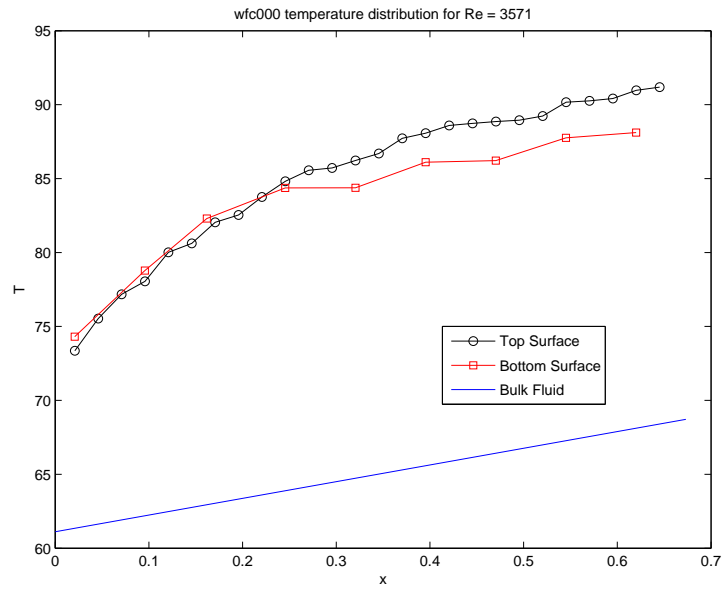


Figure 2: Wall and bulk fluid variation for wfc000 at Re = 3571.

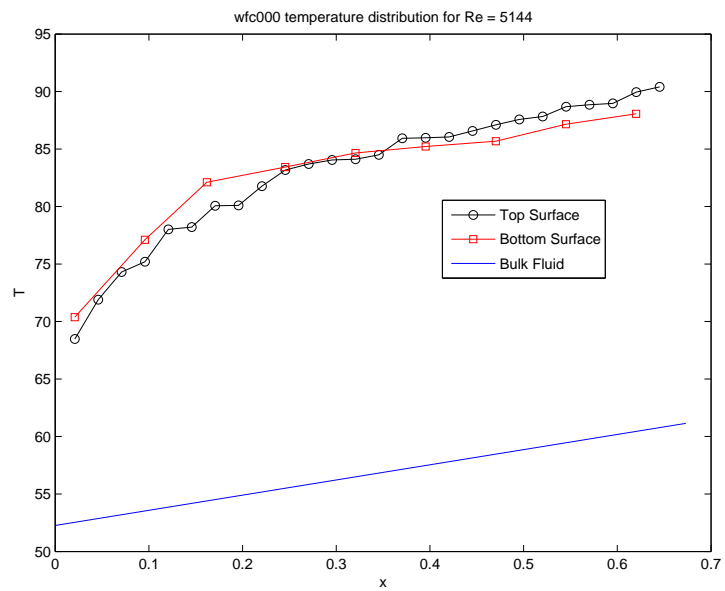


Figure 3: Wall and bulk fluid variation for wfc000 at Re = 5144.

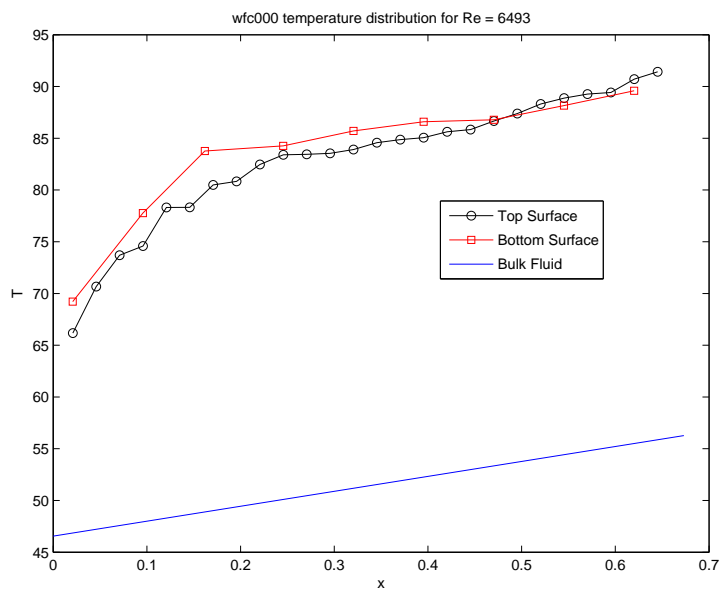


Figure 4: Wall and bulk fluid variation for wfc000 at Re = 6493.

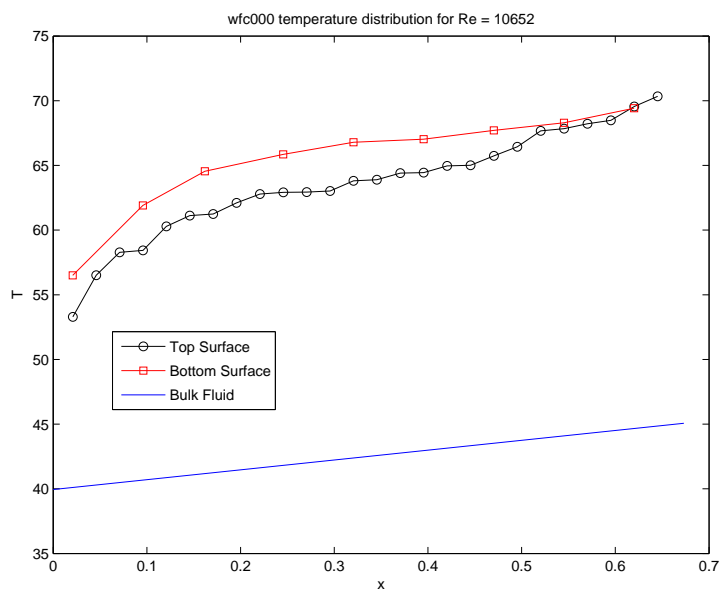


Figure 5: Wall and bulk fluid variation for wfc000 at Re = 10652.

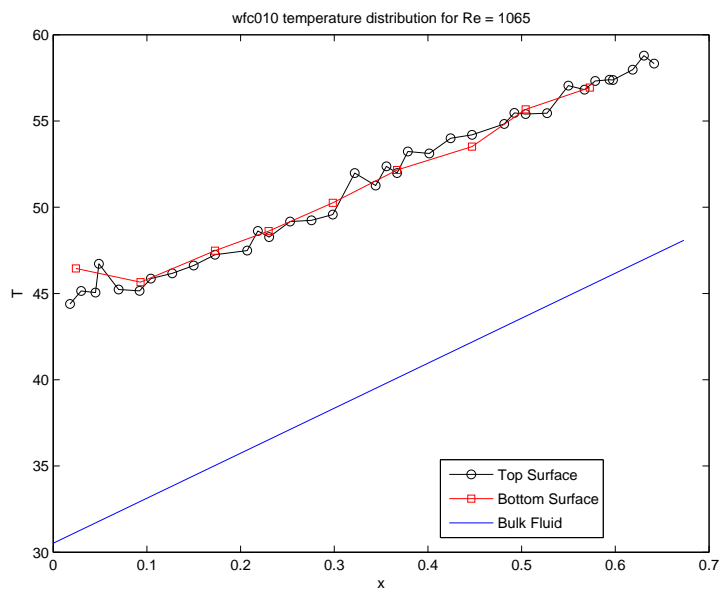


Figure 6: Wall and bulk fluid variation for wfc010 at Re = 1065.

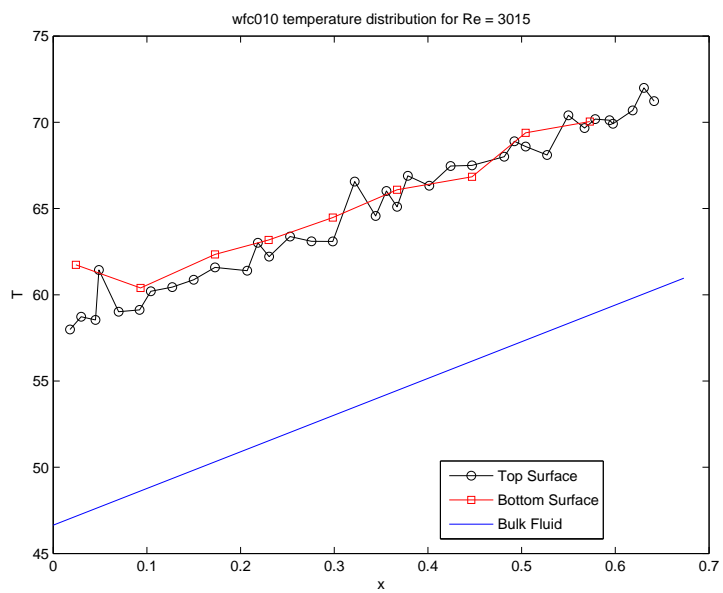


Figure 7: Wall and bulk fluid variation for wfc010 at Re = 3015.

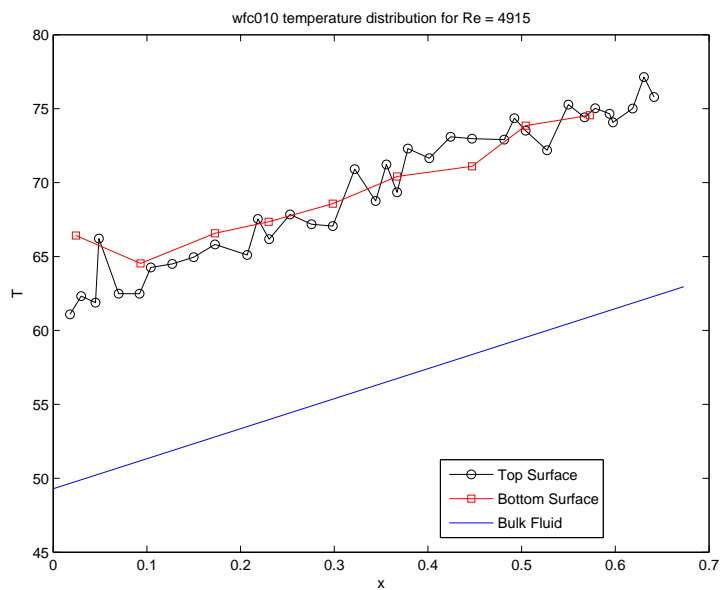


Figure 8: Wall and bulk fluid variation for wfc010 at Re = 4915.

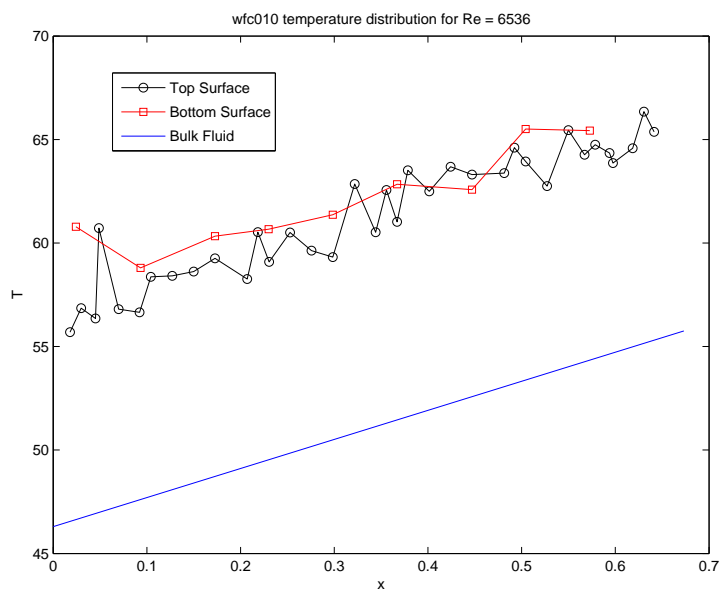


Figure 9: Wall and bulk fluid variation for wfc010 at Re = 6536.

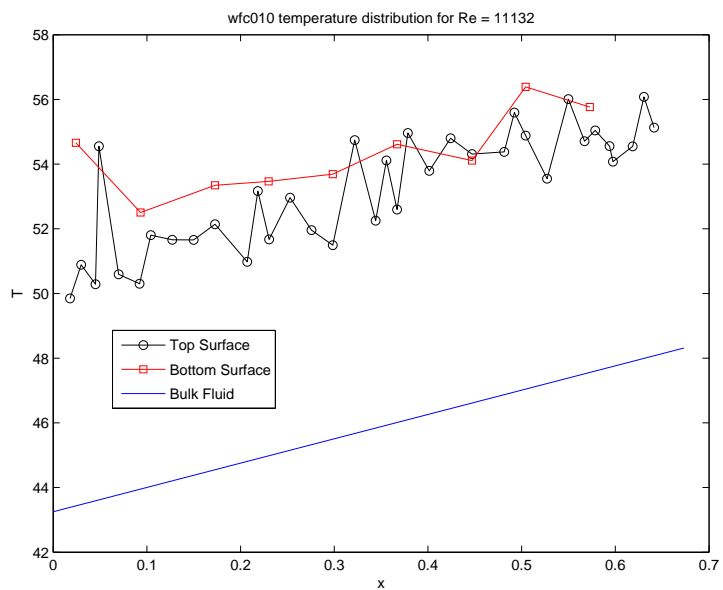


Figure 10: Wall and bulk fluid variation for wfc010 at Re = 11132.

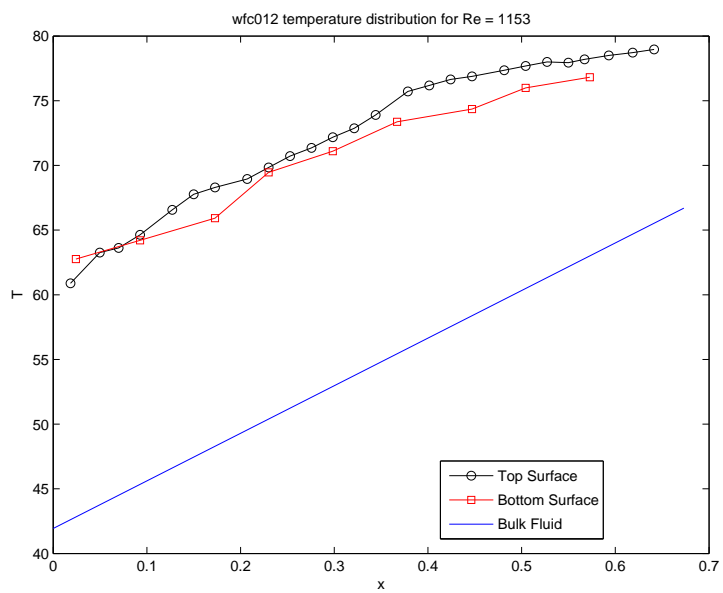


Figure 11: Wall and bulk fluid variation for wfc012 at Re = 1153.

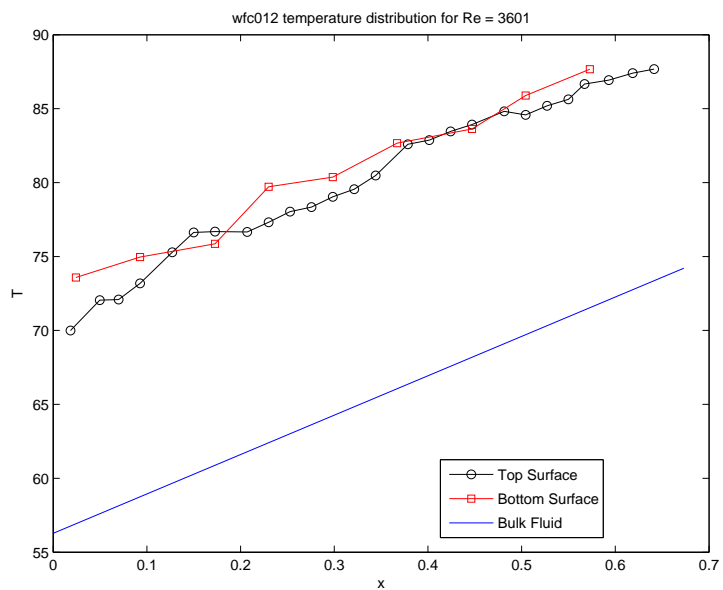


Figure 12: Wall and bulk fluid variation for wfc012 at Re = 3601.

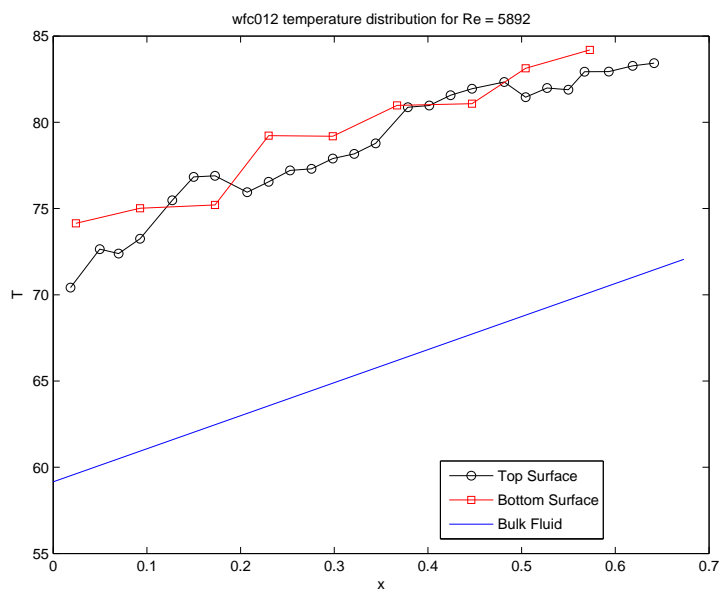


Figure 13: Wall and bulk fluid variation for wfc012 at Re = 5892.

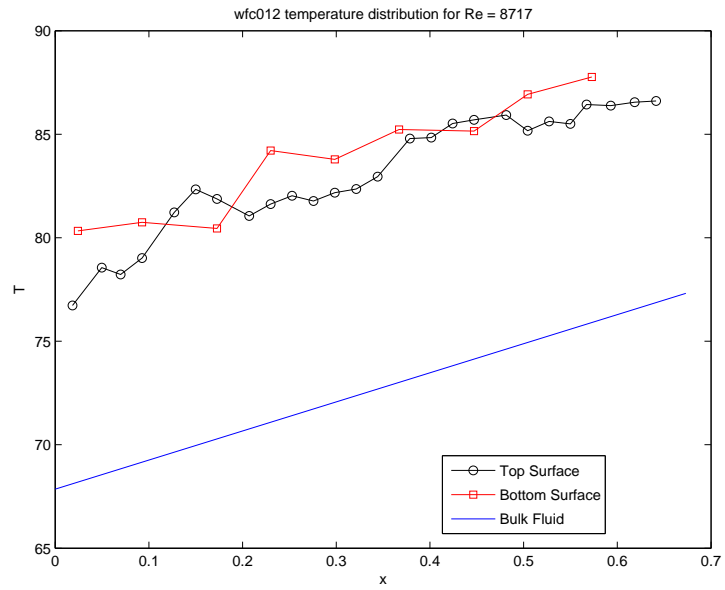


Figure 14: Wall and bulk fluid variation for wfc012 at Re = 8717.

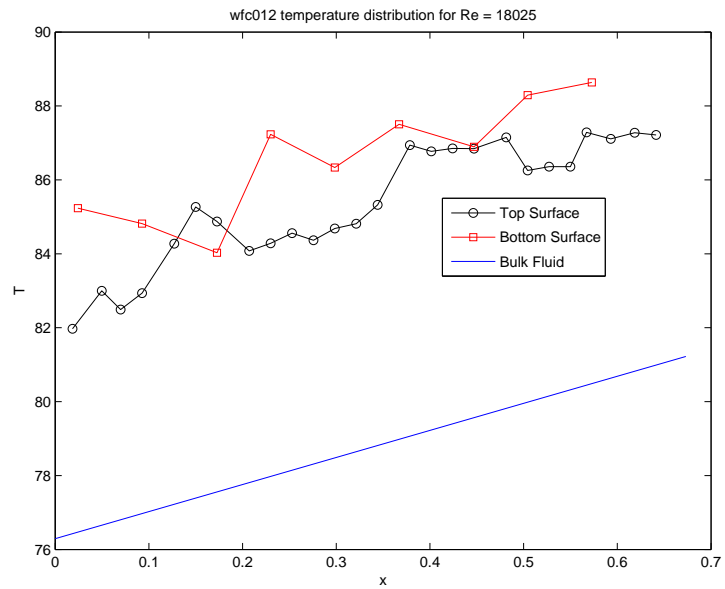


Figure 15: Wall and bulk fluid variation for wfc012 at Re = 18025.

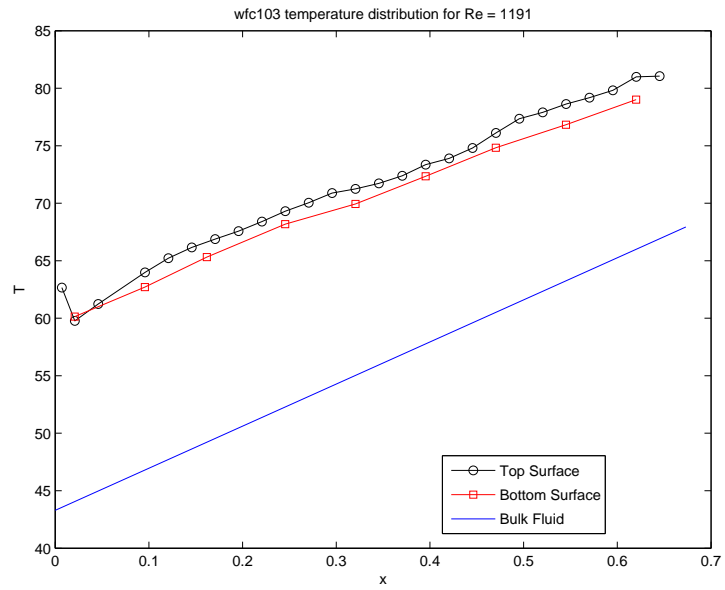


Figure 16: Wall and bulk fluid variation for wfc103 at Re = 1191.

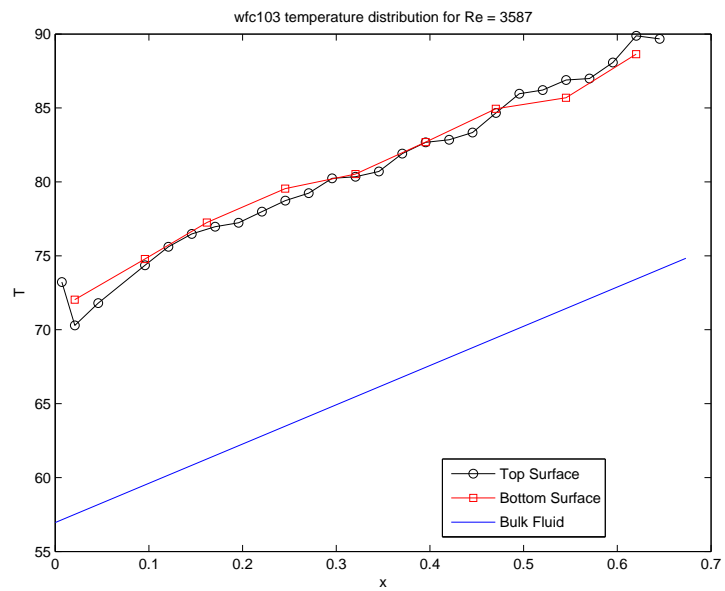


Figure 17: Wall and bulk fluid variation for wfc103 at Re = 3587.

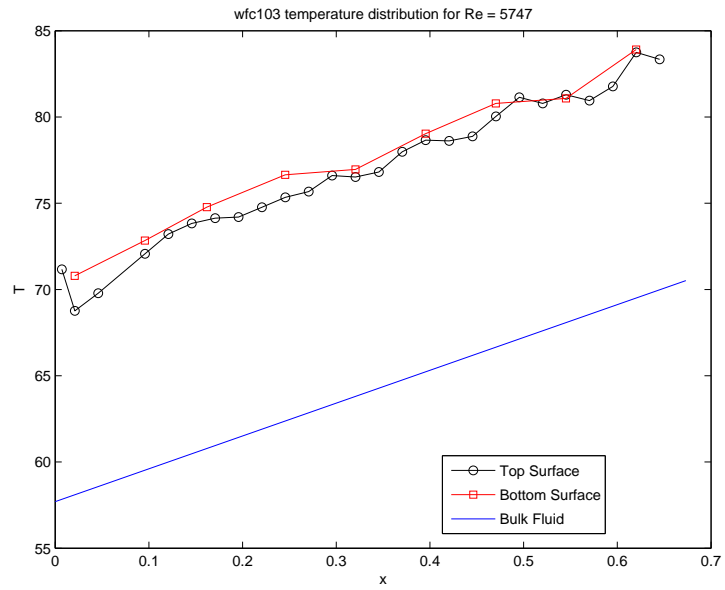


Figure 18: Wall and bulk fluid variation for wfc103 at Re = 5747.

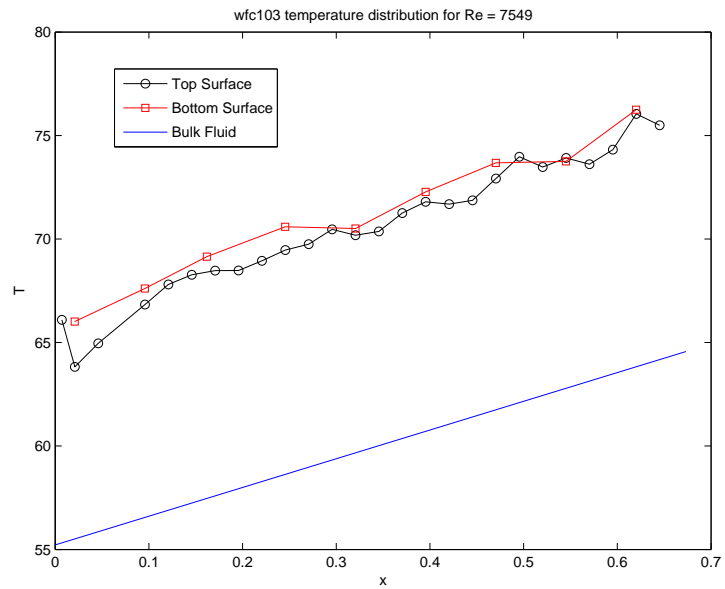


Figure 19: Wall and bulk fluid variation for wfc103 at Re = 7549.

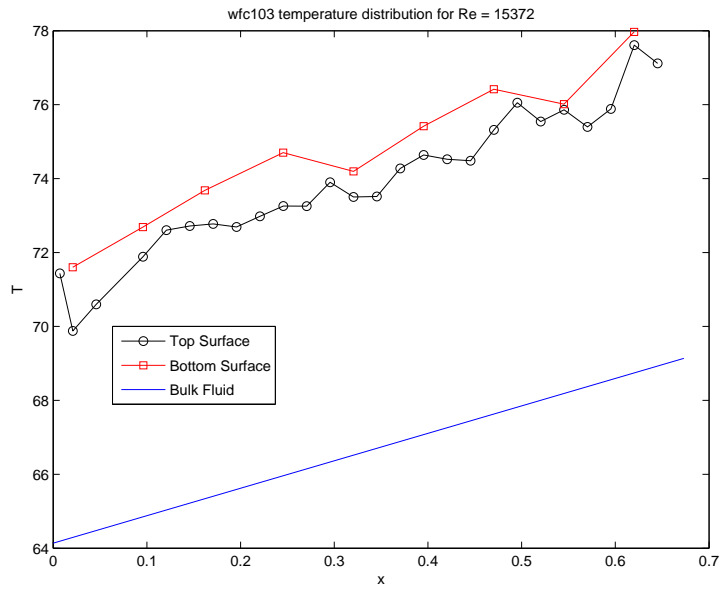


Figure 20: Wall and bulk fluid variation for wfc103 at Re = 15372.

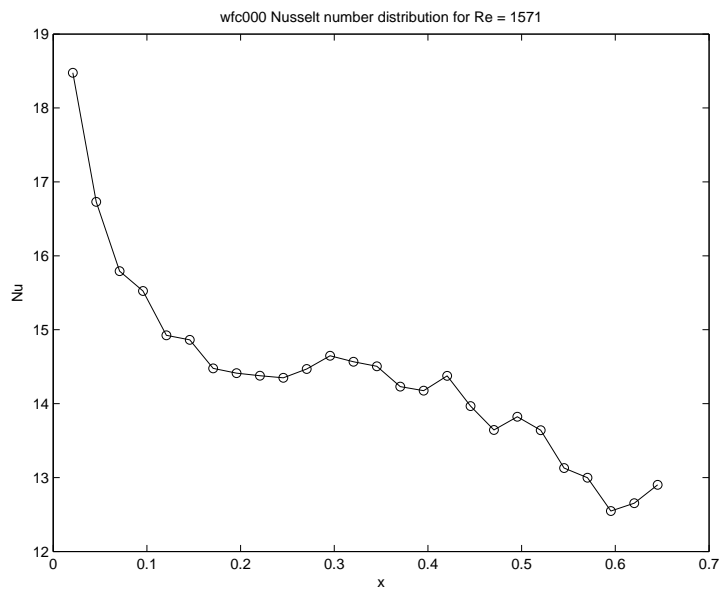


Figure 21: Nusselt number variation for wfc000 at Re = 1571.

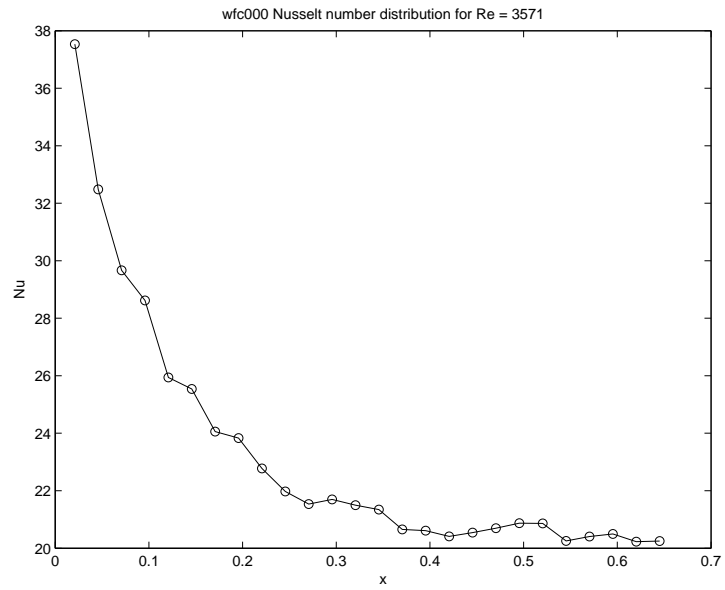


Figure 22: Nusselt number variation for wfc000 at Re = 3571.

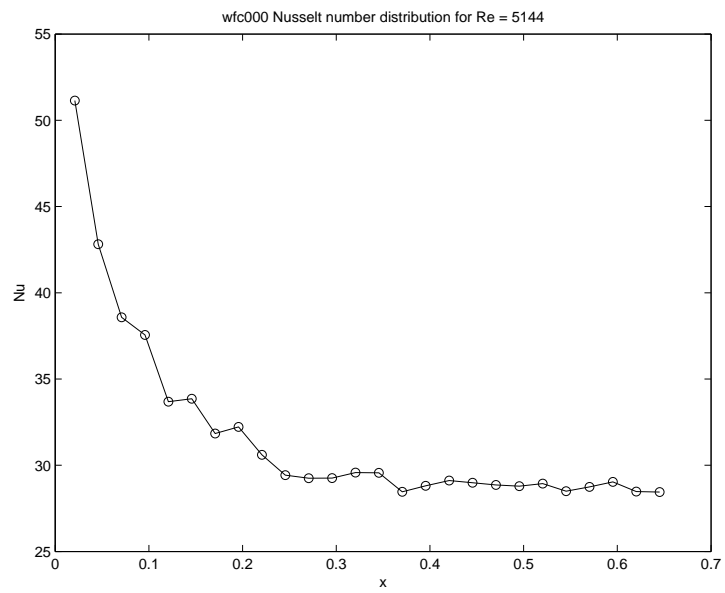


Figure 23: Nusselt number variation for wfc000 at Re = 5144.

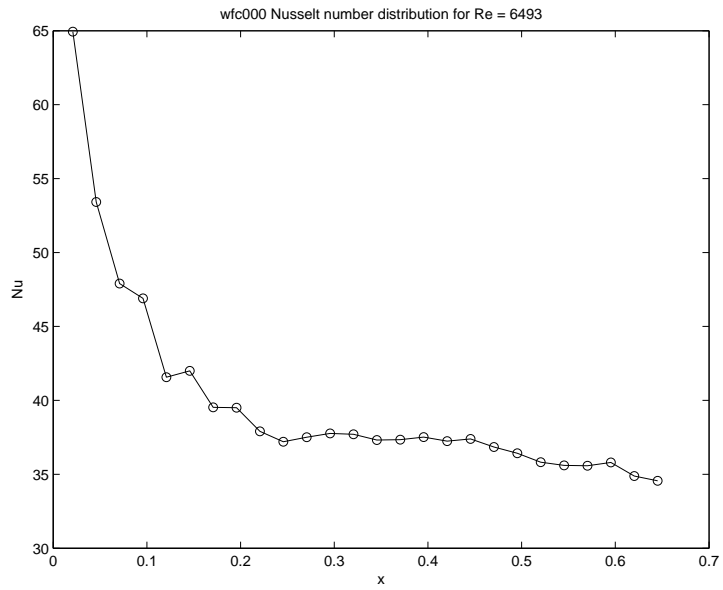


Figure 24: Nusselt number variation for wfc000 at Re = 6493.

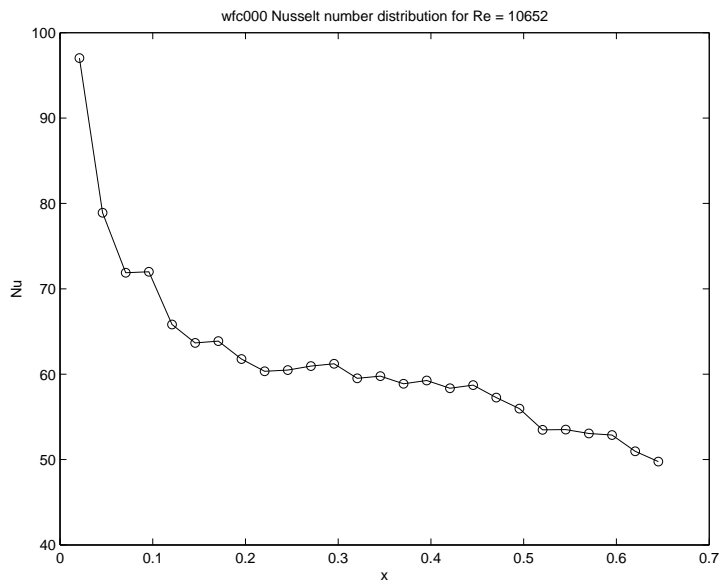


Figure 25: Nusselt number variation for wfc000 at Re = 10652.

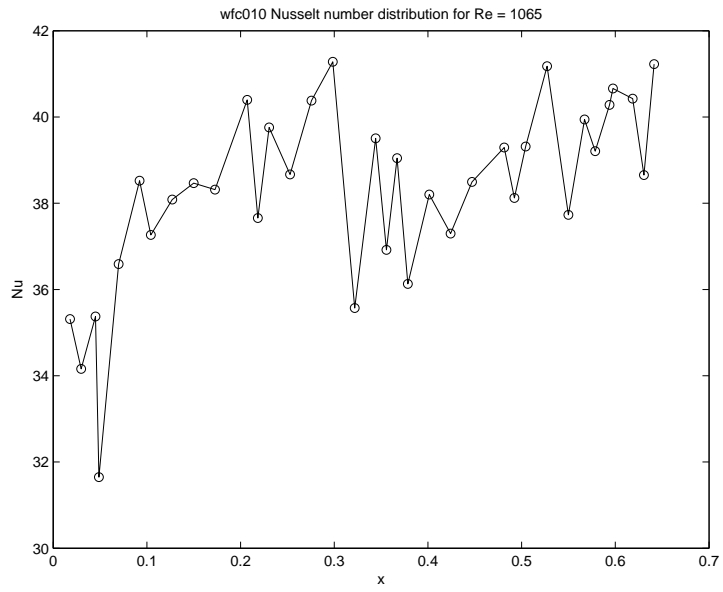


Figure 26: Nusselt number variation for wfc010 at Re = 1065.

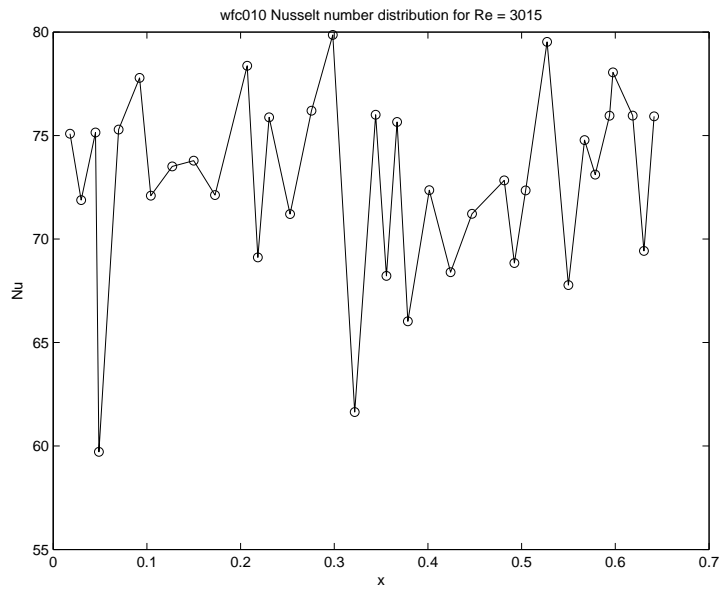


Figure 27: Nusselt number variation for wfc010 at Re = 3015.

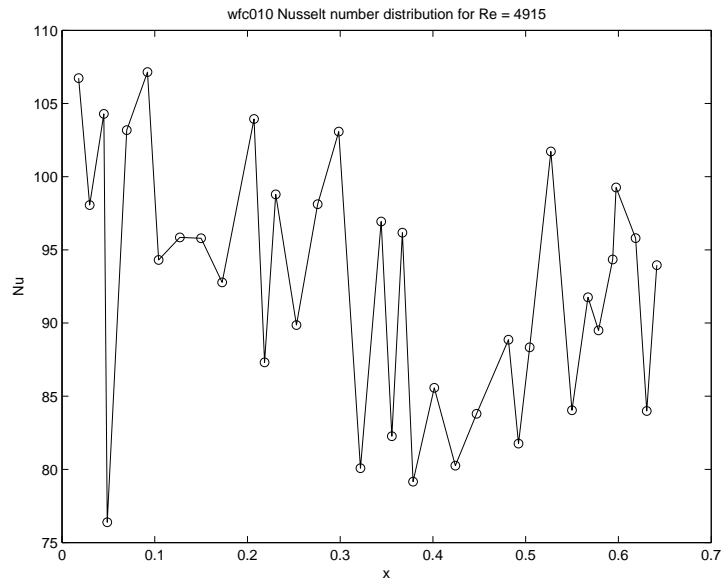


Figure 28: Nusselt number variation for wfc010 at Re = 4915.

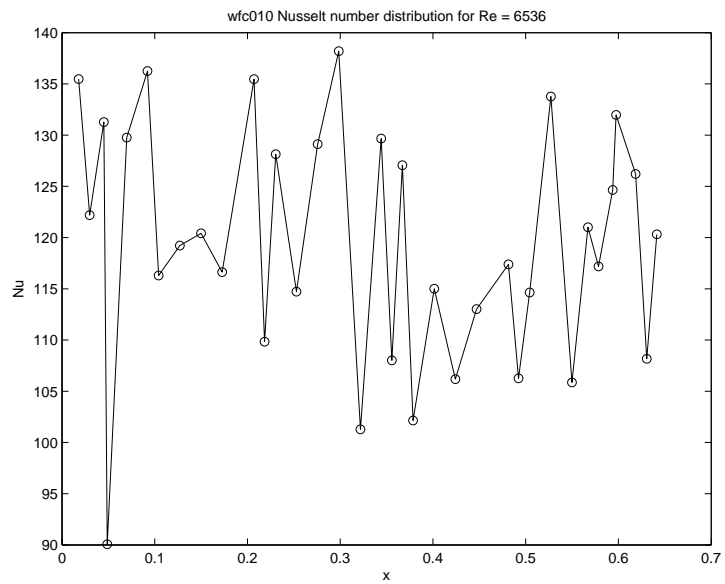


Figure 29: Nusselt number variation for wfc010 at Re = 6536.

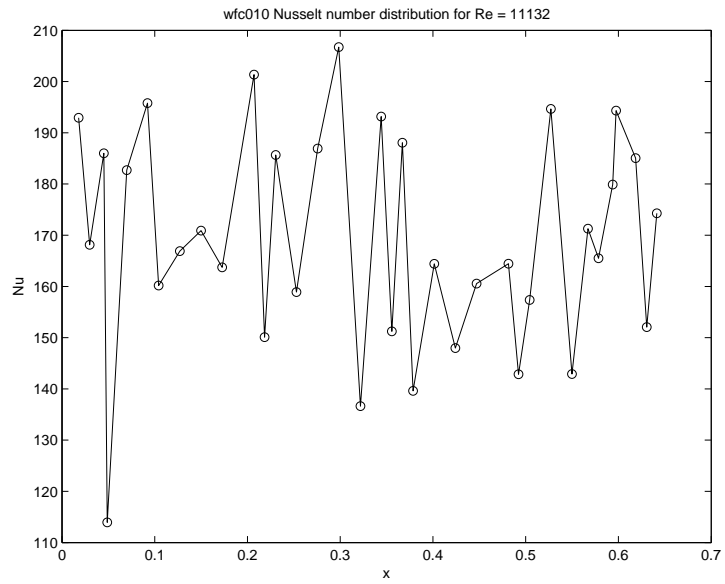


Figure 30: Nusselt number variation for wfc010 at Re = 11132.

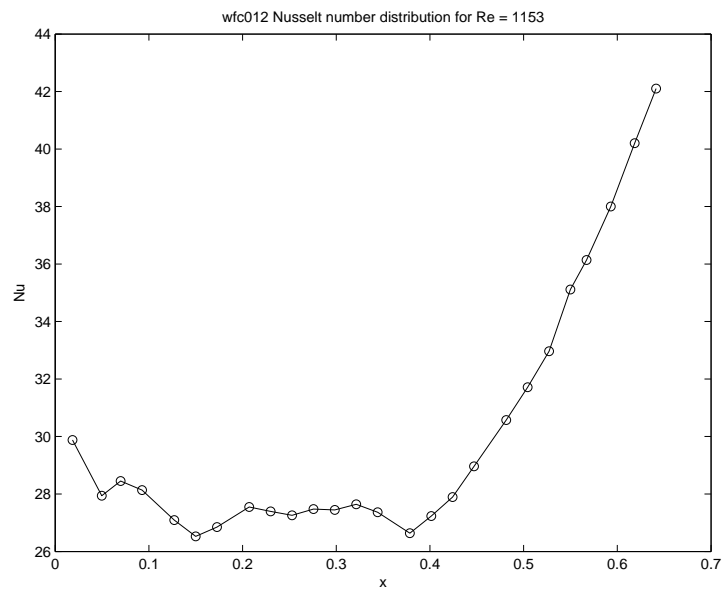


Figure 31: Nusselt number variation for wfc012 at Re = 1153.

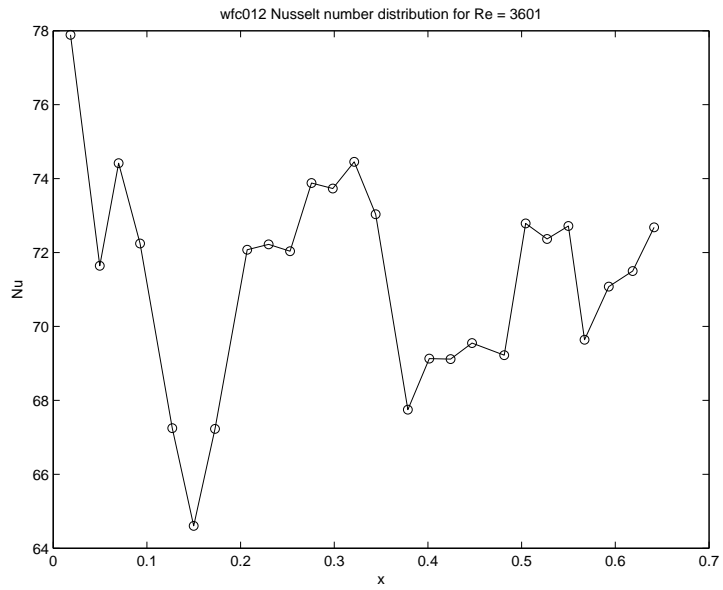


Figure 32: Nusselt number variation for wfc012 at Re = 3601.

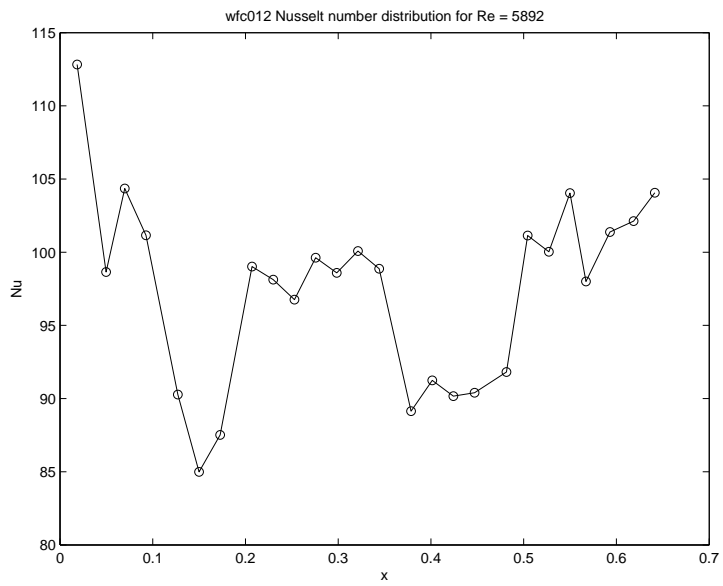


Figure 33: Nusselt number variation for wfc012 at Re = 5892.

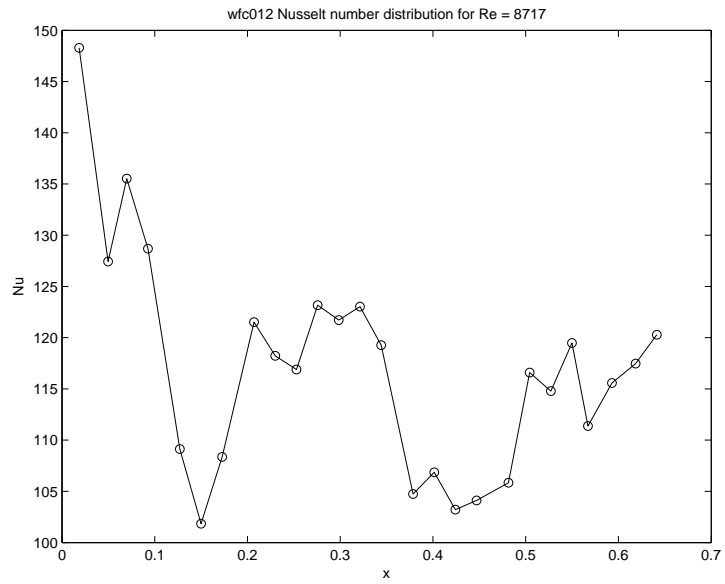


Figure 34: Nusselt number variation for wfc012 at Re = 8717.

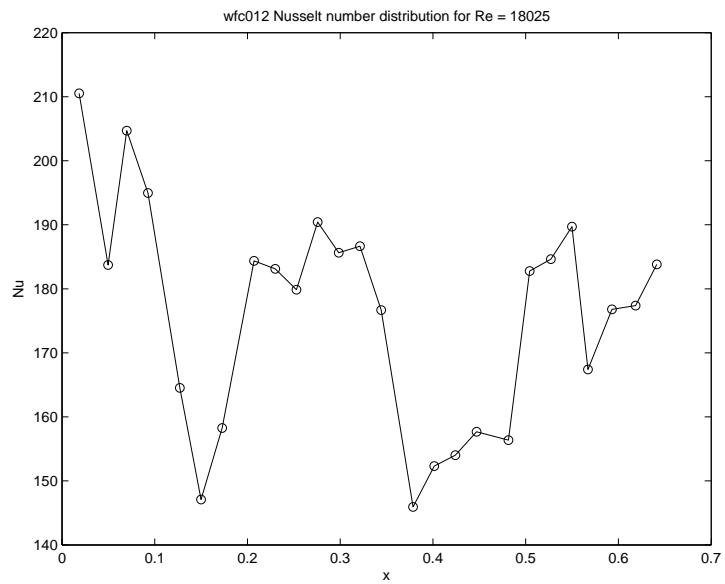


Figure 35: Nusselt number variation for wfc012 at Re = 18025.

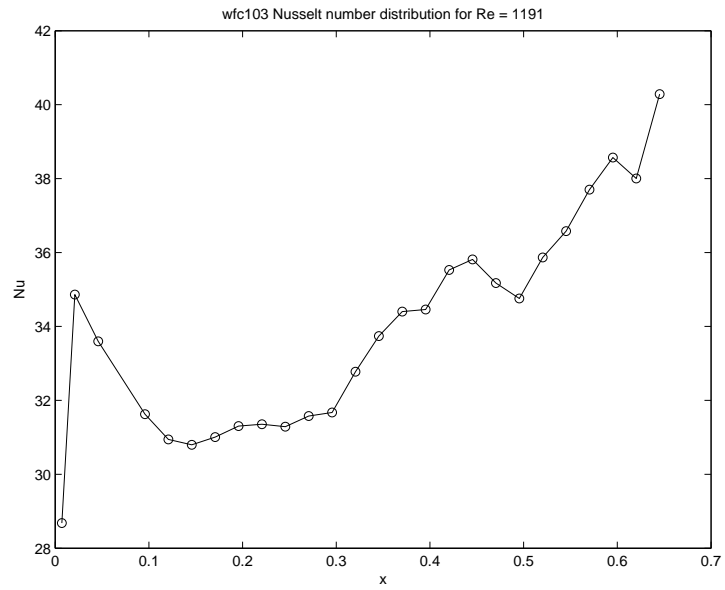


Figure 36: Nusselt number variation for wfc103 at Re = 1191.

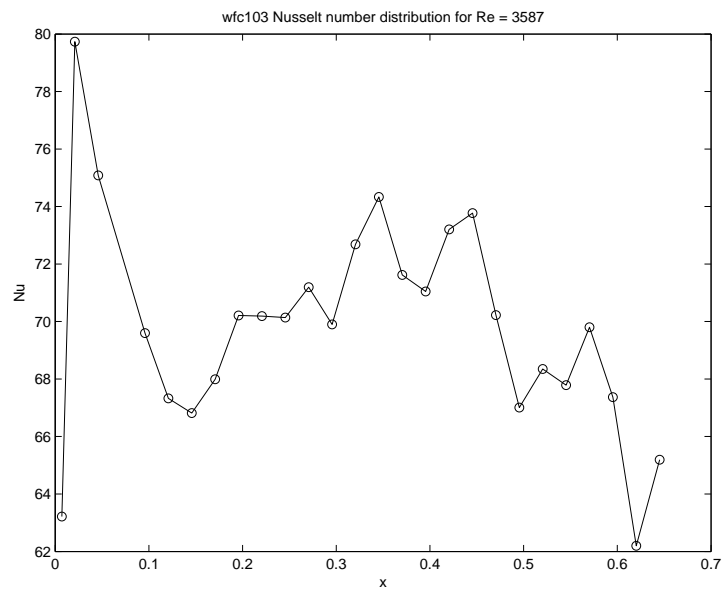


Figure 37: Nusselt number variation for wfc103 at Re = 3587.

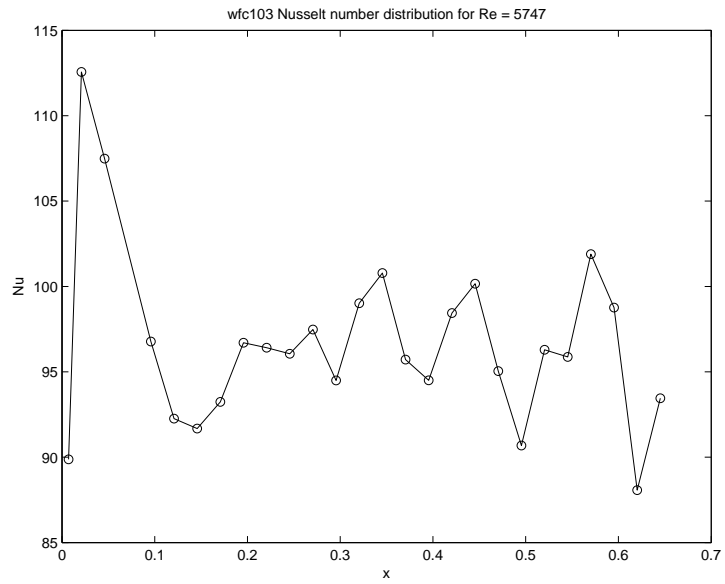


Figure 38: Nusselt number variation for wfc103 at Re = 5747.

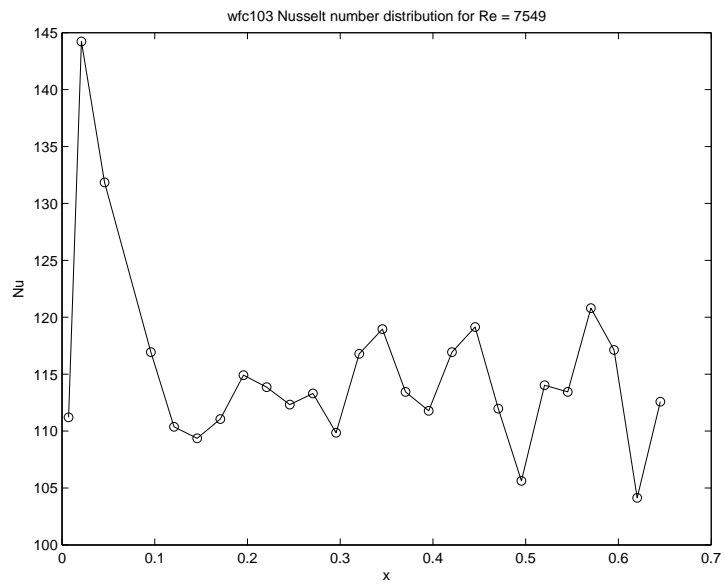


Figure 39: Nusselt number variation for wfc103 at Re = 7549.

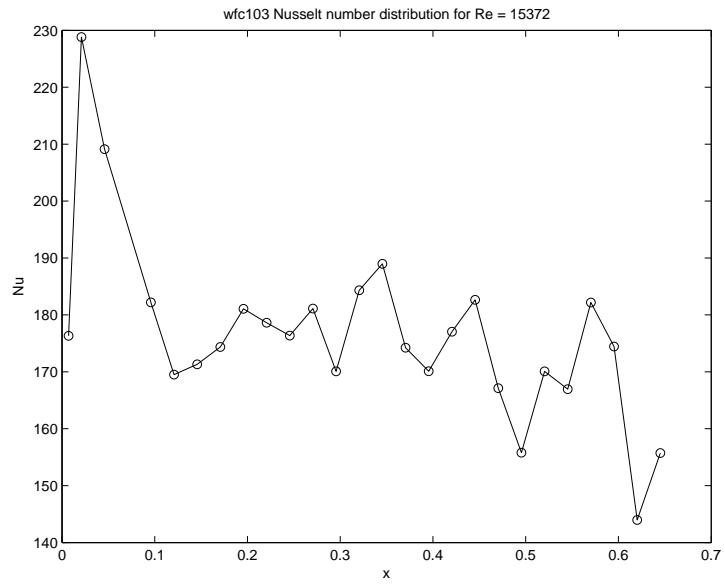


Figure 40: Nusselt number variation for wfc103 at Re = 15372.

REFERENCES

- ASTM, editor. *ASTM Special Technical Publication 470B: Manual on the Use of Thermocouples in Temperature Measurement*. American Society for Testing and Materials, 3 edition, 1981.
- G. Biswas, K. Torii, D. Fujii, and K. Nishino. Numerical and experimental determination of flow structure and heat transfer effects of longitudinal vortices in a channel flow. *International Journal of Heat and Mass Transfer*, 39:3441, 1996.
- Jonathan David Bridges. Experimental investigation of enhanced surfaces in rectangular ducts. Master's thesis, University of Missouri - Rolla, 2007.
- P. Dep, G. Biswas, and N. K. Mitra. Heat transfer and flow structure in laminar and turbulent flows in a rectangular channel with longitudinal vortices. *International Journal of Heat and Mass Transfer*, 38:2427, 1995.
- F. J. Edwards and N. Sheriff. The heat transfer and friction characteristics for forced convection air flow over a particular type of rough surface. In *International Developments in Heat Transfer*, pages 415–425. ASME, 1961.
- W. H. Emmerson. Heat transfer in a duct in regions of separated flow. In *Proc. Third Int. Heat Transfer Conf.*, volume 1, pages 267–275, 1966.
- V. Gnielinski. New equations for heat and mass transfer in turbulent pipe and channel flow. *Int. Chem. Eng.*, 16:359, 1976.
- M. Greiner, R.-F. Chen, and R. A. Wirtz. Heat transfer augmentation through wall-shape-induced flow destabilization. *Journal of Heat Transfer*, 112:336, 1990.
- M. Greiner, R.-F. Chen, and R. A. Wirtz. Augmented heat transfer in a recovery passage downstream from a grooved section: An example of uncoupled heat/momentum transport. *Journal of Heat Transfer*, 117:303, 1995.
- M. Greiner, G. J. Spencer, and P. F. Fischer. Direct numerical simulation of three-dimensional flow and augmented heat transfer in a grooved channel. *Journal of Heat Transfer*, 120:717, 1998.
- J. C. Han. Heat transfer and friction in channels with two opposite rib-roughened walls. *Transactions of the ASME*, 106:774, 1984.
- J. C. Han. Heat transfer and friction characteristics in rectangular channels with rib turbulators. *Journal of Heat Transfer*, 110:321, 1988.

- J. C. Han, L. R. Glicksman, and W. M. Rohsenow. An investigation of heat transfer and friction for rib-roughened surfaces. *International Journal of Heat and Mass Transfer*, 21: 1143–1156, 1978.
- M. S. Isaacson and A. A. Sonin. Sherwood number and friction factor correlations for electro dialysis systems, with application to process optimization. *I & EC Process Des. Dev.*, 15:313–321, 1976.
- A. M. Jacobi and R. K. Shah. Heat transfer surface enhancement through the use of longitudinal vortices: A review of recent progress. *Experimental Thermal and Fluid Science*, 11:295, 1995.
- George E. Karniadakis, Bora B. Mikic, and Anthony T. Patera. Minimum-dissipation transport enhancement by flow destabilization: Reynold's analogy revisited. *Journal of Fluid Mechanics*, 192:365, 1988.
- H. Kozlu, B. B. Mikic, and A. T. Patera. Minimum-dissipation heat removal by scale-matched flow destabilization. *International Journal of Heat and Mass Transfer*, 31:2023, 1988.
- B. Metais and E. R. G. Eckert. Forced, mixed, and free convection regimes. *Journal of Heat Transfer*, 86:295–396, 1964.
- R. W. Miller, editor. *Flow Measurement Engineering Handbook*. McGraw Hill, 3 edition, 1996.
- Lewis F. Moody. Friction factors for pipe flow. *Transactions of the A.S.M.E.*, 66:671–684, 1944.
- Nanmac Corp. *Temperature Measurement Handbook*, 12 edition, 2006.
- J. Nikuradse. Laws of flow in rough pipes. Technical report, National Advisory Committee for Aeronautics, 1950.
- W. R. Pauley and J. K. Eaton. Experimental study of the development of longitudinal vortex pairs embedded in a turbulent boundary layer. *AIAA Journal*, 26:816–823, 1988.
- Stephen J. D. Rucker. Emperical investigation of enhanced air fins. Master's thesis, University of Missouri - Rolla, 2007.
- R. L. Webb, E. R. G. Eckert, and R. J. Goldstein. Heat transfer and friction in tubes with repeated-rib roughness. *International Journal of Heat and Mass Transfer*, 14:601–617, 1971.
- R. H. S. Winterton. Where did the Dittus and Boelter equation come from? *International Journal of Heat and Mass Transfer*, 41:809, 1998.

R. A. Wirtz, F. Huang, and M. Greiner. Correlation of fully developed heat transfer and pressure drop in a symmetrically grooved channel. *Journal of Heat Transfer*, 121:236, 1999.

J. M. Wu and W. Q. Tao. Numerical study on laminar convection heat transfer in a rectangular channel with longitudinal vortex generator. part a: Verification of field synergy principle. *International Journal of Heat and Mass Transfer*, 51:1179, 2008.

L. Xiao-wei, Y. Huan, M. Ji-an, and L. Zhi-xin. Visualization of longitudinal vortex flow in an enhanced heat transfer tube. *Experimental Thermal and Fluid Science*, 31:601, 2007.

J. X. Zhu, N. K. Mitra, and M. Fiebig. Effects of longitudinal vortex generators on heat transfer and flow loss in turbulent channel flows. *International Journal of Heat Transfer*, 36:2339, 1993.

VITA

James Jackson Tinsley II was born at Clark Air Force Base in March of 1982. In May of 2007 he received his B.S. in Aerospace Engineering from Missouri University of Science & Technology. He went on to receive his M.S. degree in Aerospace Engineering in December of 2011.

James was married to Melisia Tinsley in August of 2006, and together they have three wonderful daughters.